AN EXPERIMENTAL STUDY OF A PULSED DC PLASMA FLOW CONTROL ACTUATOR

THESIS

Jennifer D. Wall
Ensign, USN

AFIT/GAE/ENY/06-J16

DEPARTMENT OF THE AIR FORCE
AIR UNIVERSITY

AIR FORCE INSTITUTE OF TECHNOLOGY

Wright-Patterson Air Force Base, Ohio

AFIT/GAE/ENY/06-J16

AN EXPERIMENTAL STUDY OF A PULSED DC DISCHARGE PLASMA FLOW CONTROL ACTUATOR

THESIS

Presented to the Faculty

Department of Aeronautics and Astronautics

Graduate School of Engineering and Management

Air Force Institute of Technology

Air University

Air Education and Training Command

In Partial Fulfillment of the Requirements for the

Degree of Master of Science in Aeronautical Engineering

Jennifer D. Wall, B.S.

Ensign, USN

June 2006

AFIT/GAE/ENY/06-J16

AN EXPERIMENTAL STUDY OF A PULSED DC DISCHARGE PLASMA FLOW CONTROL ACTUATOR

Jennifer D. Wall, B.S.
Ensign, USN

Approved:

_____	_____
Dr. Milton Franke Committee Chairman	Date
_____	_____
Dr. Mark F. Reeder Committee Member	Date
_____	_____
Lt Col Eric J. Stephen Committee Member	Date

AFIT/GAE/ENY/06-J16

Abstract

An experiment on the effects of a pulsed DC plasma actuator on a separated flow in a low speed wind tunnel was conducted. The actuator consisted of two asymmetric copper electrodes oriented normal to the flow separated by a dielectric barrier and mounted on a flat plate in the center of the tunnel. A contoured insert was constructed and used to create an adverse pressure gradient in the test section comparable to a Pak-B low pressure turbine blade distribution. Suction was applied from the upper wall to induce separation along the flat plate over the electrodes. The DC power supply was kept constant at 8.5 kV and power was regulated through a high voltage fast transistor switch. The pulse width of the switch remained at 250 ns with the frequency ranging from 25 to 100 Hz. All studies were conducted at a Reynolds number of 30,000 to simulate takeoff and other low speed conditions. It was found that the DC pulsed plasma actuator could reattach the flow but not consistently at these conditions. Furthermore no evidence was found to indicate that coherent vortical structures are responsible for reenergizing the boundary layer and controlling separation.

Acknowledgements

I would like to acknowledge several people for their help and guidance throughout my research. First, everyone at AFRL for letting me use their facilities and offering advice or a free hand whenever needed, especially Dr. Andrew Lethander and Mr. Robert Wirrig. My sponsor, Dr. Richard Rivir, was always a source of valuable information and support. Dr. Isaac Boxx worked along side me every day and his knowledge and experience were instrumental in the success of this experiment. Lastly, my thesis advisor, Dr. Milton Franke, thank you for your positive encouragement and constant support.

Jennifer D. Wall

Table of Contents

Page #

Abstract i
Acknowledgements ii
Table of Contents iii
List of Figures v
List of Tables viii
List of Symbols ix
List of Abbreviations x
I. Introduction 1
1.1 Background 1
1.2 Objective 6
1.3 Organization 6
II. Theory 7
2.1 Boundary Layers and Turbine Blades 7
2.2 Dielectric Barrier Discharge 8
2.3 Particle Image Velocimetry 10
III. Experimental Setup and Procedure 12
3.1 Wind Tunnel 12
3.2 Test Section 12
3.3 Pressure Measurement and Calibration 18
3.4 High Voltage Supply and Switch 20
3.5 Electrode Photofabrication 27
3.6 Particle Image Velocimetry 29
3.7 Experimental Procedure 33
IV. Results and Analysis 35
4.1 Tunnel Validation 35
4.2 Plasma Effect on Separation Location 45
4.3 Velocity Contours 49
V. Conclusions and Recommendations 57
5.1 Research Objectives 57

5.2 Research Improvements 58
Appendix A: Open Valve Vacuum Plots 60
Appendix B: Supplemental Data for Various Frequencies 62
Appendix C: Average Velocity Contours 67
Appendix D: Supplemental Power Spectrum Plots 71
References 79

List of Figures

Page #

Figure 1. LPT blade arrangement 8
Figure 2. DBD actuator layout 9
Figure 3. PIV image pair 11
Figure 4. Pressure taps dimensions at leading edge and throat location 14
Figure 5. Calculated boundary layer and pressure tap locations along flat plate 14
Figure 6. Contour curve and treadline 16
Figure 7. Upper and side view of contour 17
Figure 8. Pressure measurement equipment 20
Figure 9. High voltage switch 21
Figure 10. Circuit diagram 22
Figure 11. Current, voltage, and pulse traces for HTS 151 24
Figure 12. Instantaneous power trace for HTS 151 25
Figure 13. Current, voltage, and pulse trace for HTS 181 26
Figure 14. DC electrode design 29
Figure 15. Camera and laser arm position 30
Figure 16. Overall setup diagram 32
Figure 17. Vacuum condition compared to Pak-B profile 36
Figure 18. Pressure distribution for various vacuum settings 38
Figure 19. Wide field characterization setup 40
Figure 20. Comparison of no vacuum and vacuum streamlines 41
Figure 21. Velocity contour for no vacuum condition 42
Figure 22. Contour plot for closed valve vacuum condition 43
Figure 23. Boundary layer plot for closed valve vacuum condition 44
Figure 24. Comparison of boundary layer plots for vacuum settings 45
Figure 25. Comparison of flow visualization images 46
Figure 26. Comparison of streamline analysis 47
Figure 27. Comparison of profiles for baseline and with plasma 48
Figure 28. Comparison of velocity field for baseline and with plasma 49
Figure 29. 70% velocity contour 50

Figure 30. Comparison of average 70% contour 51
Figure 31. Baseline contour analysis 52
Figure 32. Actuator on contour analysis 52
Figure 33. Baseline power spectrum (Column 40) 53
Figure 34. Average baseline power spectrum (Column 40) 54
Figure 35. Comparison of average power spectrums 55
Figure 36. Zoomed comparison of average power spectrums 56
Figure 37. Open valve streamlines 60
Figure 38. Open valve velocity contours 61
Figure 39. Open valve boundary layer profile plot 61
Figure 40. Streamline analysis for 25 Hz 62
Figure 41. Streamline analysis for 75 Hz 63
Figure 42. Streamline analysis for 100 Hz 63
Figure 43. Boundary layer profile plot for 50 Hz 64
Figure 44. Boundary layer profile plot for 75 Hz 64
Figure 45. Boundary layer profile plot for 100 Hz 65
Figure 46. Velocity vector contours for 25 Hz 65
Figure 47. Velocity vector contours for 50 Hz 66
Figure 48. Velocity vector contours for 75 Hz 66
Figure 49. 70% velocity contour at 25 Hz 67
Figure 50. 70% velocity contour at 50 Hz 68
Figure 51. 70% velocity contour at 75 Hz 68
Figure 52. 50% velocity contour 69
Figure 53. 60% velocity contour 69
Figure 54. 80% velocity contour 70
Figure 55. 90% velocity contour 70
Figure 56. Average baseline power spectrum (Column 35) 71
Figure 57. Average power spectrum at 25 Hz (Column 35) 72
Figure 58. Average power spectrum at 50 Hz (Column 35) 72
Figure 59. Average power spectrum at 75 Hz (Column 35) 73
Figure 60. Average power spectrum at 100 Hz (Column 35) 73

Figure 61. Average baseline power spectrum (Column 40) 74
Figure 62. Average power spectrum at 25 Hz (Column 40)..... 74
Figure 63. Average power spectrum at 50 Hz (Column 40)..... 75
Figure 64. Average power spectrum at 75 Hz (Column 40)..... 75
Figure 65. Average power spectrum at 100 Hz (Column 40)..... 76
Figure 66. Average baseline power spectrum (Column 45) 76
Figure 67. Average power spectrum at 25 Hz (Column 45)..... 77
Figure 68. Average power spectrum at 50 Hz (Column 45)..... 77
Figure 69. Average power spectrum at 75 Hz (Column 45)..... 78
Figure 70. Average power spectrum at 100 Hz (Column 45)..... 78

List of Tables

Page #

Table 1. Scanivalve channel connections 19
Table 2. Test Matrix..... 34

List of Symbols

Page #

A	Amps	21
C	Capacitance	23
C_p	Plasma capacitance	22
H_1	Height of the flat plate	15
H_2	Height of the contour	15
n	Constant used for repetition rate division	31
P	Power	23
R	Resistance	23
R_p	Plasma resistance	22
V	Volts	21
W	Watt	5
δ	Boundary layer thickness	43
τ	Time constant	23

List of Abbreviations

Page #

AC	Alternating Current	4
AFRL	Air Force Research Laboratory	ii
CAD	Computer Aided Design	16
Cp	Pressure coefficient	4
DBD	Dielectric Barrier Discharge	8
DC	Direct Current	1
EHD	Electro-Hydrodynamic	3
FFT	Fast Fourier Transform	53
FS	Full Scale	18
GE	General Electric	18
HP	Horse Power	16
HTS	High voltage Transistor Switch	21
HV	High Voltage	21
LPM	Low differential Pressure Monitor	18
LPT	Low Pressure Turbine	4
MOSFET	Metal Oxide Semiconductor Field-Effect Transistor	21
Nd: YLF	Neodymium: Yttrium Lithium Fluoride	29
OAUGDP	One Atmosphere Uniform Glow Discharge Plasma	3
PIV	Particle Image Velocimetry	6
Re	Reynolds number	3
STL	Stereolithography	16
UV	Ultraviolet	27
VBI	Vane Blade Interaction	35

AN EXPERIMENTAL STUDY OF PULSED DC DISCHARGE PLASMA FLOW CONTROL ACTUATORS

I. Introduction

In recent years, the increasing demands on the performance and efficiency of low pressure turbines have led to higher blade loading. This increase generates larger adverse pressure gradients which can lead to a faster aerodynamic stall over the blade [1]. Several techniques, such as dimples, ribs and vortex generator jets, have already been examined to determine the ability to control separation losses. However, the key advantage of utilizing plasma actuators to prevent blade stall over these other methods is that the actuators can be operated only when needed and produce no additional parasitic effects. This research effort is an attempt to characterize the effects of a DC discharge plasma flow control actuator on a separated boundary layer.

1.1 Background

The prediction of boundary layer separation has been studied in great detail for a number of years. These studies however are complicated in the low pressure turbine due to the numerous conditions of flight that can exist. At takeoff, the boundary layer is in general more turbulent, but at cruise conditions it may be transitional due to the change in density with altitude. Further complicating the problem is that transition may be occurring before or after separation and the high free-stream turbulence levels that exist in a real engine environment. Hultgren and Ashpis [1] found that the turbulence level and other free-stream unsteadiness greatly affect the size of the separation bubble and transition at low Reynolds numbers and if transition occurs earlier in the boundary layer,

separation can be completely eliminated. A control mechanism to trigger early transition at cruise conditions is therefore desired that has minimum penalty at takeoff.

One of the first to demonstrate control of separated flows was Viets et al. [2], who introduced spanwise vortices near the wall of a stalled diffuser to cause boundary flow to re-attach. Rivir et al. [3] compiled the results of the different methods of passive and active separation control for turbine blades. These methods all introduce streamwise vortices that reenergize the boundary layer flow by adding momentum to the wall layer. The result is early transition and increased circulation. One of the methods described is properly spacing dimples which in effect adds turbulence to baseline blading. This moves the separation and transition rearward and therefore decreases the size and length of the separation bubble [3]. Dimples have been found to reattach separated flows at all Reynolds numbers investigated and are even effective if placed beyond the natural separation region. The major disadvantage to dimples is that they are a permanent structural change. In general, passive techniques, like dimples, are effective in separation control at low Reynolds numbers but induce greater losses at higher values due to increased drag.

Steady and pulsed vortex generator jets have also proven to be effective at low Reynolds number by promoting rapid mixing and early transition. These are identical to the vortex generator “tabs” found on aircraft wings to prevent flow separation. The jets also create vortical structures that pull down energy from the higher velocity free stream to reenergize the boundary layer. The advantage of the jets is that they can be used only when needed and will not create more losses at higher Reynolds numbers. However, the

jets require internal plumbing and a net mass flow. It is also possible that the jets could be destroyed in a hostile operating environment [4].

The deficiencies mentioned in the other techniques however do not exist in the application of plasma actuators. In 1998, Roth, et al. [5] patented the One Atmosphere Uniform Glow Discharge Plasma (OAUGDP). They showed that the spanwise electrode configurations produced a significant thrust due to mass transport and vortical structures induced by strong paraelectric electrohydrodynamic (EHD) body forces on the flow. Huang et al. [4] explains that the high voltage AC supplied to the electrodes caused the air above to weakly ionize. The ionized air is electrically neutral on a global scale, but microscopically it is composed of positively charged ions and negatively charged electrons that were stripped from the atoms to form ions. This state of matter is called plasma. The plasma produces this body force vector, which can induce steady or unsteady velocity components. Electrode configurations are designed to maximize the body force on the charged particles. Van Dyken et al. [6] studied the effects of dielectric thickness, electrode type, input voltage and frequency, and the input waveform on the strength of the body force. They found that a thicker dielectric was best due to its ability to sustain higher voltages prior to failure and a peak operating frequency existed that gave a maximum net force. They also concluded that well-placed actuators could create a body force to decrease drag and increase the stall angle of an airfoil.

Volino and Hultgren [7] demonstrated that plasma actuators would counter the effects of separation and keep the flow attached at Reynolds numbers (Re) from 50,000 to 300,000 to simulate the range from cruise to takeoff conditions. In this study, the flat plate was subjected to a pressure gradient corresponding to that on the suction side of the

Pak-B airfoil. They found that at Re = 50k, the pressure coefficient profile (C_p) would indicate separation on the adverse pressure gradient portion of the test section. When the actuator was turned on, the flow would remain attached and the measured C_p distribution would match that of theoretical profiles at higher Reynolds numbers. In addition, Corke and Post [8] showed that the separation location was relatively insensitive to the different conditions at various Reynolds numbers. For a cascade of Pak-B blades, this location was found to be at x/c = 0.72. Huang et al. [4] further concluded and proved that since the separation location is relatively stable for all conditions, only one actuator placed slightly upstream of this location is needed. An increased number of actuators would not create a significant change.

The majority of studies conducted in the past consist of the effects of alternating current (AC) on an array of electrodes oriented perpendicular to the free stream. High frequency AC glow discharges were first used to provide transition control on axisymmetric bodies in supersonic flows by Corke et al. [9]. They also extended this method to a single unbounded airfoil and showed a significant increase in the maximum angle of attack. Hung et al. [4] applied the technique to a Pak B LPT cascade and demonstrated reattachment of separated flow over a range of turbulence levels and low Reynolds numbers of 10,000 to 100,000.

Enloe et al. [10] attempted to define the discharge cycle of AC applied actuators. The discharge follows a series of phases during each cycle of the AC applied voltage waveform: ignition, expansion, and quenching. Ignition consists of a sudden series of microdischarge events forming dense plasma within a few millimeters of the edge of the exposed electrode. The plasma consists of negative ions that are only maintained if the

magnitude of the applied voltage is continually increased. It is not a uniform volume on top on the dielectric, but the microdischarges are occurring in rapid succession. A potential difference must be kept between the exposed electrode and the dielectric material for the electrode to continue to emit electrons. When the voltage supply is no longer increased or turned off, the plasma does not disappear immediately but slowly loses its energy through collisions with atmospheric particles. This process is called quenching, which occurs when the voltage reaches an extremum. Expansion is the sweep of the microdischarge, as the volume of plasma appears to expand above the actuator over time when voltage is first applied.

Rivir et al. [11] investigated the effects of short pulsed DC excitation on separation control. This method allows a higher electric field strength to be obtained than from high frequency AC sources. Whereas discharge impedance matching is accomplished through inductive and frequency matching for AC sources, it is resistively matched for the pulsed DC case. For this experiment, this was accomplished using various parallel and series combinations of resistors, which produced voltages from 2 to 11 kV with total circuit current up to 25 amps. The DC source and the high speed switch used in this experiment produced a 22 nanosecond to 2 microsecond pulse width atmospheric discharge. The results of this study claimed electrode peak power levels of 2 – 40 kW and an increase of up to 250% in the local velocity for the near wall boundary layer at low free stream velocities [11]. Although the peak power used in DC pulsed actuators is much higher than AC, the time average power is lower due to the shorter on time of the switch required. Over time, the DC pulsed plasma actuators are maintaining flow attachment at a fraction of the power required for AC control.

1.2 Objective

This research project involved multiple objectives and goals. First, some of the existing facilities and experimental setup at the AFRL laboratory needed to be redesigned, altered or newly manufactured. This was necessary to produce results that were well characterized and repeatable. Another one of the objectives therefore was to validate the new design before starting the testing. This was accomplished mostly through a series of pressure measurements and wide field PIV and analysis. A third objective was to acquire velocity field data for a pulsed DC plasma actuator and determine its effectiveness on flow reattachment. Lastly, it was desired to find evidence to support or contradict the existence of coherent vortical structures as the mechanism in which pulsed DC plasma actuators control separation.

1.3 Organization

This paper will begin by first explaining the theory behind several of the different topics that needed to be understood in order to successfully conduct the experiment. Following this will be a description of the experimental setup and procedures utilized throughout the research. Specialized equipment, such as the laser and camera for the PIV measurements, will be discussed in detail as well as new designs or modifications made to the existing facilities. Validation data and results of the experiment will be examined followed by the conclusions drawn from these results. Recommendations for future research and suggested improvements will also be discussed. Lastly, appendices will be supplied containing supplementary data recorded and any additional information needed for the continuation of this research.

II. Theory

The successful conduction of this experiment was predicated on having a working knowledge of all of the processes that were involved. A brief explanation of all areas pertaining to the research effort is given below. These explanations are by no means inclusive, and the sources referenced should be used to obtain more knowledge on the subject matter.

2.1 Boundary Layers and Turbine Blades

The flow field can be divided into two regions: (1) viscous boundary layer adjacent to the airfoil or flat plate and (2) the essentially inviscid flow outside the boundary layer. The velocity of the fluid increases from a value of zero at the wall to the free stream "frictionless" value outside the boundary layer [12]. For a flat plate, the boundary layer will begin as laminar on the front edge and farther downstream transition into a fully turbulent flow. Viscous forces cause the boundary layer to grow as flow continues down the plate. For airfoils, boundary layer growth is also due to the additional pressure forces at the edge of the boundary layer from the free stream flow [12].

Turbine engines have numerous sets of blades: fan blades, low and high pressure compressor blades, and low and high pressure turbine blades. In the turbine and compressor section, sets of stators exist to direct the flow into the rotor section, which consist of rotating disks of blades that resemble airfoils [13]. The rotors serve to power the compressor and other auxiliary systems. Due to the losses from boundary layer growth, there is not enough energy for the flow to completely stay attached on the upper side of the blades. At some location the velocity approaches zero and may begin to move

back on the airfoil resulting in circulation and a larger separation bubble. The extent of separation is also proportional to the turning angle of the flow directed by the stators. Despite incurring greater losses, an increased angle is desirable in order to maximize the work produced by the rotors [13]. A method to control separation is desired that allows this large angle to be maintained. A typical LPT arrangement is shown in Figure 1.

Figure 1. LPT blade arrangement

2.2 Dielectric Barrier Discharge

The dielectric strength of a material is the maximum electric field that it can withstand without breaking down. At this point its insulating properties begin to fail. In this experiment, dielectric material is used to provide a barrier to prevent arcing but at the same time allow current to flow in order to produce plasma. The electrodes are aligned on either side of the dielectric material as shown in Figure 2. An asymmetric configuration has been shown to work best in previous studies with the trailing edge of the upper electrode in the same plane as the leading edge of the lower one. The plasma, described by Enloe et al. [10] as a surface configuration dielectric barrier discharge (DBD), adds momentum to the boundary layer and accelerates the flow near the wall above the electrodes.

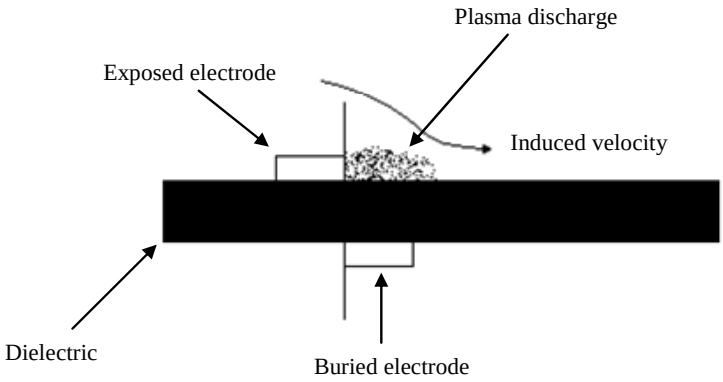

Figure 2. DBD actuator layout

Corke and Post [8] describe how an AC supplied single dielectric barrier discharge is self-limiting and stable at atmospheric pressures. During half of the cycle, electrons move from the exposed electrode to the dielectric and build up until balance with the AC potential is achieved. Plasma generation will then stop. On the second half of the cycle, plasma reforms and the electrons that were deposited on the dielectric travel back to the exposed electrode [8]. This self-limiting characteristic is important as it prevents an excess of electrons that would cause an electric arc. The dielectric constant of air is low and careful attention must be made to ensure an arc will not occur across the electrode leads that are not separation by the dielectric material.

The formation of the plasma from DC pulsed actuators occurs in distinct phases as described earlier for AC applied actuators. The momentum that is added to the boundary layer comes from collisions between the ionized air and the other neutral molecules in the atmosphere. This occurs during the ignition and expansion phases. The difference in the phases for DC and AC is that the time scale is decreased greatly. The applied voltage for DC is only on for the set amount of pulse time, which is usually on the order of nanoseconds. Therefore the evidence of these phases has not been captured on current traces as it has been for AC applied actuators.

2.3 Particle Image Velocimetry

For Particle Image Velocimetry (PIV), two pictures are taken of the test section with a known delay time between the images. The test section is illuminated by two quick pulses of light from a laser. These two pulses are altered from a beam to a thin planar laser sheet using a set of optics focused on the area of interest. The laser sheet actually illuminates the vaporized propylene glycol that is inserted upstream of the test area. Sufficient seeding and laser power are needed to operate a PIV-based experiment effectively. The two pulses of light must also be synchronized with the aperture of the high speed digital camera [14]. The images are then imported to a flow visualization software program. The program maps the velocity vectors accordingly using the image pairs and the known time delay.

The flow visualization software used in conjunction with PIV will determine the distance each particle has traveled using correlation algorithms. The accuracy of these correlations depends heavily on the seed particle density. An ideal of a 10-pixel displacement between seeding particles is suggested for high correlations [14]. The maximum expected velocity of the flow field and the dynamic range must also be known with relative certainty to obtain proper PIV results. The dynamic range is defined as the ratio of pixel resolution to pixel displacement for each time step. If the dynamic range is not great enough, the time delay between laser pulses must be decreased, which results in a decrease in output power. The dynamic range however can be increased through the use of adaptive correlations. Adaptive correlations use an iterative process to determine velocity information resulting in more accurate vector maps as image size and dynamic range increase [14]. This method however is more susceptible to noise. Specific

information on actual equipment and software used in this experiment will be presented in the following section. Figure 3 shows a representative raw PIV image pair that has not undergone processing. These images show how far the flow has propagated downstream by viewing the change in position of the area missing seeding in the center of the images.

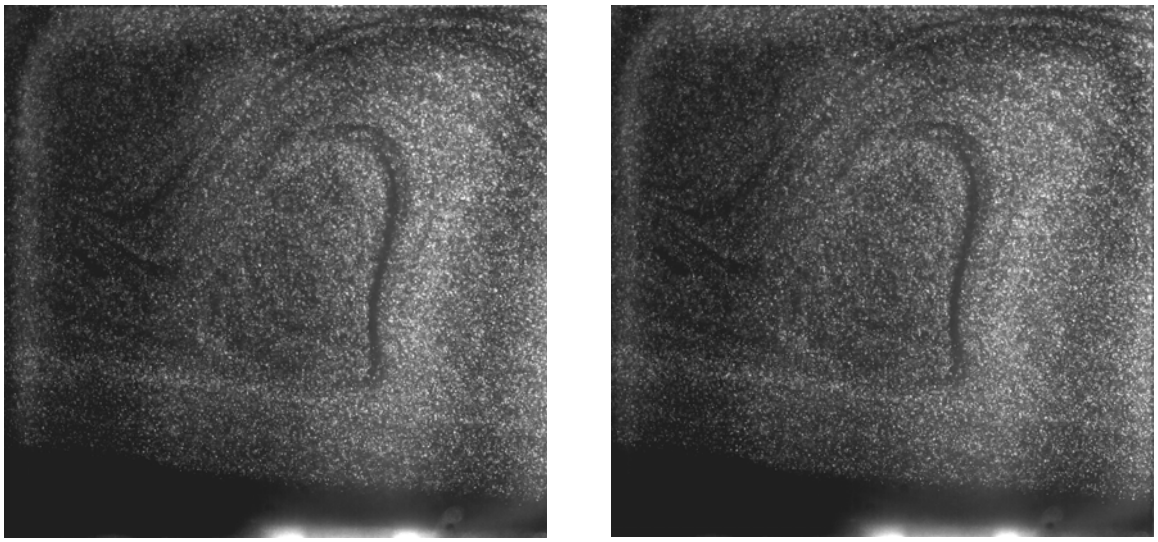

Figure 3. PIV image pair

III. Experimental Setup and Procedure

Multiple pieces of equipment were needed to make this experiment a success. The major components and the procedures used to acquire data are described in detail below.

3.1 Wind Tunnel

The AFRL/PRTT low-speed wind tunnel was used for this research. The wind tunnel operated from one of two compressors and was parallel to two other flow paths. The flow was directed by the position of two air controlled valves. Temperature control was maintained using a heater and chiller capable of a range of 15ºC to 50ºC. The present research was conducted at 80ºF (26.6ºC). Although the cross section of the test section could vary slightly in the vertical direction, for purposes of this research it measured 36 cm wide by 23 cm tall. A rectangular divergent duct is used to direct flow into the test section. To maintain uniform flow, flow straighteners were placed in the cylindrical reservoir at the inlet of the tunnel. Lastly, the inlet contained an opening for the insertion of seeding particles necessary in the use of PIV.

3.2 Test Section

3.2.1 Center Plate. The mid tunnel test section was a modified version of that used by Balcer et al. [13]. A 1.27 cm thick by 69.85 cm long Plexiglas flat plate was mounted across the span of the tunnel. The flat plate has an elliptical leading edge with an aspect ratio of 4:1. In addition, the plate contained a movable flap on the trailing edge that could be set to various angles of deflection. A two-foot-long sheet metal extension was placed on the trailing edge. This increased length allowed for smaller angles of deflection to be utilized with the same amount of blockage produced. This would alter

the velocity over the top of the flat plate without moving the inlet control valve and adding little turbulence. A 1.8 mm cavity was cut into the Plexiglas flat plate in order to hold the plasma actuator. The recessed portion was 45 cm long and 15 cm wide and began 12 cm from the leading edge of the flat plate.

The flat plate was altered for this experiment to include 31 pressure taps in the streamwise direction. The first pressure tap was located 3.81 cm downstream such that the elliptical edge of the flat plate was cleared. A larger number of pressure taps were clustered at 61-85% of the chord where the throat and recess for the electrode is located. This also overlaps the expected position of separation. The pressure taps clustered in the throat were separated in the streamwise direction by 0.64 cm and staggered diagonally to avoid a six degree wake from the proceeding pressure tap. The same method was used for the other pressure taps but with a streamwise separation distance equal to one inch. The location of the pressure taps with respect to the left wall of the tunnel was determined to avoid the boundary layer. The flat plate begins at approximately 1.32 m downstream from the inlet of the tunnel. Turbulent boundary layer thickness was calculated at Re=30k and plotted to ensure all of the taps remained outside. The second and third rows of the pressure taps are further away from the sidewall to remain outside the increasing boundary layer and therefore do not align with the first row. Figure 4 and Figure 5 show the locations of the pressure taps with given dimensions and the calculated boundary layer thickness along the flat plate.

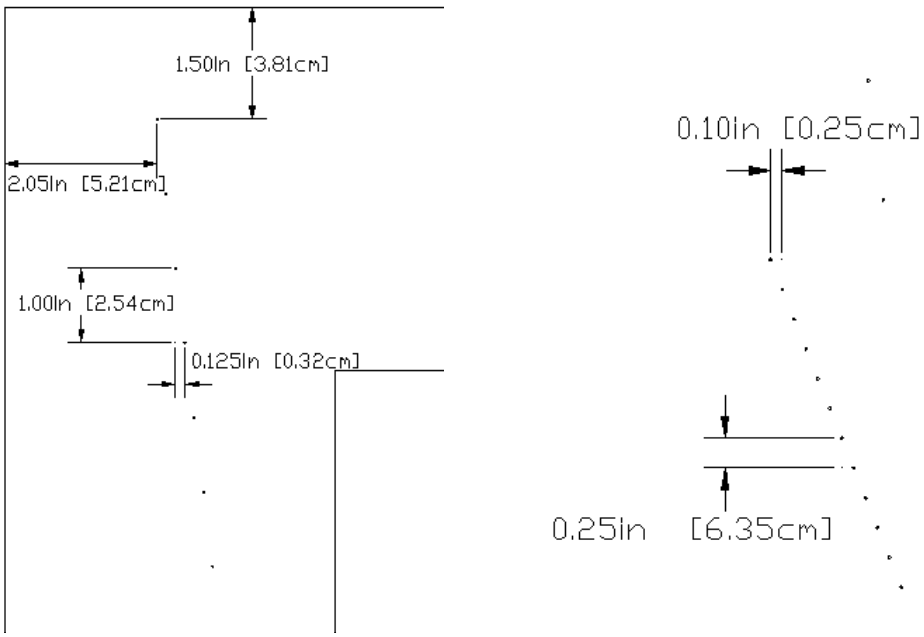

Figure 4. Pressure taps dimensions at leading edge and throat location

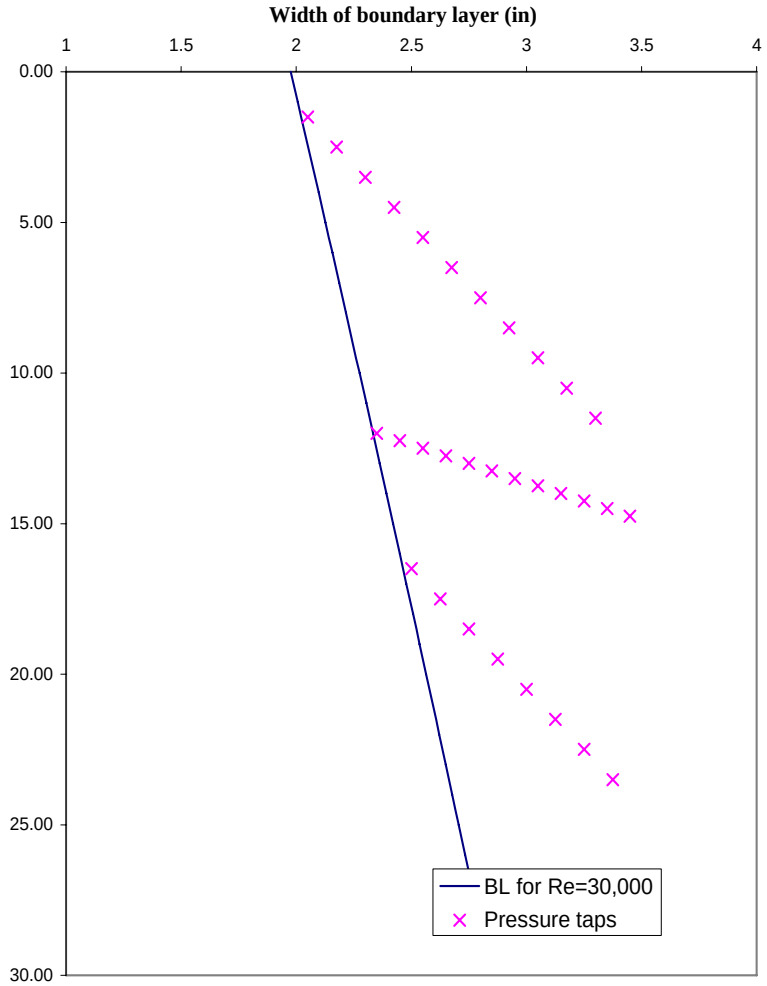

Figure 5. Calculated boundary layer and pressure tap locations along flat plate

3.2.2 Upper Wall Contour. A new method for modeling the C_p distribution of a Pak-B LPT blade over the flat plate was needed for this experiment. Similar to setups used by Hultgren and Ashpis [1] and Volino and Hultgren [7], an insert was necessary that would constrict the flow above the flat plate. This method was chosen as an alternative to studying an actual Pak-B cascade as characterizing boundary layer conditions and PIV along a flat plate can be accomplished with greater ease. An equation was derived to determine the necessary height of the contour as a function of x/c given the known C_p distribution of a Pak-B LPT blade at a high Reynolds number. Using the definition of the pressure coefficient and assuming incompressible isentropic flow in the test section, the height of the contour was found to be proportional to the height above the flat plate and inversely proportional to the square root of the given C_p distribution as shown in the following equation:

$$H_2 \cong H_1\left[C_p\left(x/c\right)\right]^{-\frac{1}{2}} \tag{1}$$

Where H_1 is the height of the flat plate and H_2 is the height of the contour above the flat plate. This curve was then smoothed to produce a more gradual front end. Once plotted, a treadline was created to calculate a large number of coordinates easily. Figure 6 shows the final curve and treadline used in producing the new contour.

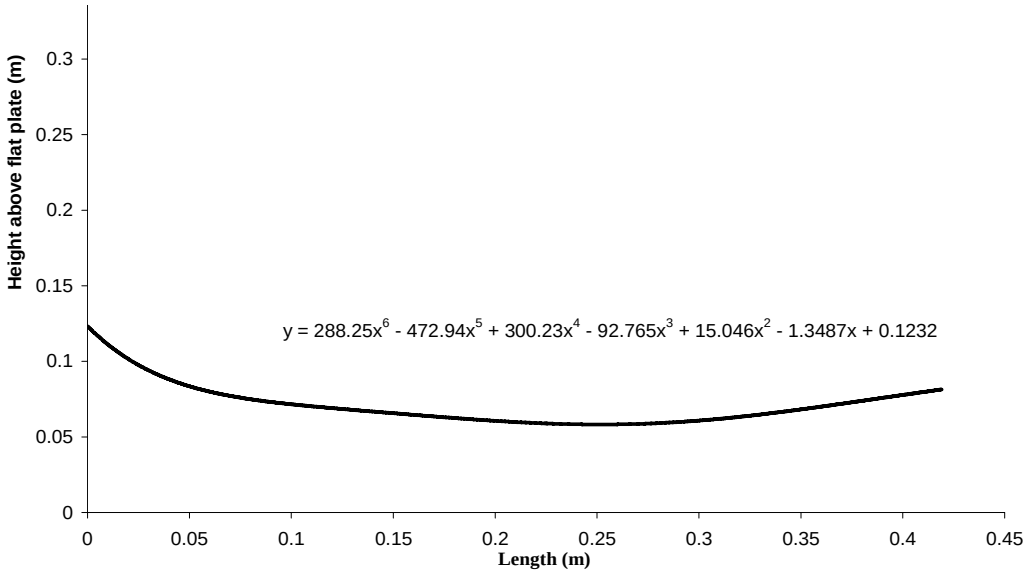

Figure 6. Contour curve and treadline

A large number of coordinates was needed to create a smooth 3-D AutoCAD model of the contour from the above curve. The model included two slots to the contour for the laser sheet and another one that can be used for suction. The vacuum slot meets up with a hole on the top side of the contour, which is connected to a small divergent duct. This divergent duct is attached to a 2 HP shop vac vacuum, which is needed to keep the flow attached along the surface of the contour. Multiple cavities were also designed into the contour to decrease the overall weight and production time. Both the entire contour piece and the divergent duct were created using stereolithography (STL) technology. Stereolithography, also known as 3-D printing, uses an ultraviolet laser to harden the liquid photopolymer layer by layer until the model is complete. The model is then typically washed in a solvent and then baked in an ultraviolet oven to cure the new object. Figure 7 shows two pictures of the top view of the contour with the duct attached and cavities exposed and the other with the slots visible on the underside.

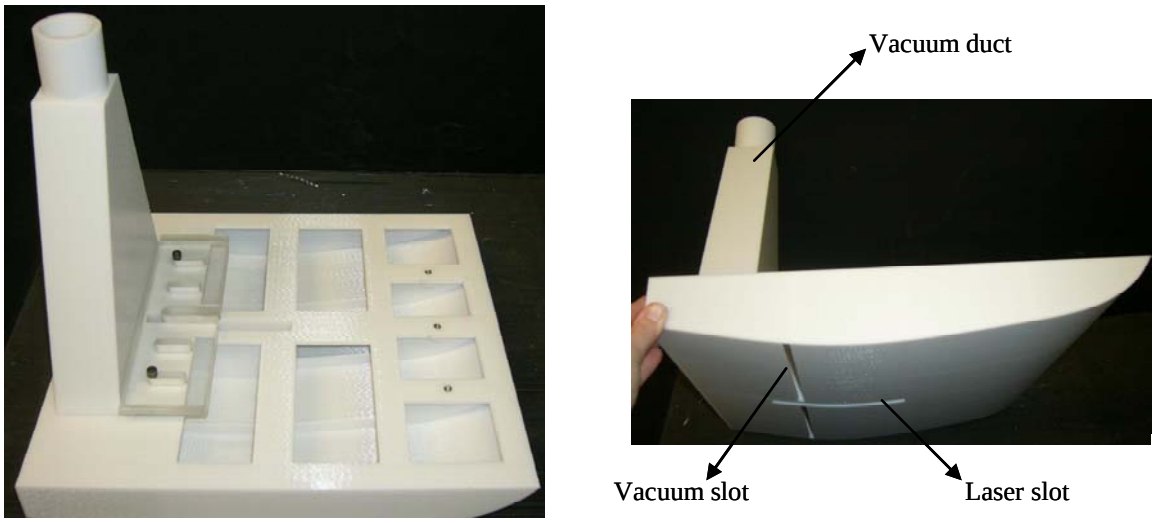

Figure 7. Upper and side view of contour

A simple tail section was added by manufacturing a 34.29 cm long piece of Plexiglas that aligned perfectly with the end of the above contoured section. A smoothed radius was added on the end and a large cavity was also removed from the topside to decrease the weight. This piece was added so that end effects would not alter the flow significantly in the main test area. The contour and tail end were held smooth against the upper wall using small Plexiglas blocks designed with slots to allow access to the threaded inserts designed in the two pieces. One can be seen in Figure 7 that was particularly designed to avoid the laser sheet. These blocks allowed for easy access into the main test section as the contour and tail end could be simply slid further down the tunnel. Lastly an optical quality glass insert was manufactured that fit perfectly into the laser slot on the contoured section. This addition was designed after some preliminary flow visualization revealed that the flow along the contour was being tripped by the leading edge of the laser slot. The insert was designed by using the corresponding points from the treadline in Figure 6 that were omitted from contour to make the laser slot to ensure the surface remained smooth. The insert was also necessary to prevent flow leakage and provide better flow visualization.

3.3 Pressure Measurement and Calibration

The pressure taps were connected to a 48 port J9 scanivalve for quick accurate readings. All 31 pressure taps were connected to determine the pressure distribution along the flat plate. Every other channel in the throat is left open to atmosphere as increased accuracy is desired in this area. This is done to clear out the proceeding pressure input sent to the pressure transducer and to ensure there is enough wait time in between the scanivalve readings. Two Kiel probes are located at the inlet and exit of the tunnel. The inlet probe is used to determine the total pressure of the flow and used in conjunction with the exit probe to find total mass flow in the tunnel. The last scanivalve port is the static reading from a port along the side wall of the tunnel. The numbers in Table 1 represent the pressure port location starting at the leading edge of the flat plate. These pressure locations will become crucial when validating the C_p distribution of a Pak-B turbine blade. The scanivalve is connected to a scan control machine and a position display box that can be controlled automatically through the computer or manually by stepping through port to port.

The pressure transducer used in this experiment is a low differential pressure sensor, GE LPM 5481 with a range of 0 to 0.4 in H_20 and an accuracy of 0.25% FS [15]. This gives an error of less than 1% in the throat for Re=100k. Before and after pressure scans are taken, the transducer and the scanivalve were connected to a deadweight calibration tester. The deadweight tester is a GE Ruska V1600/3D. A deadweight tester works by determining the interaction of airflow with a non-cylindrical piston loaded with a known weight. A pressure is supplied to the deadweight tester and regulated until the known weight begins to float above the piston. The pressure measured is approximately

equal to known weight divided by the area of the cylinder. The deadweight tester can also be used in a differential mode where two pistons can be loaded with weights. The calibration pressure is then the difference between the two. This allows for smaller pressures to be obtained by using weights that are close in magnitude.

Table 1. Scanivalve channel connections

Scanivalve port	Destination / pressure port	Scanivalve port	Destination / pressure port
0	Inlet probe	24	Atmosphere
1	1	25	18
2	2	26	Atmosphere
3	3	27	19
4	4	28	Atmosphere
5	5	29	20
6	6	30	Atmosphere
7	7	31	21
8	8	32	Atmosphere
9	9	33	22
10	10	34	Atmosphere
11	11	35	23
12	Atmosphere	36	Atmosphere
13	12	37	24
14	Atmosphere	38	25
15	13	39	26
16	Atmosphere	40	27
17	14	41	28
18	Atmosphere	42	29
19	15	43	30
20	Atmosphere	44	31
21	16	45	Empty
22	Atmosphere	46	Exit probe
23	17	47	Static Port

The weight on the piston forces air through an outlet aperture, which is then read and assigned a voltage by the pressure transducer. A calibration curve was then plotted from the test weights and corresponding voltages and used to convert the voltage readings for the pressure traces. The pressure transducer was always turned on for a couple of hours to stabilize before taking data as measurements could vary significantly with temperature. Calibrations were taken at the beginning and end of the day with the deadweight tester connected directly to the pressure transducer and also connected indirectly to the pressure transducer through the scanivalve. A pressurized nitrogen gas

bottle was used to supply clean air to the deadweight tester. Figure 8 shows the scanivalve, display control boxes, deadweight tester, and the pressure transducer used for the pressure measurements.

Figure 8. Pressure measurement equipment

All voltages from the calibration tests and pressure traces were recorded using two LabVIEW programs. The programs were set to a sample rate equal to 1000 and a sample time of 20 seconds giving 20,000 values to average for each scan location. An additional 60 second settling time was also incorporated to create a delay in the readings. This time was chosen by determining how long it took for the atmosphere ports to be recorded as approximately equal. The LabVIEW program provided raw data files which were then used in conjunction with Excel and MATLAB to determine the C_p distribution. This data will be presented later in the results section.

3.4 High Voltage Supply and Switch

A Glassman high voltage supply was used to power the switch, which will in turn regulate the voltage and current sent to the electrode. A lot of precaution was used when operating the high voltage supply. Before even attempting to use the supply, a good earth

ground had to be made and before each run several locations were tested to ensure no potential existed. The supply was able to produce an output voltage and current up to 12 kV and 330 mA [16]. The supply had a digital display for the voltage output but a trend indicator also showed the voltage as a percentage of the full rated output in a ten element bar graph. The supply was directly connected to the high voltage switch and both shared a common ground.

The first switch utilized was a Behlke HTS 151 fast high voltage transistor switch. The switch consists of a variety of MOSFETs turned on by a positive going signal of 3 to 10 volts amplitude. The on-time can be set as low as 150 ns with a delayed rise time of 10 ns. The switch can handle up to 10 kV and 30 A DC [17]. The HV switch was contained inside a high power metal case. The metal case also held a 25k pF capacitor and three 100 kΩ resistors placed in parallel. When the switch is not open, the capacitor stores the voltage from the HV supply. Outside the case, a 1 kΩ resistor was placed in parallel to the electrode that serves as a bleed resistor for the current when the switch is open and the plasma is not formed. A set of parallel resistors totaling 560 Ω was placed before the parallel legs in case of failure. These resistors would ensure that the switch did not see a large current spike if the following parts of the circuit shorted. Figure 9 shows the high voltage switch and the other contents of the metal case.

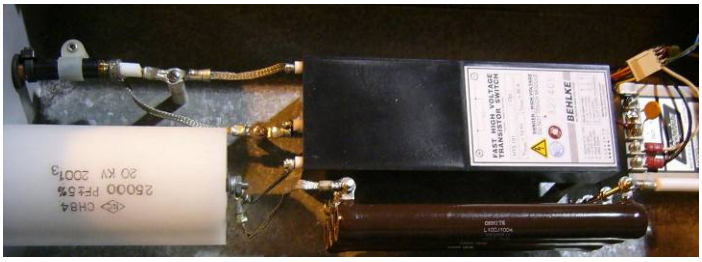

Figure 9. High voltage switch

A voltage probe was also connected across the resistors and electrode. The probe measuring the voltage across the resistors is a North Star high voltage PVM-11. It can sustain a maximum pulsed voltage of 12 kV and has an inherent resistance and capacitance of 50 MΩ and 15 pF [18]. A current coil was placed to measure the total current going to the electrode and 1 kΩ resistor. Therefore the total applied power can be calculated. The plasma produced also has some inherent resistance and capacitance, R_p and C_p. The resistance of the plasma can be approximated if the current coil is moved to right before the electrode and compared to the total current. The coil, Pearson current monitors model 4100, have an internal resistance of 50 Ω and an output of one volt per amp [19]. Figure 10 represents the described circuit diagram with boxes drawn for the voltage probes, current coil, and the electrode.

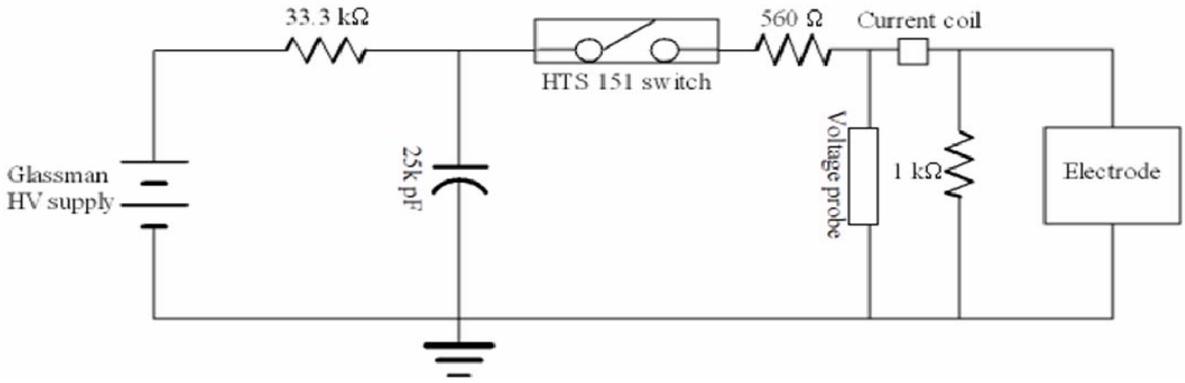

Figure 10. Circuit diagram

The current coil and voltage probe are connected to a LeCroy 600 MHz oscilloscope. The WaveRunner 64Xi series oscilloscopes are capable of up to 10^{10} samples per second and data files are easily saved in Excel or MATLAB format. A pulse generator is also connected to one of the channels of the scope. The pulse generator used was a four channel digital model (DG535) by Standard Research Systems. Both the

frequency and pulse width were set which determined the closed time of the switch and the time average power being sent to the electrode.

The electrode was supplied 8.5 kV as this was found to sustain a discharge consistently. The voltage is not just a square waveform as the switch contains some inherent capacitance and the external resistors create a RC circuit. The voltage waveform instead has a gradual decay with has a time constant, τ, equal to the product of the circuit's resistance and capacitance:

$$\tau = RC. \tag{2}$$

The switch has a minimum rise time of 180 ns. Therefore to set the effective pulse width to 250 ns, the pulse generator would be programmed to 430 ns as the voltage and current trace do not begin to rise until 180 ns later due to the switch delay. Initial current spikes are also characteristic of the switch. These data points occurred on such a small time scale that they did not affect power calculations. Current and voltage traces were taken on a LeCroy oscilloscope, which captured data files whenever triggered. Power was calculated from the following equation:

$$P = IV\,. \tag{3}$$

The current and voltage traces also contain inherent noise from cumulative inductance in different parts of the circuit and the equipment utilized. Figure 11 shows sample images of a 430 ns pulse and the resulting current and voltage traces.

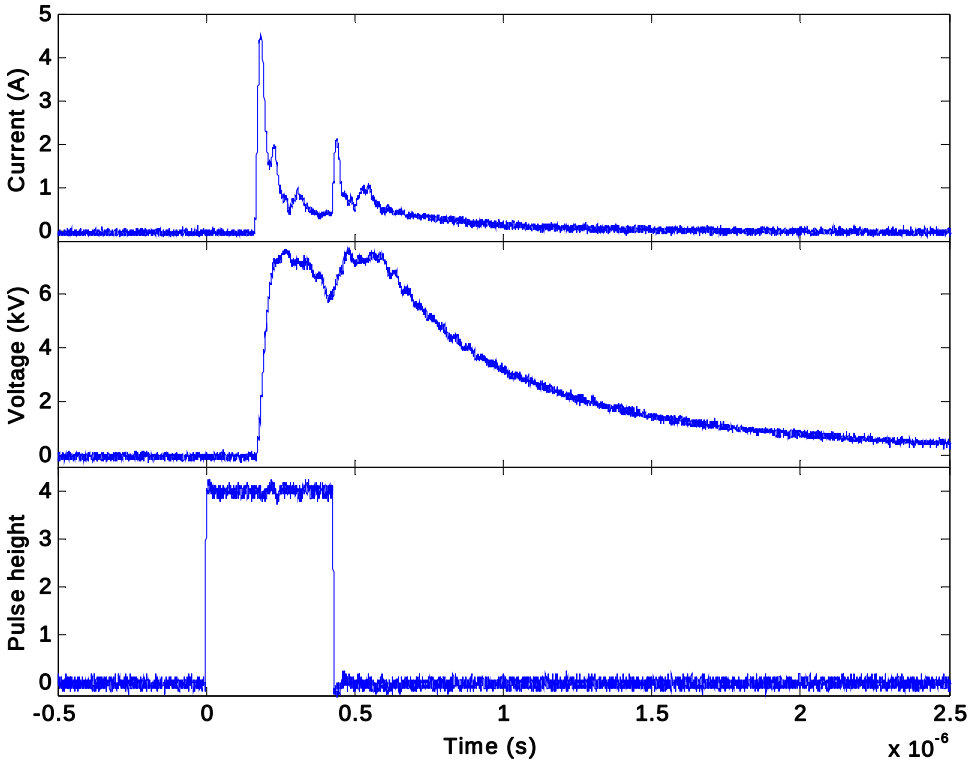

Figure 11. Current, voltage, and pulse traces for HTS 151

The figure also shows the double lobe present in both the voltage and current traces. This is also characteristic of the Behlke 151 switch used. Similar waveforms were found by Rivir et. al, [11] who utilized a similar high voltage transistor switch. A series of voltage and current traces were averaged and used to find the instantaneous power shown in Figure 12. The power trace exhibits the double lobe feature and the gradual decay like that of the voltage and current. As shown in the graph, the power reaches peaks of approximately 15 kW. Taking into account the effective pulse width of 250 ns at a frequency of 100 Hz, the time average power is only about 0.4 W.

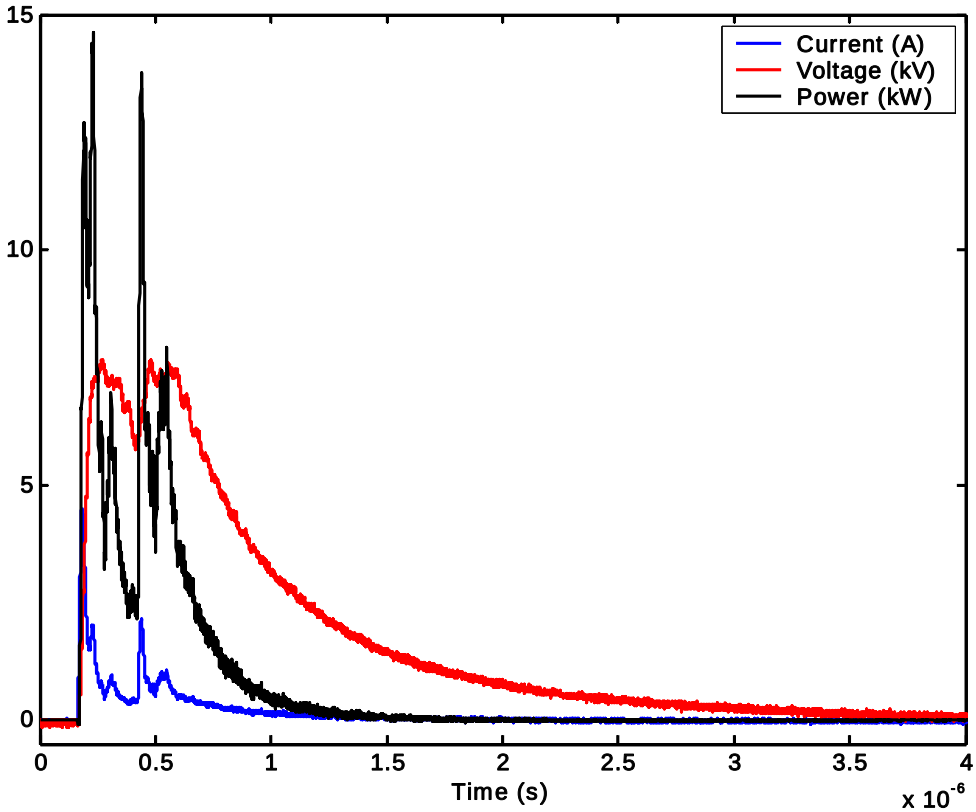

Figure 12. Instantaneous power trace for HTS 151

These high voltage fast transistor switches are relatively easy to use and their behavior is highly reproducible. They however do have a limited unknown lifetime. One by one, the MOSFETS began to fail until the switch's behavior became inconsistent and unsafe. For this reason, the switch was changed after only one run condition was performed at a frequency of a 100 Hz. The replacement, a Behlke 181 switch, has essentially the same characteristics of the 151 model. It however has a higher voltage and current rating of 18 kV and 60 amps. The overall circuit diagram presented in Figure 10 was kept the same except a 1 MΩ resistor was placed in parallel to the electrode instead of the 1 kΩ. This was done in part to extend the life of switch. Compared to the expected resistance of the plasma, the current does not want to travel through the 1 MΩ resistor and therefore it does not appear as a load in the circuit. The 1 MΩ resistor chosen is inductive however. This does ensure the resistor looks less like a load but

unfortunately introduces noise in the current and voltage traces. The current coil and voltage probe were kept in the same position.

The 1 MΩ resistor also increases the time constant significantly and therefore the trail off of the voltage is greater for this setup. The current, voltage and pulse traces for the HTS 181 switch are included in Figure 13.

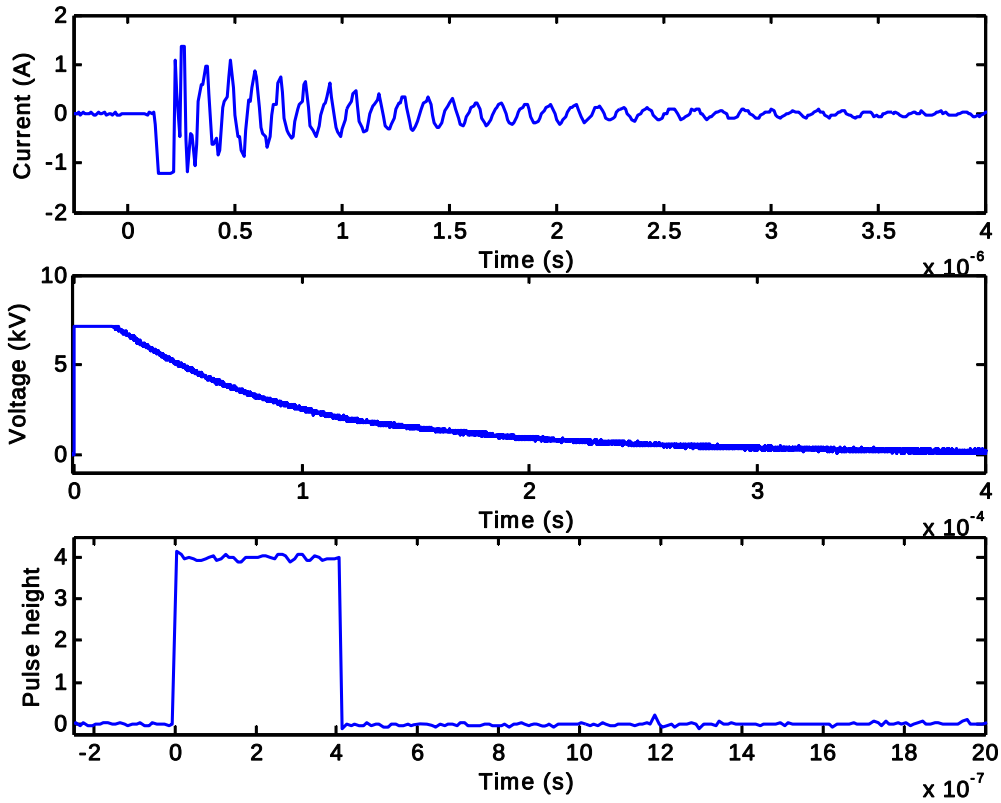

Figure 13. Current, voltage, and pulse trace for HTS 181

Figure 13 is not included with one time axis to show the detail of the trail off on the voltage trace. If the graphs were aligned it would show there is less of a time delay for this switch. The voltage and current become high about 160 ns after the trigger. The pulse width was therefore set to 410 ns to create an effective pulse of 250 ns. Showing the detail of the trail off also causes the peak of the voltage trace to be clipped. The peak of the voltage waveform is similar to the first switch but does not exhibit the double lobe feature. The voltage applied to the electrode for both switches was kept constant at 8.5

kV. The current waveform unfortunately does not provide useful information as it has been affected significantly from the noise due to added inductance of the 1 MΩ resistor.

3.5 Electrode Photofabrication

An FR4 copper clad fiberglass laminate circuit board was cut to fit the cavity on the flat plate. The board is 62 mil thick with a coating thickness of 1 oz/ft^2 and a dielectric strength of 28 V per micrometer. The electrode photofabrication took place in the AFRL/PRTT Heat Flux Instrumentation Laboratory (Class 10,000 clean room). The board was first laminated with a DuPont Riston FX 900 series photoresist 30 micron thick using a dry film laminator. The photoresist was covered with a polyester film that protected the copper from oxidation and contamination.

An electrode pattern was created to optimize conditions for DC pulsed discharge by keeping the ends of the electrode as close as possible to minimize inductance. This pattern was transferred as two negatives (one for both the top and bottom electrode) on acetate paper such that the darkened areas would not be exposed to the UV light. The non darkened areas were the electrode shape and non crucial areas on the board. These areas were included to decrease the amount of time spent on the next step of fabrication. Special attention was taken to ensure that the electrode design was flawless as any anomaly could become a hot spot susceptible to arcing. Crosshairs were included on the negatives to align the circuit board in between the two easier.

The negatives and the circuit board were then placed on the glass of the UV exposure device and vacuum sealed together. The vacuum seal ensured that the negative patterns would have good contact with the board and prevent any shadow effects. The negatives were placed on the circuit board such that when positioned in the tunnel the

electrodes would be approximately at the expected separation region along the flat plate. The top of the device was then rotated 180 degrees to place the board directly over the 3000 W halide bulb. The board was exposed and the process was repeated for the opposite side. The UV light hardened the photoresist in the non darkened areas of the masks which serves as protection for the electrodes against the chemical bath in the next step of fabrication.

The first chemical bath is used to remove the unwanted laminate from the boards. This was done by constantly pouring a warm 1% solution of sodium carbonate on the board leaving the bare copper. An etching solution of 1% sodium persulfate was then used to remove the unprotected copper from the substrate. The board was placed in the solution bath and manually agitated to encourage the etching. After the copper was etched away, the board was rinsed with distilled water and hung up to dry. Black paint and a permanent marker were used to darken the area around the electrodes to decrease the reflection from the laser and the overall noise in the PIV images. At this point the electrodes are still protected with the photoresist. A small portion had to be manually etched off with acetone and Teflon-covered copper tape was soldered onto these spots. The tape was fed through the tunnel's side wall and connected to the external resistors outside the high voltage switch.

The dimensions of the plasma emitting portion of the electrodes were approximately 11.43 cm long and 0.32 cm wide. This results in an area of 362.4 mm^2, which is similar in size to electrode used by Boxx [20]. The top and bottom electrode are separated by the thickness of the circuit board, 1.59 mm. Figure 14 shows the completed electrode used during this experiment.

Figure 14. DC electrode design

3.6 Particle Image Velocimetry

3.6.1 Laser and Light Arm. For this research, the Pegasus-PIV diode-pumped Nd: YLF laser system was used. This laser system is designed for high speed or time resolved PIV analyses. The Pegasus-PIV features a dual-head design, which allows for one laser to be triggered independently of the other. Each laser head can operate from 1 – 100,000 pulses a second allowing camera frame rates up to 20,000 frames per second. The energy for each cavity at 527 nm is 10 mJ at 1 kHz as documented in the manufacturer's performance specifications. This however drops to around 1 mJ at the repetition rate of 10 kHz [21].

The laser light is directed into the test section through a laser arm manufactured by Dantec Dynamics, Inc. After exiting the light arm, the beam is refocused and reshaped into a laser sheet using Dantec Dynamics modular light sheet optics. The laser sheet is then shone through the laser slot built into the upper wall contour. This slot is covered by a piece of optical quality glass that prevents air tunnel leakage but can be removed in case access to the test section is desired. The laser sheet was focused in the middle of the plasma actuator in order for the light intensity to be great enough for the

camera to capture useful images. Proper seeding was accomplished with a Rosco 4500 fog machine using 1:1 mixture of propylene glycol and distilled water.

3.6.2 High Speed Digital Camera and Timing. Imaging was accomplished using a high speed, mega-pixel, light-sensitive Photron APX camera. Its sensitivity to light allows for faster shutter speeds up to 4 μs with decreased blur. The APX camera provides full 1024x1024 pixel resolution at 200,000 frames per second. The camera can store up to 8 Gigabytes of data before downloading [22]. The camera is used in conjunction with two Nikon micro lenses. The 105 m and the 200 mm lens are used for wide field and narrow field PIV respectively. The wide field lens was used to characterize boundary conditions and the separation along the flat plate and upper contour. The narrow field was utilized to capture the plasma discharge and the resulting effects on the flow. The fields of views were determined from ruler images on the flat plate. Figure 15 shows the camera and light arm in their final configuration.

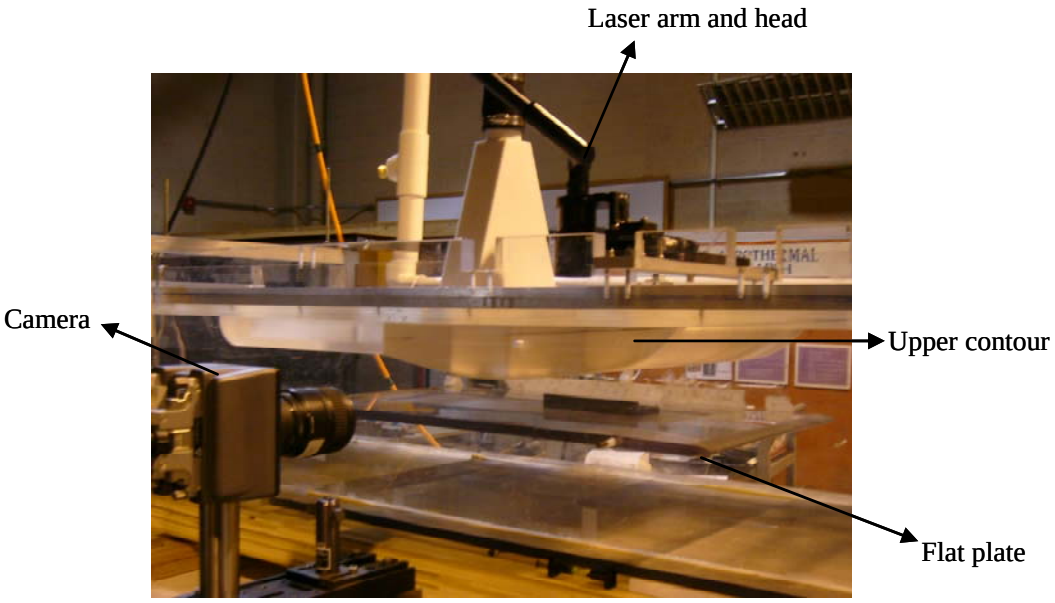

Figure 15. Camera and laser arm position

It was necessary to synchronize the camera shutter and the firing of the laser. The camera with a repetition rate of 600 Hz first received a 50 μs trigger from the Quantum Composer as the camera needs time to respond. The shutter stays open for 500 μs (2000 frames/second) until it needs time to transfer data to its memory and perform certain internal checks. This happens again before another trigger is received from the Quantum Composer. These are the two frames that make up an image pair. The Quantum Composer is then used to trigger the first laser pulse on the end of the first frame and the next pulse on the beginning of the second. The Quantum Composer also triggers the pulse generator that determines the pulse width and frequency sent to the high voltage switch. The pulse generator is used instead of the Quantum Composer directly because it has better time resolution at the small values used to trigger plasma production.

The Quantum Composer however makes it possible to connect the repetition rate of the camera and plasma production together. Using the divide-by-n function on the Quantum Composer enables the user to change the repetition rate to a factor of "n" of another frequency set on a different channel. For example, with the camera's repetition rate set at 600 Hz and "n" equal to six, the repetition rate of the plasma production is effectively set to 100 Hz. This means that one discharge should be present for every six image pairs. The amount and timing of discharge is predictable and controllable. The Quantum Composer used during this experiment was a 9300 series pulse generator used on continuous mode. It had a frequency range from 0.01 Hz to 10 kHz [23]. An oscilloscope was used to monitor the timing of the camera, laser, and plasma discharge together. A diagram of the overall setup is included below in Figure 16.

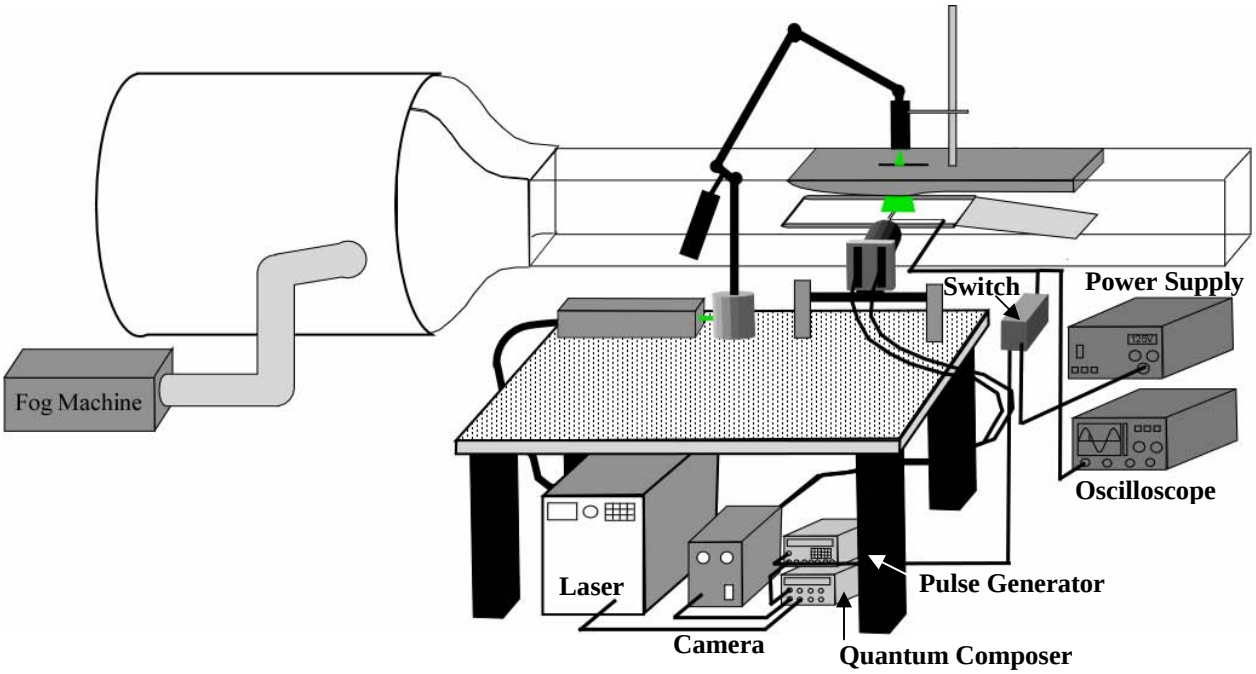

Figure 16. Overall setup diagram

3.6.3 Flow Software. The image pairs were downloaded into the Dantec Dynamics Flow Manager software for preliminary processing. Flow Manager is one program of five in the Flow Map system used primarily for processing and analyzing the flow field. The APX camera and Pegasus laser settings first had to be set properly in the software with special attention in setting the timing between image pairs and the field of view. The pixel dimensions were set to 17 μm x 17 μm. Proper variable settings were necessary or correlations between image pairs would be erroneous. The field of view for narrow field and wide field was set to 18.1 mm and 57.1 mm respectively. Databases were setup to keep track of the recorded data then processed and validated with proper correlations. In addition to Flow Manager, post-processing and data presentation were accomplished with Tecplot. Data are exported from Flow Manager to Tecplot and custom graphs, contours, and animations can be made. Tecplot is utilized for its greater visualization capabilities. Flow Manager also exports data in a format that could be read by MATLAB, which was crucial for analysis.

3.7 Experimental Procedure

Each session began with focusing the image prior to collecting data and verifying the field of view through ruler shots. The tunnel velocity and the amount of suction were determined previously through the validation runs. These were set to operate at Re = 30,000 with just enough pull to create separation along the flat plate. Validation runs consisted of pressure measurements using the new taps in the flat plate and LabVIEW and wide field PIV analysis without the actuator turned on. The pressure measurements also required calibrations to be taken using the dead weight tester through the scanivalve and pressure transducer. The wind tunnel chiller and laser were always allowed to stabilize beforehand for at least an hour.

The main experimental runs were always operated with caution since high voltage was involved. After stabilization, the timing equipment was turned on and the correct settings were verified. Before turning on the power supply, the connections in the circuit and the existence of any shorts were checked. The fog machine was turned on and once the test section was filled with particles, the laser and camera were triggered. 3072 image pairs were acquired and stored to disk for each run. The pulse, voltage, and current traces were monitored and stored on the Lecroy scope. The process was repeated two other times to be able to draw conclusions at that run condition with accuracy. The voltage setting and the effective pulse width were kept set at 8.5 kW and 250ns. These settings were chosen to ensure a consistent and continuous discharge. Four different forcing frequencies were examined: 25, 50, 75, and 100 Hz. The 100 Hz case was taken with the first switch configuration whereas the other three were taken with the new setup. Changing the frequency of the pulse effectively alters the time average power sent to the

electrode as described earlier while keeping the voltage and current constant. Table 2 is a summary of the run conditions. As noted only the frequency of the switch being closed is altered. Therefore for run conditions 1-4, the plasma is expected to form every 24^{th}, 12^{th}, 8^{th}, and 6^{th} frame of the camera respectively.

Table 2. Test Matrix

Run condition	Camera trigger (Hz)	Pulse width (ns)	Voltage (kV)	Switch trigger (Hz)
1	600	250	8.5	25
2	600	250	8.5	50
3	600	250	8.5	75
4	600	250	8.5	100

IV. Results and Analysis

The results section will describe how the three remaining objectives were completed. This includes validation for the new experimental setup, data on the effect of a pulsed DC plasma actuator on separation, and the analysis to determine whether evidence exists that coherent structures are the cause for reattachment. Although two switches were used with different characteristic waveforms, data from both will be presented as the resulting conclusions are valuable. Only representative figures however will be included in this section with supplemental data provided in the appendices.

4.1 Tunnel Validation

A series of tests were performed to validate the new setup and determine the settings under which the experiment would be conducted. This was in large part a trial and error process where only representative data were recorded and processed to justify the decisions made.

4.1.1 C_p Distributions. The contour along the upper wall was designed and manufactured to mimic the pressure distribution along a Pak-B turbine blade. This method was chosen rather than studying an actual turbine cascade, because boundary conditions could be analyzed and imaged easier. A great deal of public literature exists on the C_p distribution found for ideal and experimental turbine blades. In addition to compiling results on different methods of active and passive control, Rivir, et al. [3] also compared the theoretical and experimental data on pressure distributions of a Pak-B turbine blade. The pressure distribution calculated using the Vane Blade Interaction (VBI) code is often used to compare the two data sets. Rivir et al. [3] makes note of the inadequacies of the computational model in predicting separation onset and transition

after separation occurs. The VBI code C_p distribution at Re=100k, the experimental data collected in this paper for Re=25k, and the run condition for this experiment are shown in Figure 17.

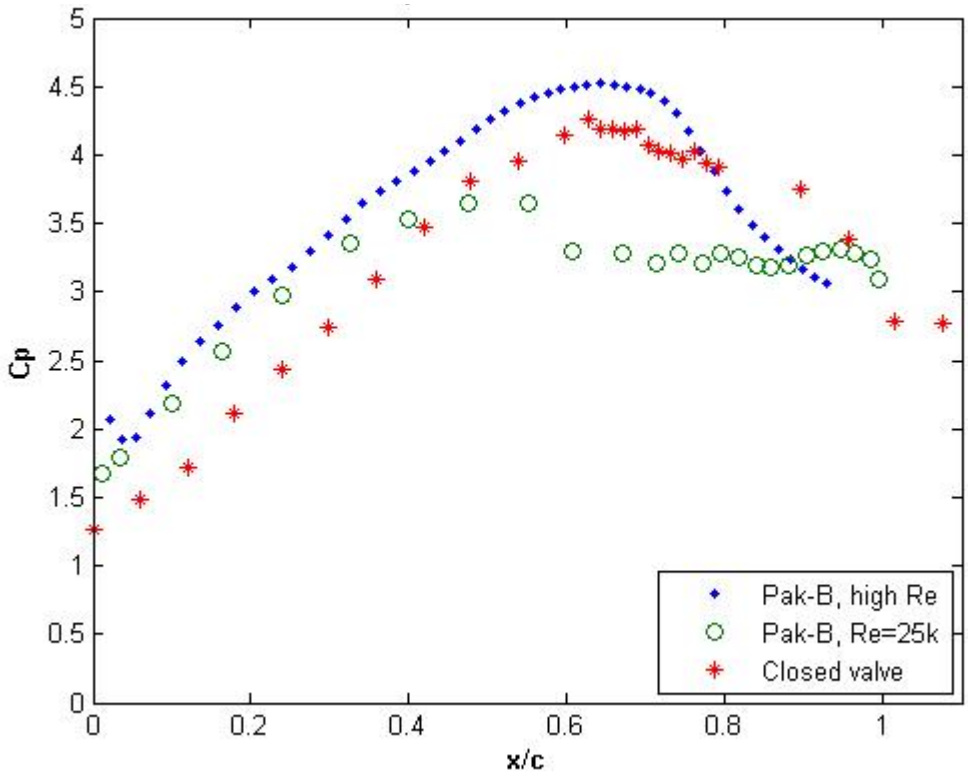

Figure 17. Vacuum condition compared to Pak-B profile

The inadequacies in the VBI code can be seen with the missed location of the loss "knee" and how the measurements still change very gradually after separation compared to the experimental data. The loss knee is indicative of the beginning of the separation bubble. As shown, the C_p distribution for this experiment lies in between the experimental curve and the one produced by the VBI code. For the run condition in this experiment, labeled closed valve, the separation inflection point can be seen at approximately 0.65c, which is around the recorded location for separation on a Pak-B blade. After this point, the graph begins to drop off as losses during transition are occurring. It does appear that end effects exist in the experimental data, but the general

shape of a Pak-B distribution is accomplished and the results are repeatable. This result was necessary to be able to compare the results to existing literature and data that also modeled the Pak-B pressure distribution. The run condition for this experiment is labeled closed valve to distinguish the different settings under which pressure scans were conducted. Certain settings had to be altered to achieve the C_p distribution presented above in Figure 17.

The two major settings that could be altered were the deflection angle of the tail end of the flat plate and the amount of vacuum pulled. As mentioned previously, a piece of sheet metal was added to the end of the flat plate to alter the amount of blockage gradually below the main test section without inducing major turbulence. The tail end could be raised up and down by a threaded rod on the outside of the tunnel. The amount of vacuum pulled could be altered through two valves, one controlling the amount of air passage through the vacuum tubing and the other allocating the amount of air outside the tunnel that is removed. Changing the deflection angle and vacuum setting was a trial and error process that was first tested for repeatability to ensure none of the pressure ports had a leak and all of the equipment was working properly.

Besides producing the general shape and magnitude of a Pak-B pressure distribution, it was desired to operate at a low Reynolds number of 30,000 and have a velocity ratio of the inlet to exit equal to 1.64. A low Reynolds number was chosen to simulate take-off and other low speed conditions, where separation is likely to occur on a turbine blade and the use of plasma actuators would be applicable. The desired velocity ratio was chosen to imitate actual conditions found in experiments with the Pak-B blades and was accomplished by altering the tail deflection angle. The trial and error process of

finding the correct vacuum setting was repeated until all of these goals were minimally compromised. Not all of the data were recorded when the vacuum was applied as it was clear that too much or too little flow was being pulled. Figure 18 shows the pressure distribution taken at three vacuum settings: no vacuum applied, vacuum with closed valve, and vacuum with open valve. The difference between the open and closed valve settings is that the open valve is also pulling air from the test cell and thus less from the tunnel.

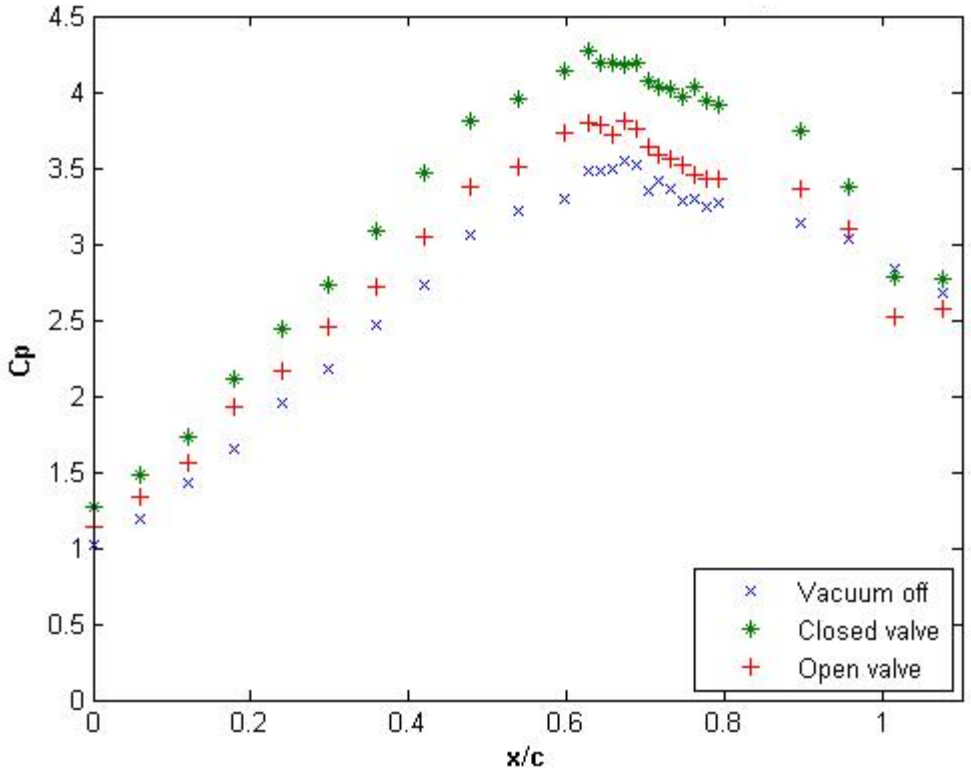

Figure 18. Pressure distribution for various vacuum settings

The separation knee is not as evident at the other vacuum settings and the curves do not obtain the same magnitude as the closed valve vacuum case. With no vacuum setting applied, separation on the flat plate was not consistent and the flow along the upper contour was not attached. With the open valve setting, it was still not obvious that

separation was occurring. Preliminary flow visualization and PIV presented in the next section were used to further justify the amount of vacuum needed along the flat plate.

4.1.2 Flow Characterization. The C_p distribution is good for comparison to public literature but is limited in what it can tell about instantaneous flow quality, uniformity, and characteristics. In order to obtain and document greater physical insight into the nature of the flow field in the test section, wide field planar laser scattering techniques were applied, including flow visualization and PIV. Flow visualization refers to visually using the camera images to determine the flow conditions. This technique is useful but a more quantitative method is necessary. PIV refers to the analysis conducted on the images to verify the visual conclusions made. Through both methods, the uniformity and stability of the flow was characterized and the run conditions chosen were further justified. Figure 19 is a representative wide field flow visualization image at the chosen closed valve run condition. Reflections from the laser on the electrodes, flat plate, and upper contour can all be seen. PIV images were often processed with an attempt to minimize these effects and the area where the laser sheet cutoff was neglected. The images were also rotated around the y-axis so that the processed plots have the flow going from left to right.

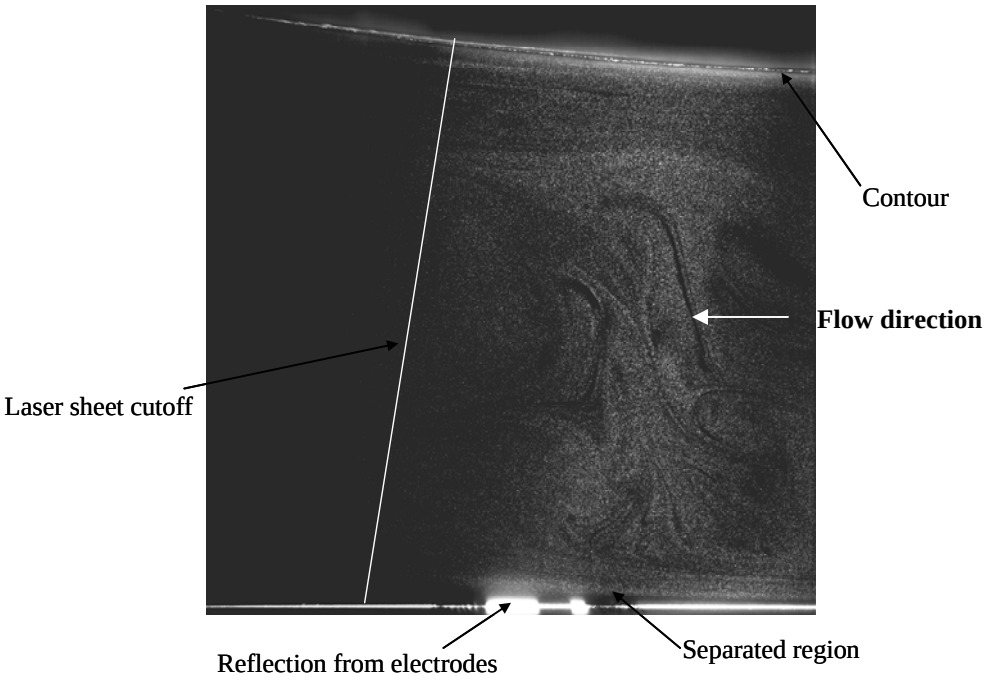

Figure 19. Wide field characterization setup

Streamline analysis was conducted to ensure only a slight upward velocity was being induced by the vacuum while maintaining flow attachment along the upper contour. Figure 20 presents two streamline images that show the slight difference that was needed with having the vacuum on. The top streamlines show how the flow goes along the contour instead of with the free stream. For both the no vacuum and vacuum case, there is a slight upward velocity from just the expanding test section.

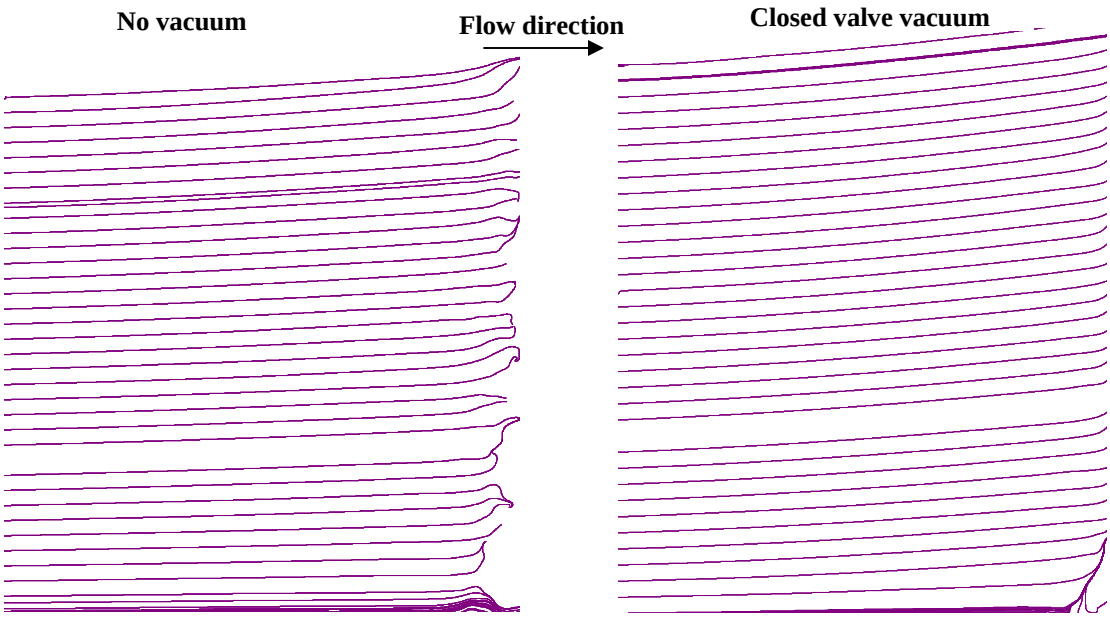

Figure 20. Comparison of no vacuum and vacuum streamlines

The streamline images cannot however show much detail for the boundary layer and separation region along the flat plate. In Figures 21 and 22, velocity contour maps with vectors overlaid on top are included for the vacuum and closed valve vacuum condition. These images further validate that the flow is moving along the contour more with the vacuum on. More importantly, the magnitude and direction of the free stream velocity vectors are not being altered significantly. The color scale above is the velocity in m/s. The free stream velocity is approximately 2.5 m/s. The green color on the top and lower part of the contour shows roughly where the flat plate and contour are in the image.

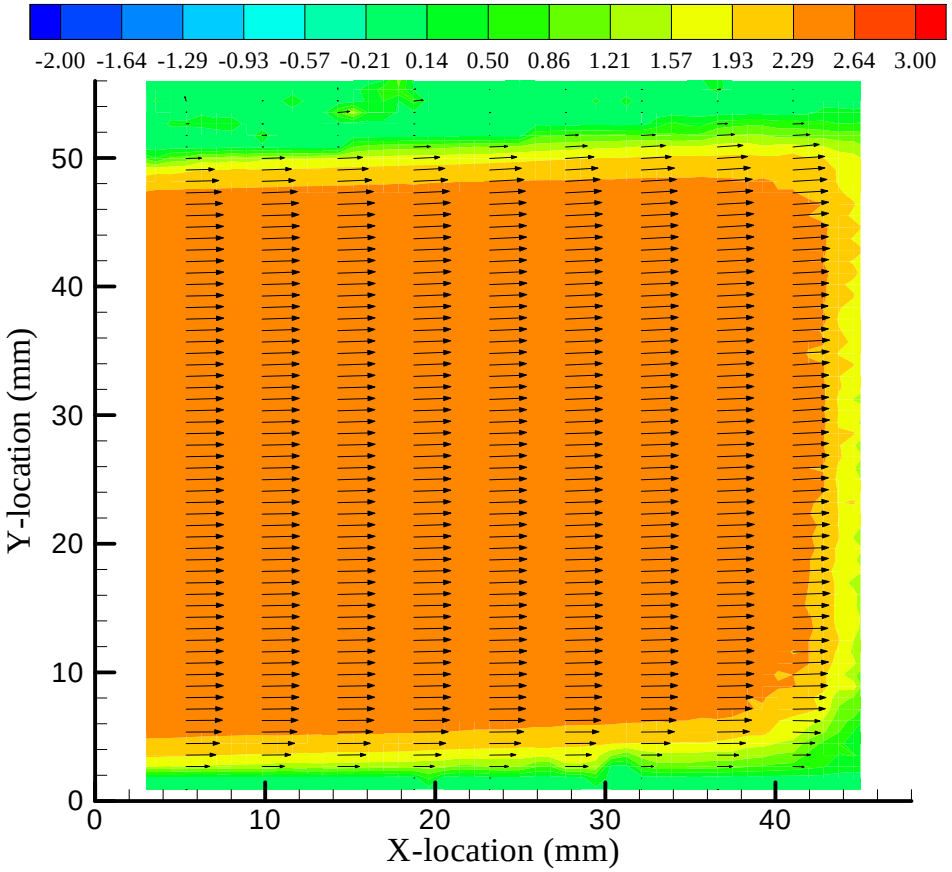

Figure 21. Velocity contour for no vacuum condition

The arrows along the upper part of Figure 21 remain relatively straight compared to the shape of the contour at this location indicating separation. The small boundary layer along the flat plate and flow visualization images also indicate that separation has not occurred in this no vacuum condition along the plate. The same color scale was chosen for the closed valve condition to compare the boundary layer thickness along the flat plate and upper wall. Along the contour, the velocity vectors are canted more upwards and the boundary layer is thinner. Comparing the contour plots with flow visualization images, the closed valve condition consistently kept the flow separated along the flat plate. Boundary layer profile plots further justify the vacuum setting by showing the change in boundary layer thickness along the flat plate and the uniformity of

the flow in the main test section. Appendix A includes streamline and contour plots for the open valve vacuum condition for comparison.

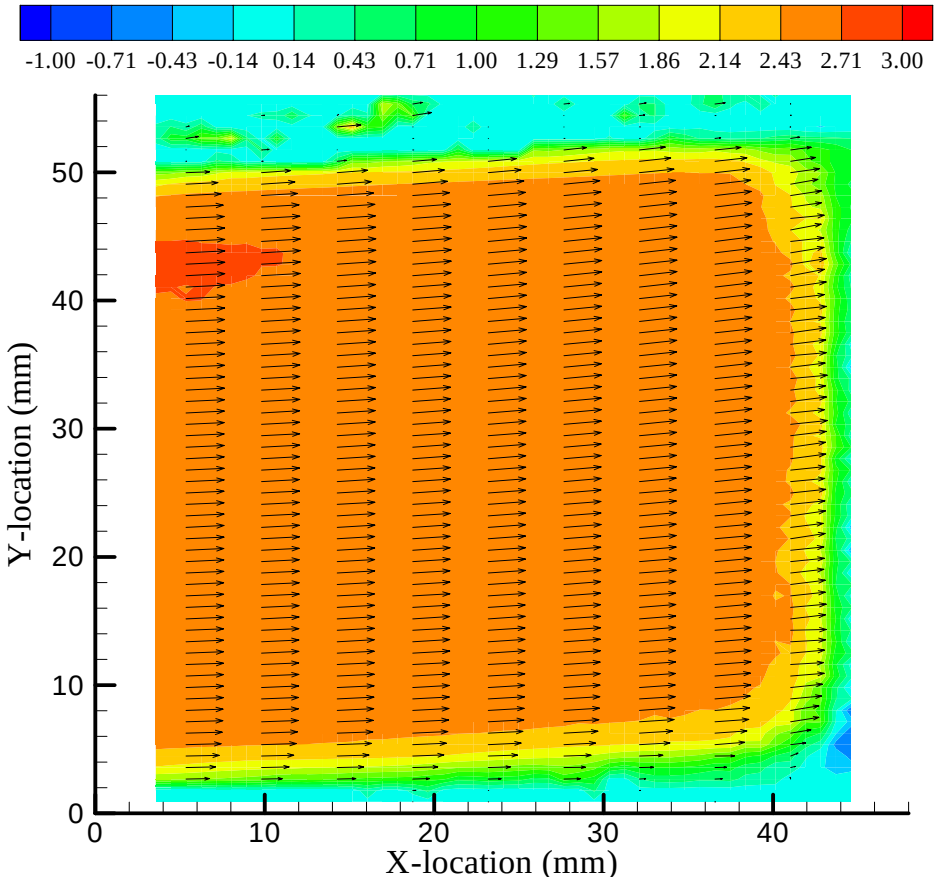

Figure 22. Contour plot for closed valve vacuum condition

The boundary layer plots were made by first exporting the data from Flow Manager to text files. The text files were a large matrix consisting of information on the position and velocity of each vector in the flow field. The plots are a graph of the U-velocity as a function of y-location averaged over ten different columns in the image. Therefore the profile does not represent any real location in the flow but the graphs are useful to examine their general shape. The U-velocity is normalized with the free stream velocity and the y-location is normalized with 99% of the average boundary layer thickness, $\delta_{.99}$, which is approximately 6 mm. Figure 23 is a boundary layer profile plot for the closed valve vacuum case.

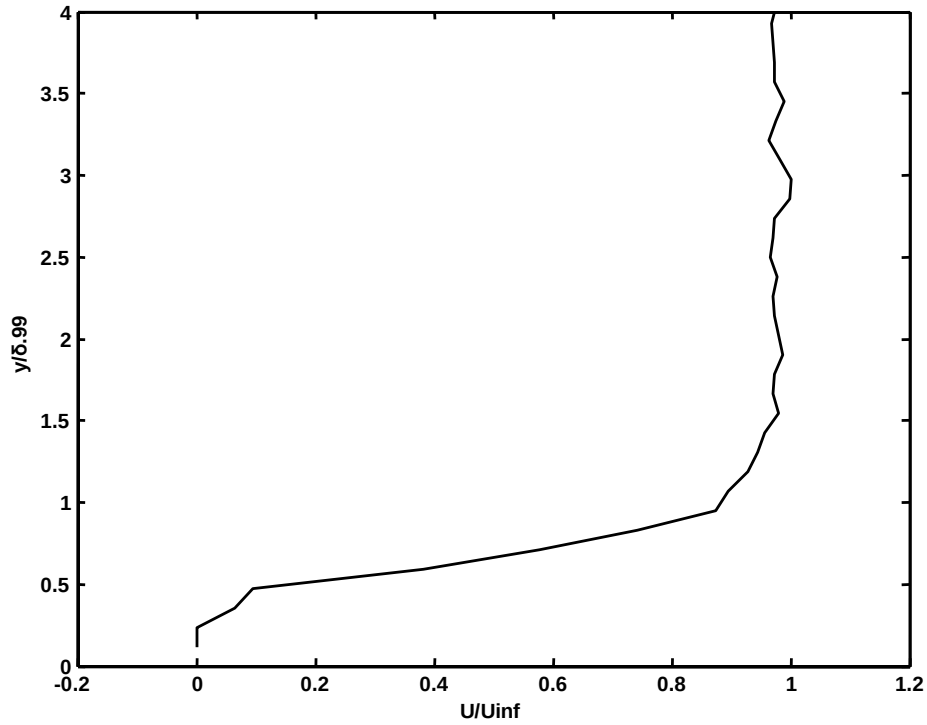

Figure 23. Boundary layer plot for closed valve vacuum condition

As shown the profile plot includes noise from the flat plate and therefore not much detail is shown close to the wall. The same plots will be included later in this section for the narrow field lens for the actuator on and off. In these plots it is clearer that separation is occurring on the flat plate as the boundary layer reverses direction.

Figure 24 is a graph of the boundary layer plots for the no vacuum condition graphed with the closed valve case presented in Figure 23. Plotting these on both the same graph gives an indication of how little the flow within the main test section was altered. Also, flow along the flat plate appears to become separated for the vacuum profile in comparison to the other. This can be seen more clearly by zooming on the graph but noise from the flat plate still does not allow much detail to be shown. The validation graphs are important in characterizing the flow conditions and justifying certain settings, but they are also useful in determining day to day repeatability.

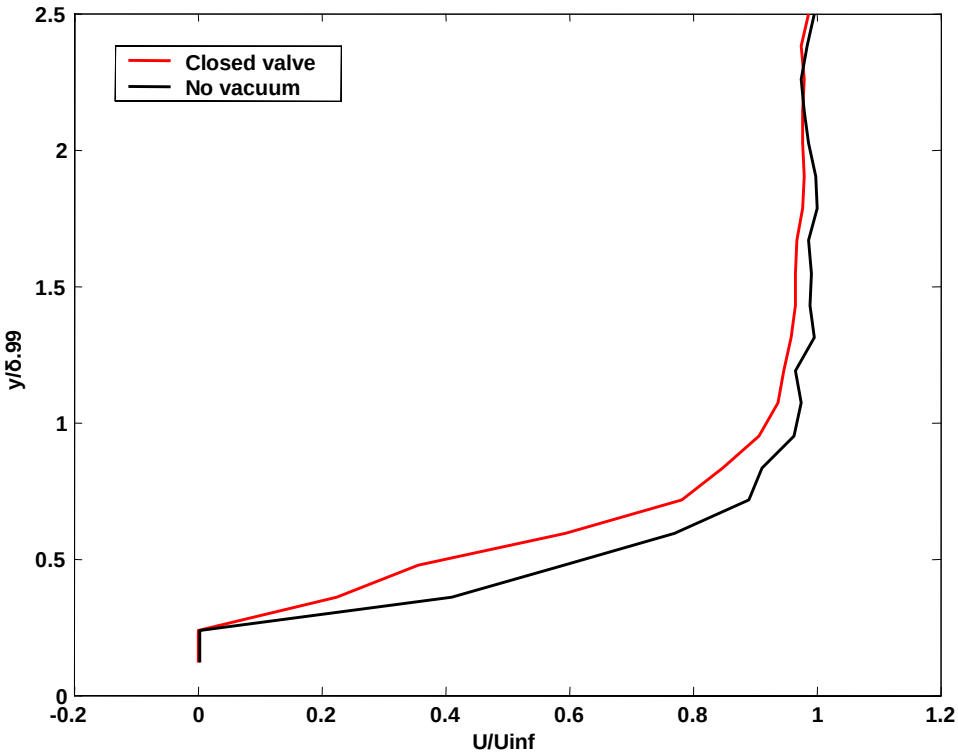

Figure 24. Comparison of boundary layer plots for vacuum settings

4.2 Plasma Effect on Separation Location

Flow visualization was first used in determining if the actuator was having any effect on the flow. With the narrow field camera lens, it became clear that flow was separated along the flat plate. For the baseline case, seeding was consistent except for the separation region right above the actuator. In this location, seeding particles could be seen rotating or were sometimes stagnant, also indicative of separation. In all cases when the actuator was turned on, the flow would reattach for a certain amount of time and then would appear to be ineffective. Through just flow visualization it seemed the separation location was only moved to the end of the bottom electrode. It however was impossible to verify this as the plasma appeared to be vaporizing the seeding particles directly behind the bottom electrode. Figure 25 shows two representative flow visualization images with the actuator off and on respectively. The baseline case PIV analysis was

done using the vector statistics of all the image pairs whereas analysis for the actuator on had to be accomplished with select images in which reattachment was occurring. This was the case because the vector statistics for when the actuator was turned on would average both the images where the plasma seemed ineffective with the ones that appeared to be changing the separation location.

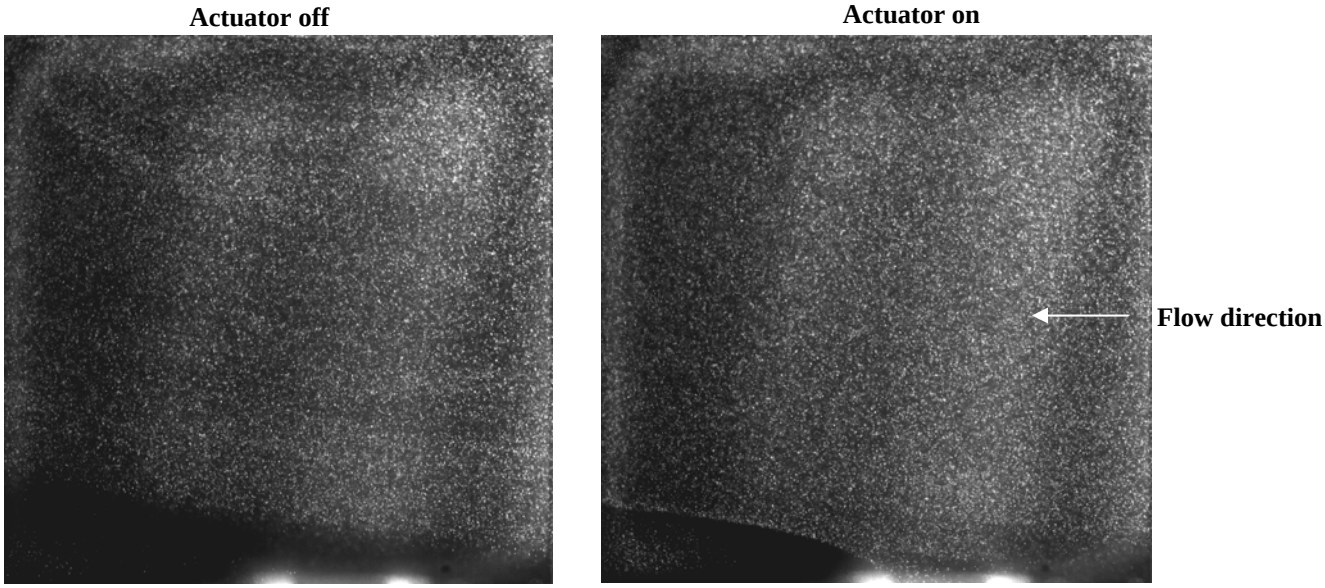

Figure 25. Comparison of flow visualization images

The PIV streamline analysis also reveals the apparent change in separation location. Figure 26 shows the two streamline images with the axis flipped such that the flow is going from left to right. The general location of the electrodes is shown as a black box at the bottom of the figure. The streamlines appear to show that the plasma is pulling down on the boundary layer before the actuator location but does not appear to affect the flow aft of the electrodes. It cannot be stated with certainty however that the streamlines shown for the flow aft of the actuator are accurate. Due to the lack of seeding in this location, a large percentage of the vectors in this region were considered invalid. The streamline analysis however does show that the plasma does not have much effect on the free stream when it is compared to the baseline case. The image presented in the

figure is for the 50 Hz case, but there was no apparent change in the streamline analysis for the other conditions.

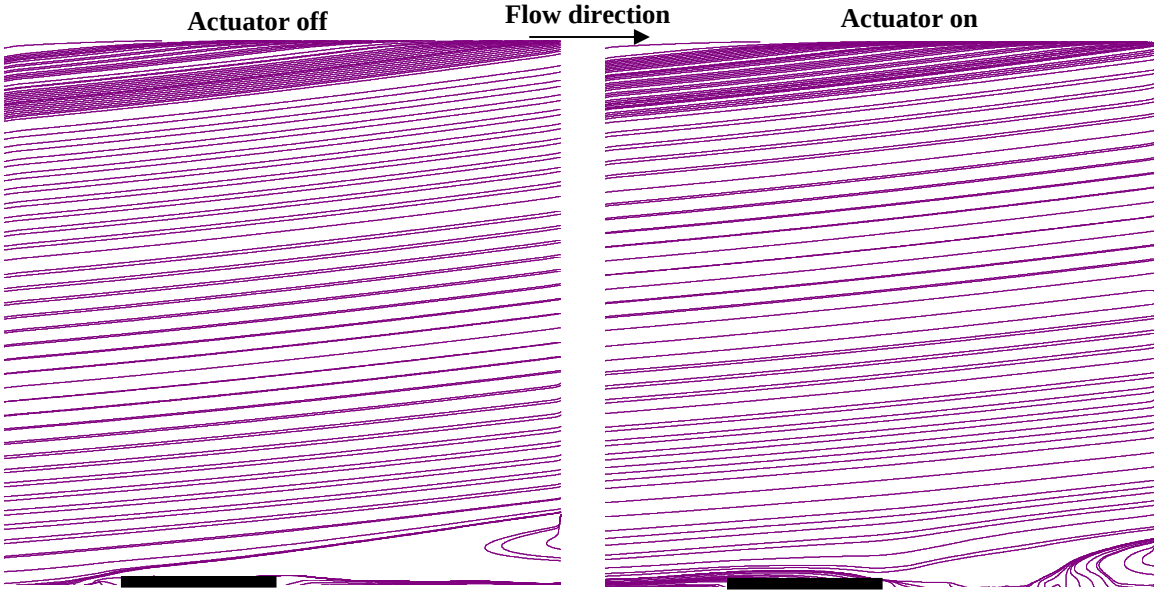

Figure 26. Comparison of streamline analysis

Profile plots can also be used to compare the plasma effect on the flow with the baseline condition. As the same method used for validation, Figure 27 is a graph of the normalized streamwise velocity profiles for both the cases of the actuator on and off at 25 Hz averaged over ten different columns of the images. The images processed for these profiles however are with the narrow field camera lens and therefore more detail is shown closer to the wall. There are still laser reflections from the actuator and therefore there is not distinguishable difference between the two profiles close to the flat plate due to this additional noise. The profile plots show more the order of magnitude the plasma has on altering the boundary layer. Again this trend was consistent for all run conditions.

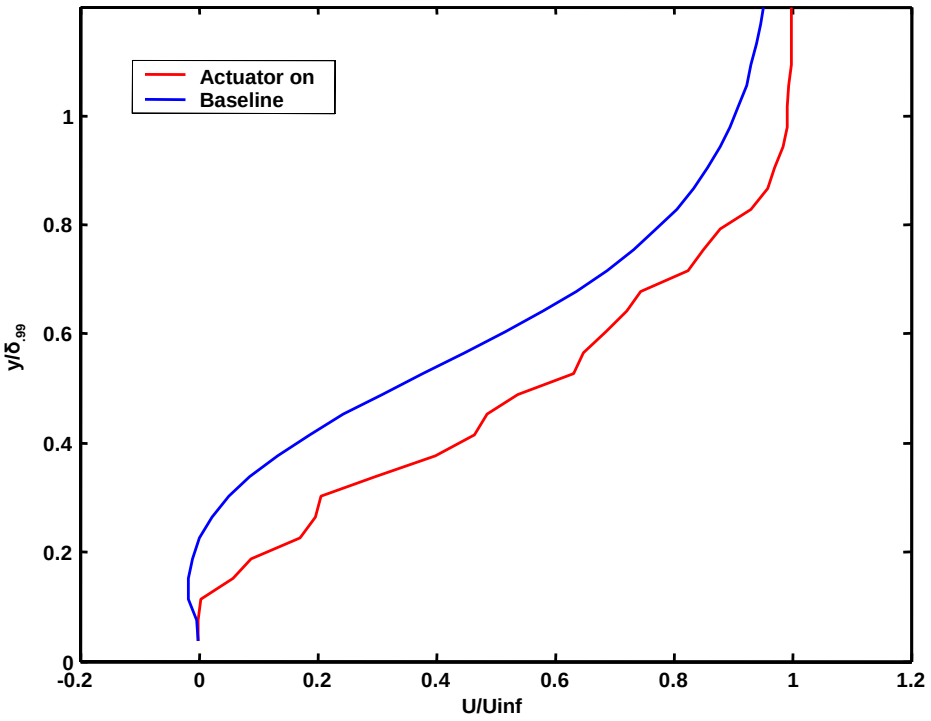

Figure 27. Comparison of profiles for baseline and with plasma

The velocity field contours also reveal the effect the plasma is having on the boundary layer. Figure 28 compares the two velocity contours for the baseline and actuator on at 100 Hz on the left and right respectively. The same scale above the two contours is used to compare the differences. There is a definite change in boundary layer thickness and there appears to be a slight inflection in the velocity contour around the actuator location. Although it was clear through this preliminary flow visualization and analysis the actuator was having an effect on the boundary layer and separation location, reattachment was not consistent. Further analysis is required to determine if the frequency of these separation and reattachment events is indicative of the existence of organized vortical structures created by the plasma. Appendix B includes streamline figures, boundary layer profile plots and the velocity vector contours at the other frequencies not presented for comparison.

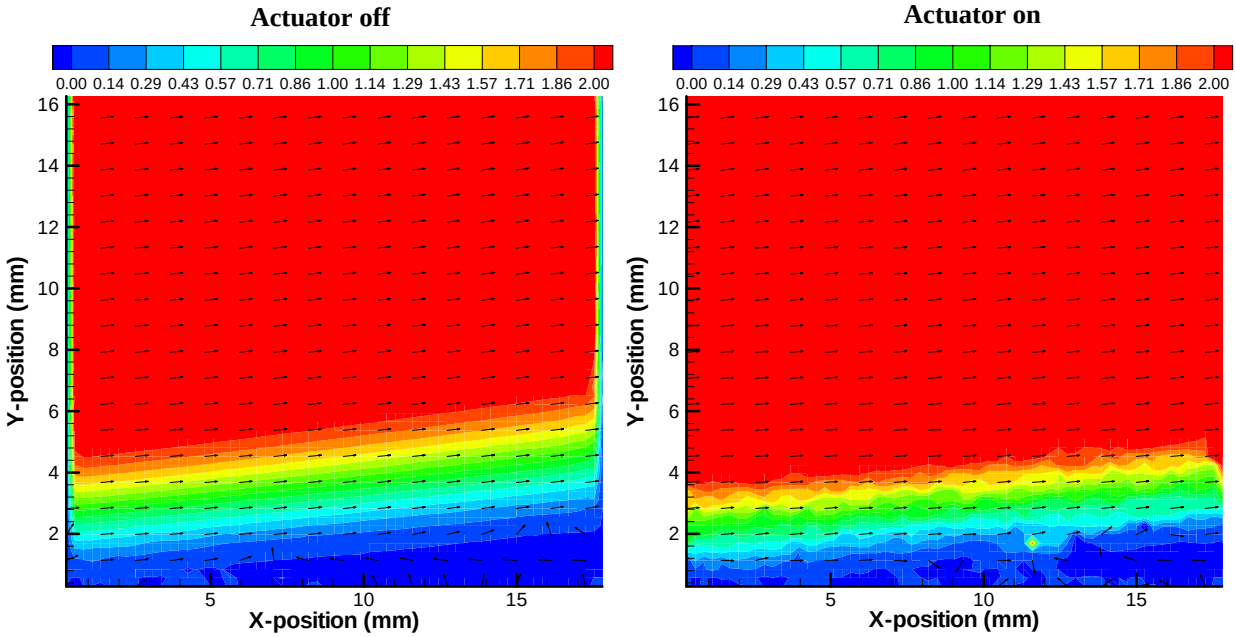

Figure 28. Comparison of velocity field for baseline and with plasma

4.3 Velocity Contours

One of the objectives of this research project was to find evidence to support or contradict the existence of coherent vortical structures as the mechanism in which pulsed DC plasma actuators control separation. As shown in the previous section, the actuator appeared to move the separation location only a part of the time. It did not appear through flow visualization that these separation/attachment events were occurring at the frequency of the switch. It was therefore desired to systematically determine if some characteristic frequency did exist. If this were the case, it would support the existence of vortical structures propagating behind the actuators creating reattachment. These coherent structures have been found to reenergize the boundary layer and reattach the flow in an organized predictable manner for AC plasma discharge actuators.

If vortical structures existed, their propagation downstream would also cause the above free stream to fluctuate with the frequency of their occurrence. Some rising and

falling of the flow behind and above the actuator would exist as the structure proceeded downstream. It was therefore desired to examine a particular area of the flow over time. The method chosen to accomplish this was to define a velocity contour that responded to the actuator. The velocity contour is the locations where each column of the image reaches a chosen percentage of the free stream velocity. The seventy percent contour is shown in Figure 29 for both the baseline and actuator on condition at 100 Hz. As expected, the actuator effectively increases the velocity closer to the flat plate.

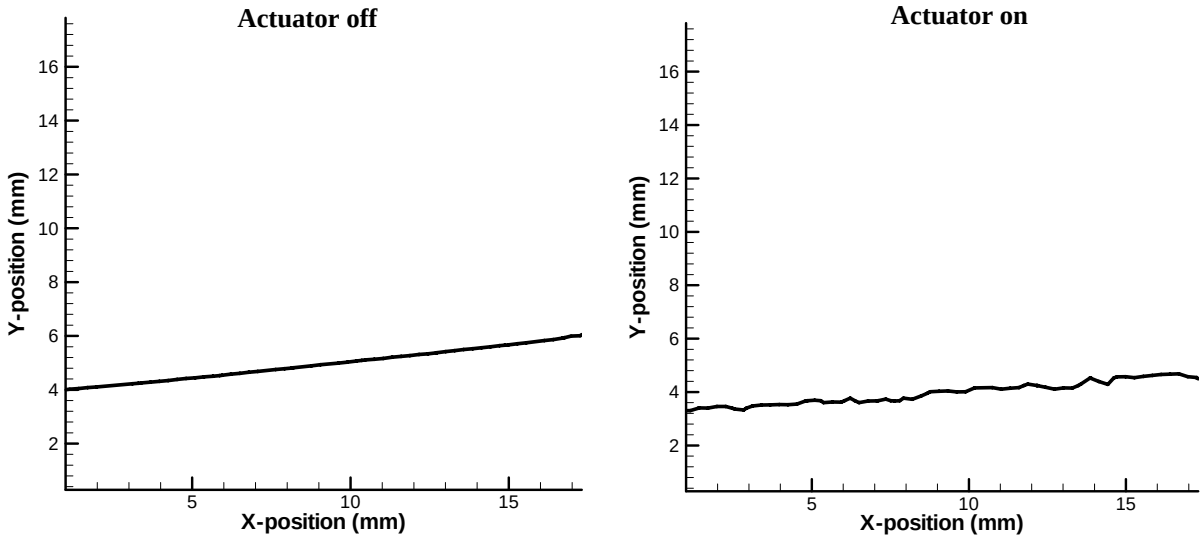

Figure 29. 70% velocity contour

The imaging software could be used to animate through each image to reveal how the velocity contour is changing over time. Other velocity contour values were examined but 70% was chosen for the remaining analysis. The other contours displayed the same behavior with the difference being the magnitude of the y-location. Very low contour values however would display larger fluctuations when analyzing the separated images. Figure 30 is an average of the 70% contour over a series of images for both the baseline and actuator on conditions. Appendix C includes the 70% contour averages for the other frequencies and a sample of the other velocity contours that were examined.

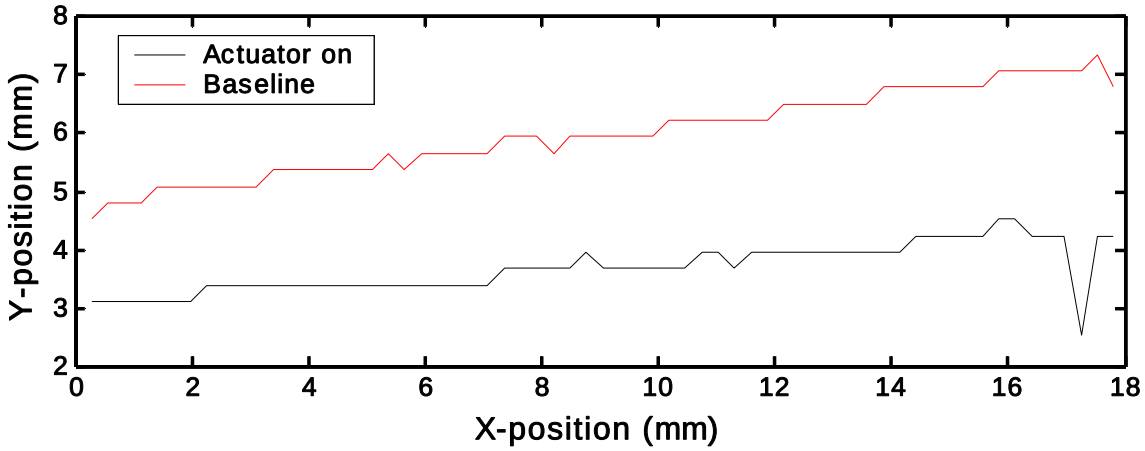

Figure 30. Comparison of average 70% contour

Velocity vector data was exported from the processing software to be analyzed with MATLAB. At first, MATLAB was used to graph particular columns of the contours for a series of images. The contour percentage, column numbers, and the set of images could be easily altered within the script. The individual columns were first examined to determine if the fluctuations seen through the flow visualization was in fact real and consistent throughout the images. Figures 31 and 32 are graphs of the seventy percent contour at three different column locations over 500 images for the baseline and 100 Hz actuator on case respectively. Different sets of images were also examined to ensure results were similar. As shown the different column numbers only change in magnitude as expected from boundary layer thickness increasing further downstream. Some noise exists in the figures as seeding varies from image to image affecting the vector information being analyzed. As shown, a natural fluctuation exists in the tunnel without the actuator being turned on and therefore it was necessary to compare all analysis to the baseline condition.

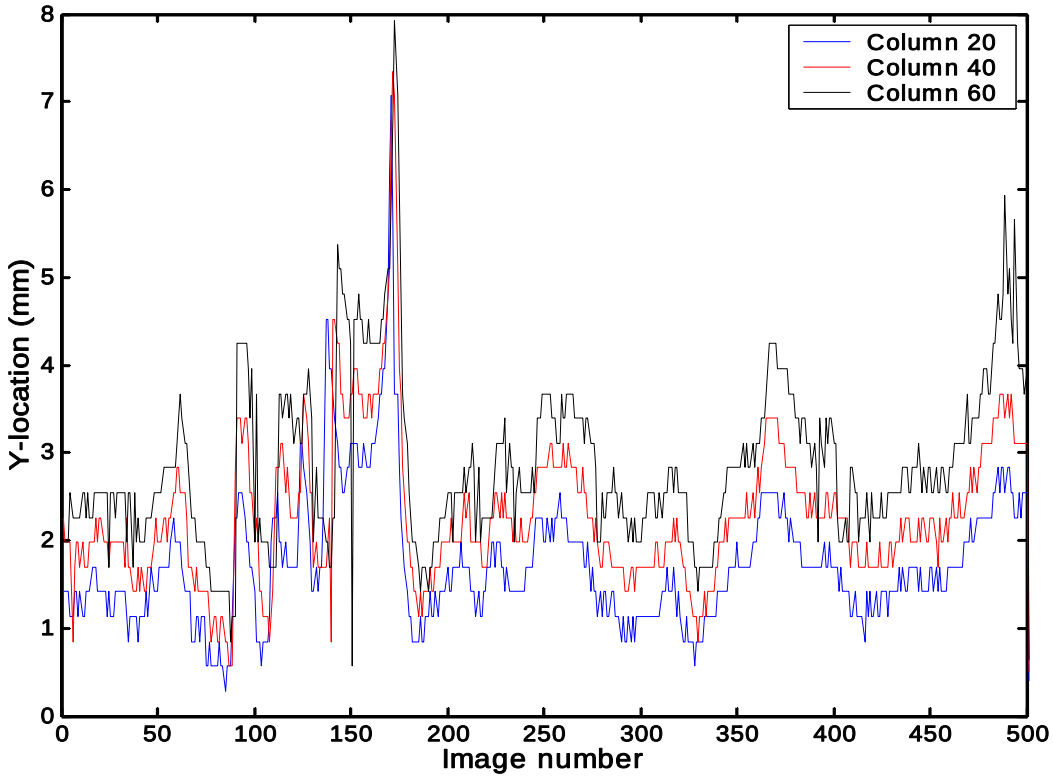

Figure 31. Baseline contour analysis

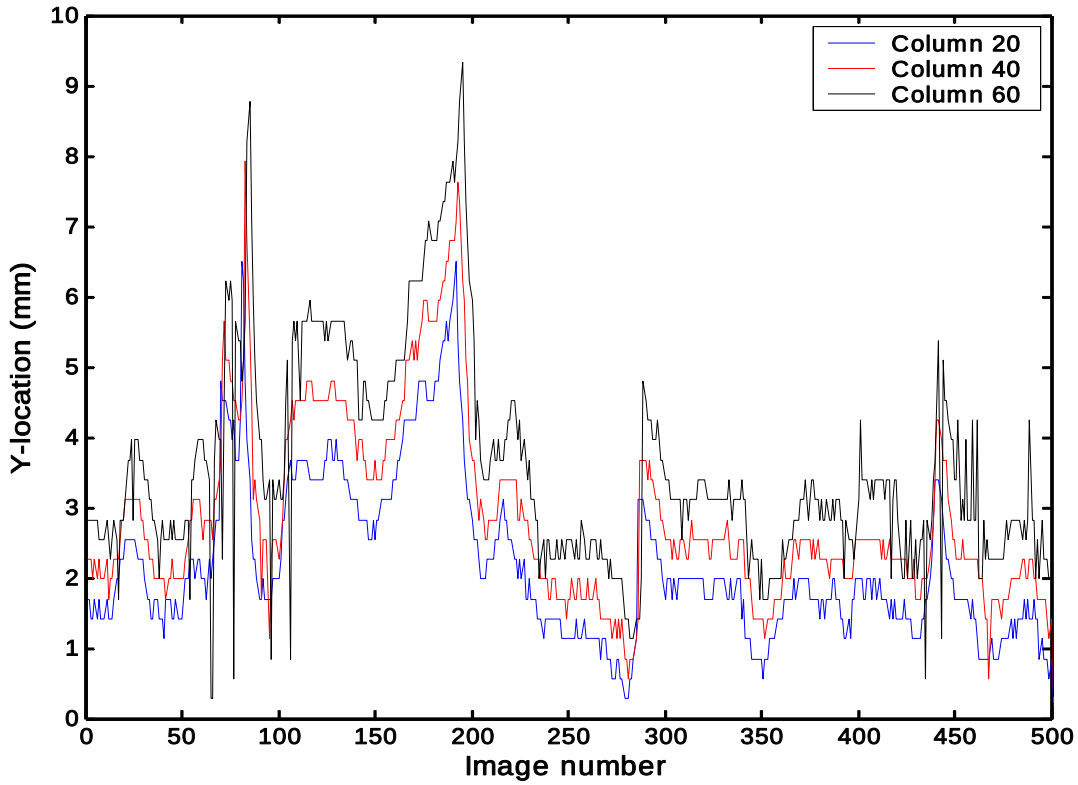

Figure 32. Actuator on contour analysis

It is difficult to determine a characteristic frequency from the graphs above or if one even exists. Efforts were focused on examining one column at a time. MATLAB was used to perform a FFT on the data and create a power spectrum. Figure 33 is a power spectrum for five different series of images for the baseline condition at Column 40. Each series consisted of 512 different images. The image numbers were changed to time by using the camera trigger of 600 Hz. The power spectrum provides a relative intensity for the frequencies that dominate the flow. As shown, the power spectrum reveals a strong zero frequency tendency as the fluctuations do not have a strong control over time on the characteristics of the flow. There does appear however to be other dominate frequencies at around 10 and 20 Hz.

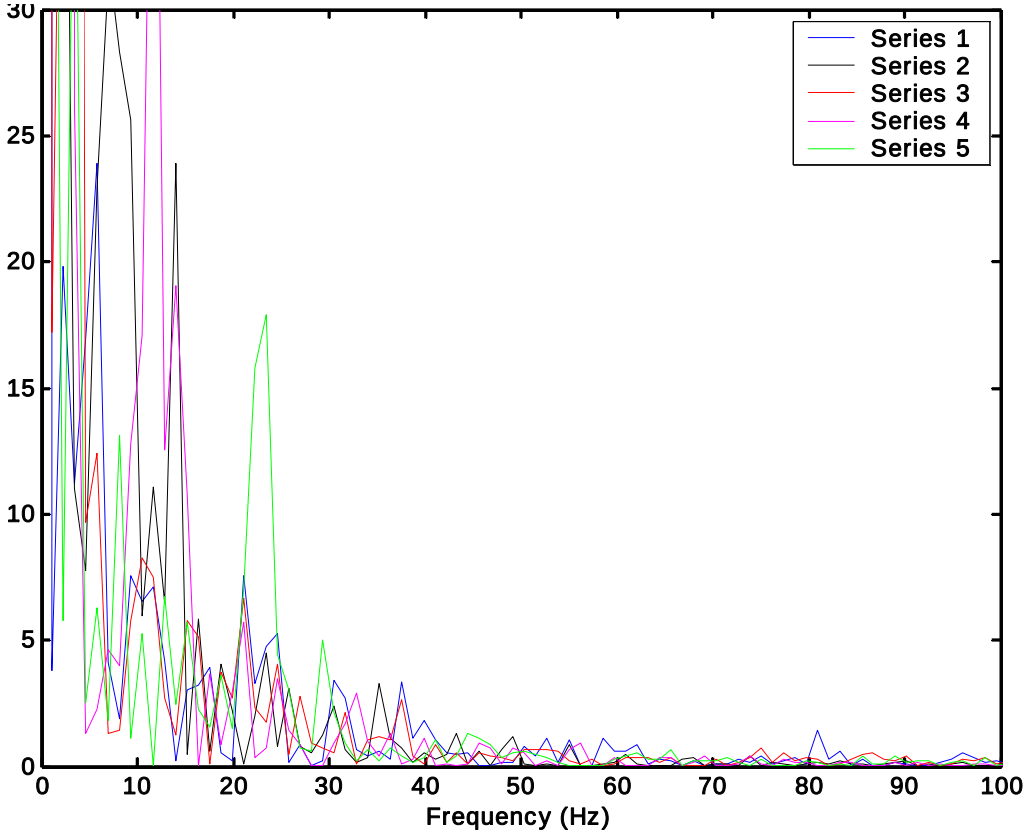

Figure 33. Baseline power spectrum (Column 40)

These secondary frequencies can be seen more clearly when the averages of the different series are plotted. Figure 34 is the average of the five different series presented in Figure 33. Power spectrums at other representative column numbers are included in Appendix B. All of the column numbers chosen were located behind the bottom electrode.

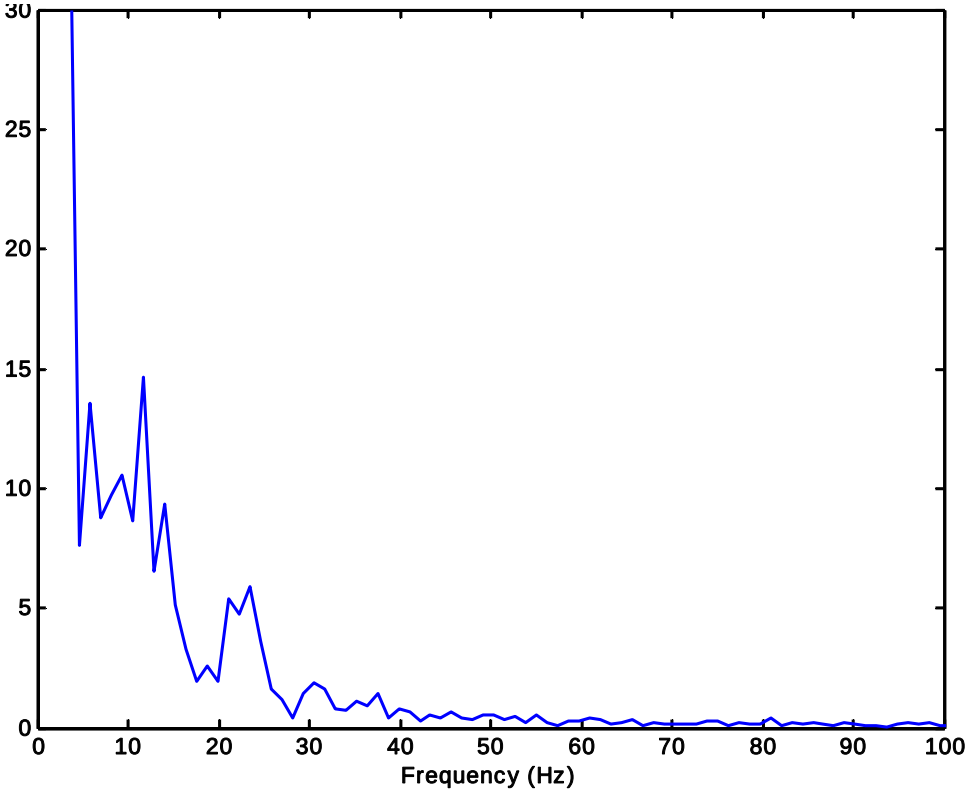

Figure 34. Average baseline power spectrum (Column 40)

The same script was run for the different series of images for the actuator turned on. The graphs were examined to determine if any other extraneous frequencies existed compared to the baseline condition. It was desired to determine if the plasma was causing the velocity contour to respond in a different matter due to the development of vortical structures. Figure 35 is one of the representative runs at 100 Hz graphed with the baseline condition. Three runs were taken for each condition to determine if there was any day to day variation. Similar to the baseline condition, a large zero frequency component was present. In general the actuator followed the trend of the baseline

condition as far as which frequencies dominate and only differed in the relative power of these frequencies.

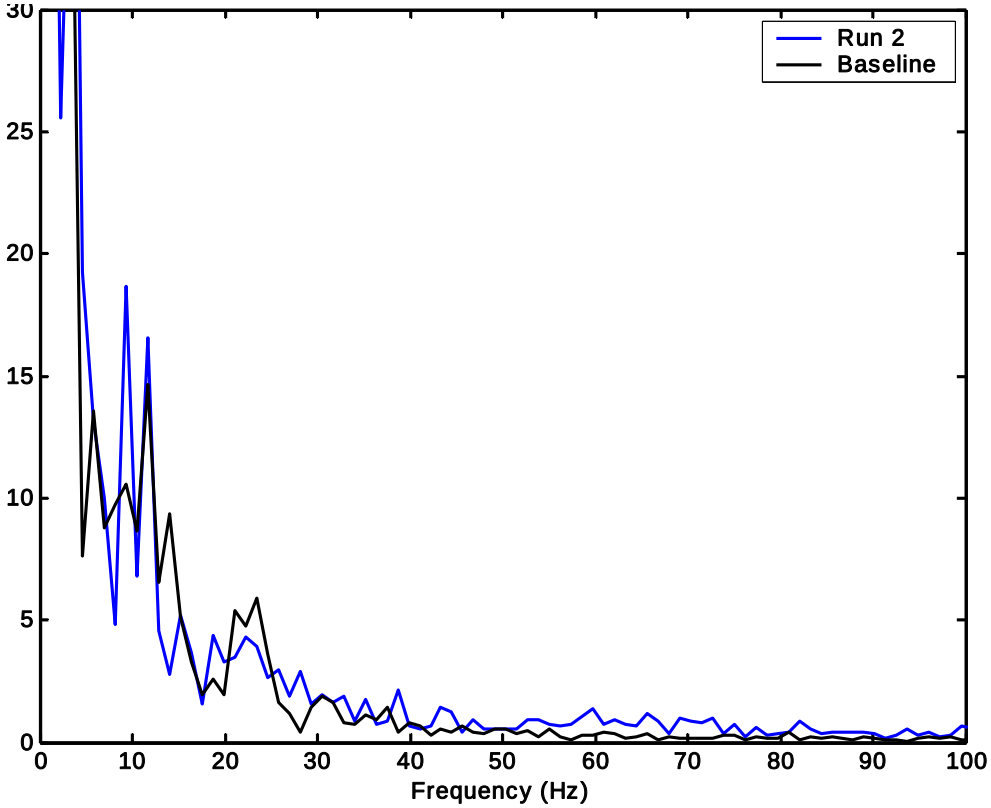

Figure 35. Comparison of average power spectrums

Figure 36 is a zoomed in image of Figure 35 to reveal more the overlap of the two graphs. This further supports the conclusion that no extraneous frequencies exist for when the actuator is turned on. Other series of images and different runs were examined in detail to ensure this was always the case. The plasma does not appear to significantly affect the flow above the actuator in a repeatable organized manner. It does not appear to create any fluctuations that overpower the existing variations in the flow. Appendix D contains average power spectrums for the other frequency cases and at two other column locations. The different run conditions varied the relative strength of the frequencies found but did not introduce any additional frequencies.

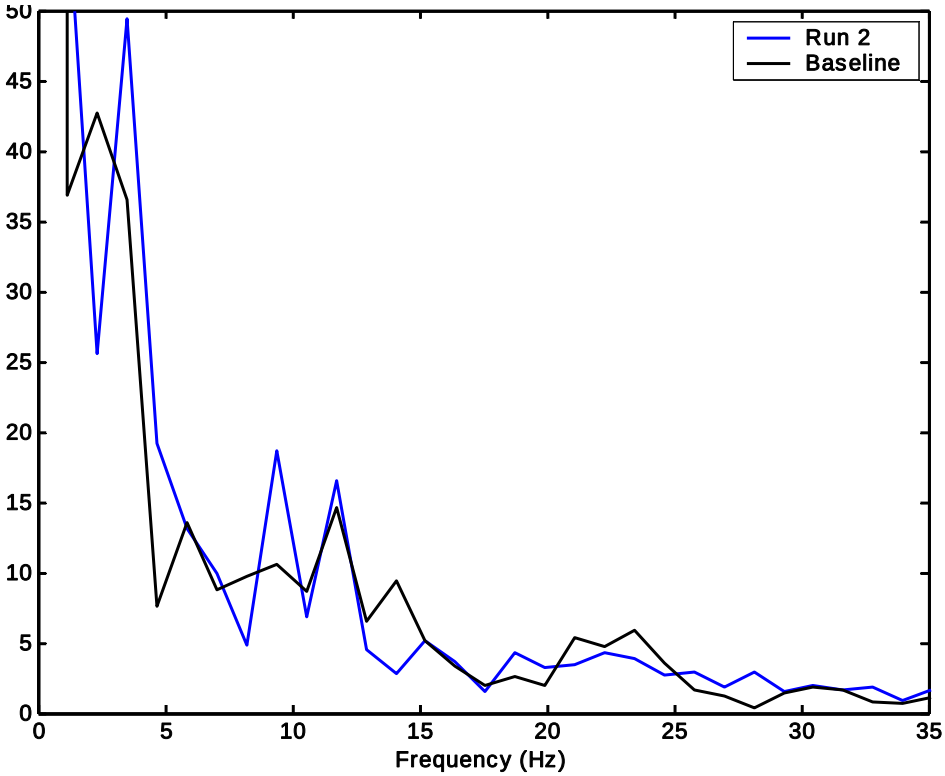

Figure 36. Zoomed comparison of average power spectrums

V. Conclusions and Recommendations

5.1 Research Objectives

The first objective of this research project was to improve the existing AFRL/PRTT facilities and experimental setup. Previous studies there focused on AC plasma actuators and therefore the different pieces of equipment first needed to be changed and tested. The HV switch was redesigned as well as the contour along the upper wall to create the pressure distribution similar to a Pak-B turbine blade. A more permanent structure that could also be easily removed for access into the main test section was manufactured. Also the previous method of taking pressure measurements needed to be refined. Pressure taps were put along the flat plate and clustered at the throat to more accurately determine the C_p distribution. An extension on the flat plate and upper contour were created to reduce the amount of turbulence and end effects in the test section while being able to control the amount of flow below the flat plate. Lastly, a glass insert was designed to improve image quality.

The second objective was to validate and document the new experimental setup. The results showed the pressure distribution was very similar to a Pak-B with suction used to create separation on the flat plate. The flat plate therefore simulated the surface of Pak-B blade at a low Reynolds number. PIV and preliminary analysis revealed relatively uniform flow within the main test section. All characterization was documented in detail to ensure this experiment would be repeatable. The third objective was to collect data on a pulsed DC plasma actuator for four different forcing frequencies. The voltage and current for these cases were all similar but the time average power was altered by changing the frequency. For all cases, the plasma was effective in reattaching

the separated flow along the flat plate and decreasing the size of the boundary layer for a portion of the time. Changing the frequency did not appear to have any effect on the duration of these reattachment events but rather only the number of occurrences throughout the data set.

The last objective focused on determining if some frequency was being induced by these reattachment events. If a frequency existed behind and right above the actuator this would indicate some organized structure. Vortices have been produced in AC studies and have been found to propagate downstream originating at the actuator. Velocity contours were studied to compare the power spectrum with the actuator on and off. No additional frequencies were found at any run condition. The plasma does not appear to create any fluctuations that overpower the existing natural frequencies of the flow. Therefore no evidence was found that coherent structures were responsible for controlling separation at these conditions.

5.2 Research Improvements

The following recommendations are included to further validate the conclusions found from this experiment and offer suggestions for carrying on this study. First, it is suggested that this experiment and all following studies be conducted with solid seeding. This experiment utilized seeding from a fog machine which was simply vaporized by the thermal effects of the plasma. No imaging directly behind the actuators was therefore useful and the resulting analysis had to be tailored due to this fact. Changing the seeding entails major changes to the setup as a new insert and collection pool would be necessary and safety procedures would need to be determined. Another method of correcting this issue would be to insert smoke right before the actuator on the flat plate. This alteration

would have to be made with care also to ensure the flow is not tripped by this additional slot.

Continuous studies can include determining if there is a point in which altering the frequency of the switch has no further effect on controlling separation. Perhaps a frequency exists that keeps the flow attached the entire time. Also the effects of changing the pulse width and voltage setting could be examined. Lastly, this experiment could be repeated with various combinations of non-inductive external resistors keeping in mind the limits of the switch.

Appendix A: Open Valve Vacuum Plots

In addition to the vacuum condition chosen, the open valve vacuum was examined and analyzed in detail. This condition differed only slightly from the closed valve vacuum in that the vacuum also pulled air from the test cell. It therefore did not provide as much suction for the tunnel. These graphs are included to supplement the previously presented figures and to further justify the chosen vacuum setting.

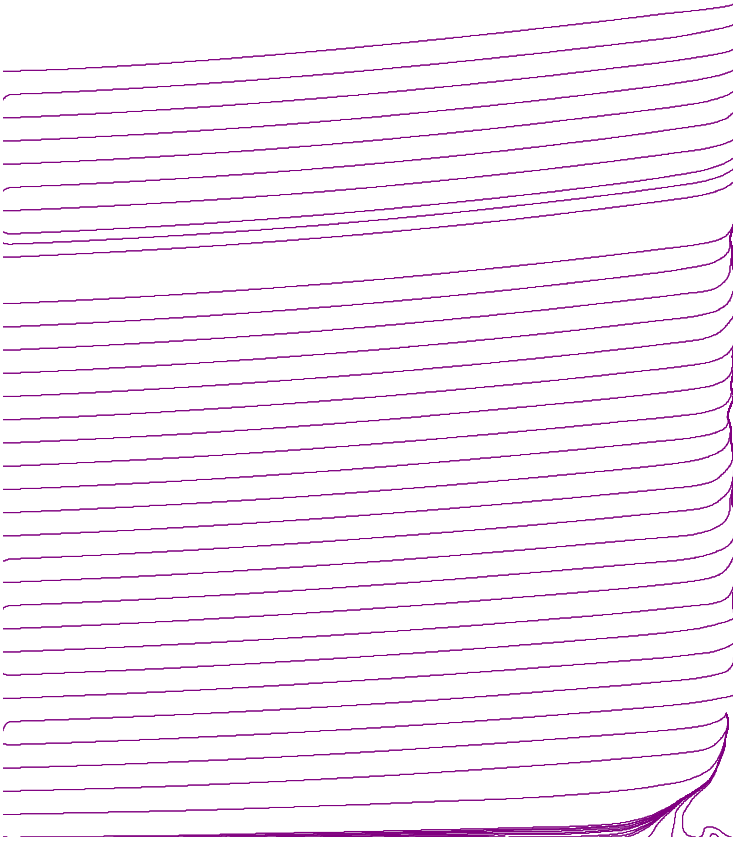

Figure 37. Open valve streamlines

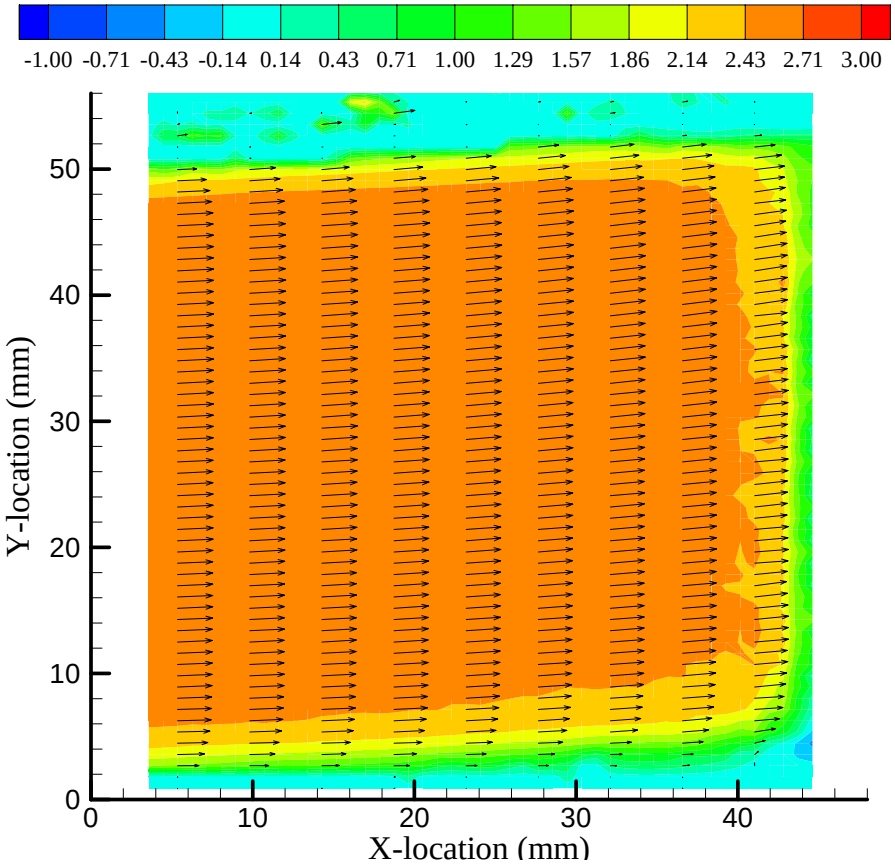

Figure 38. Open valve velocity contours

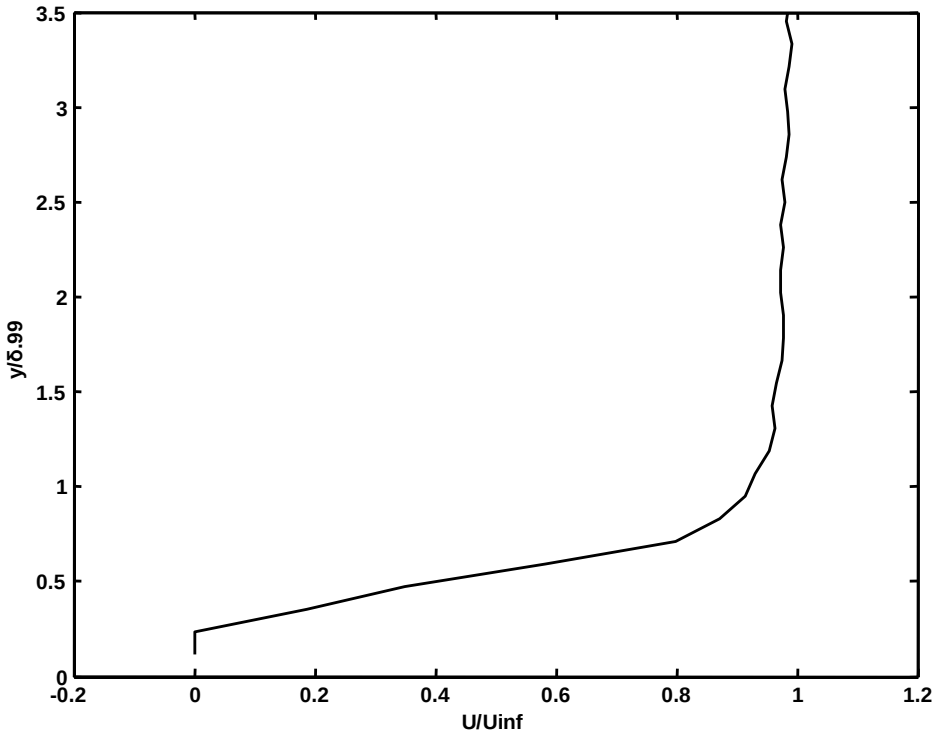

Figure 39. Open valve boundary layer profile plot

Appendix B: Supplemental Data for Various Frequencies

The data presented below is for the other frequencies investigated but were not presented in the main results. The following plots include: streamline analysis for 25, 75, and 100 Hz, boundary layer profiles for 50, 75, and 100 Hz, and velocity vector maps for 25, 50, and 75 Hz. All of the data below is similar to that presented in the results section and therefore no additional conclusions were drawn from this information. The data is rather for thoroughness and additional support for the conclusions made.

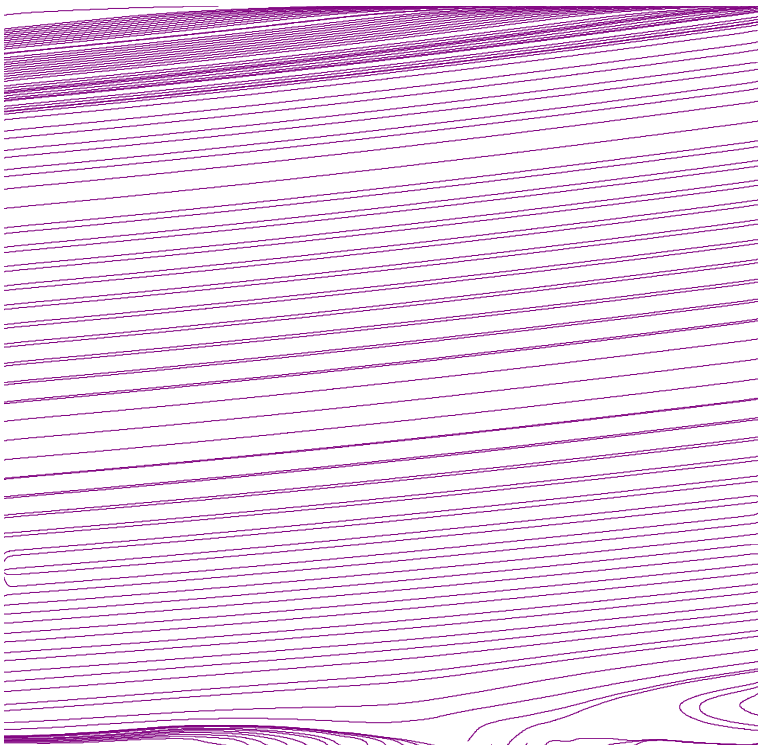

Figure 40. Streamline analysis for 25 Hz

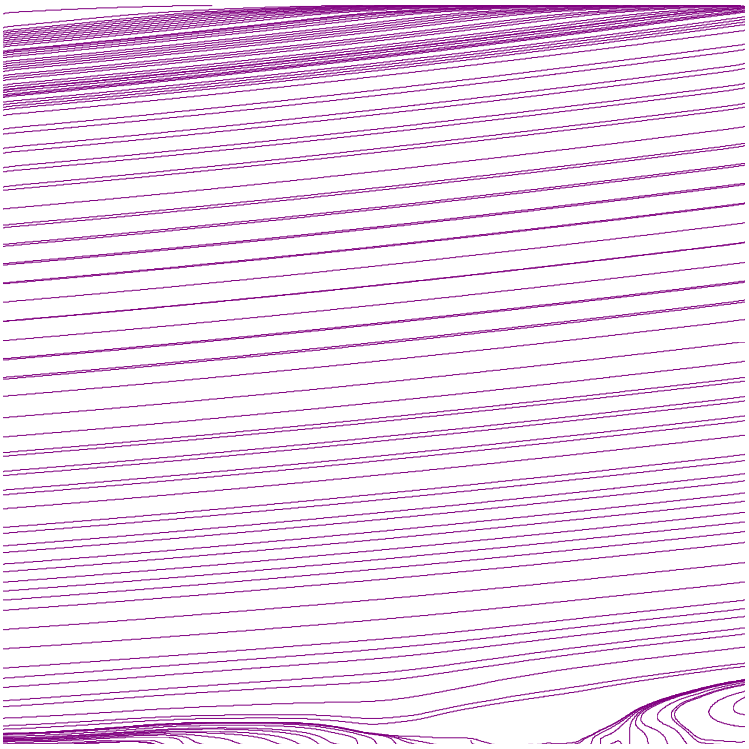

Figure 41. Streamline analysis for 75 Hz

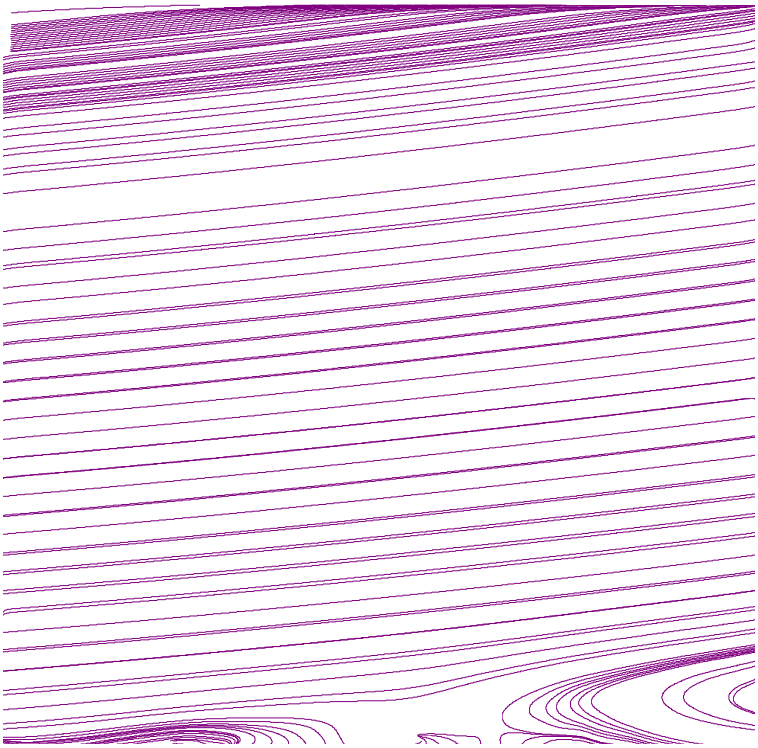

Figure 42. Streamline analysis for 100 Hz

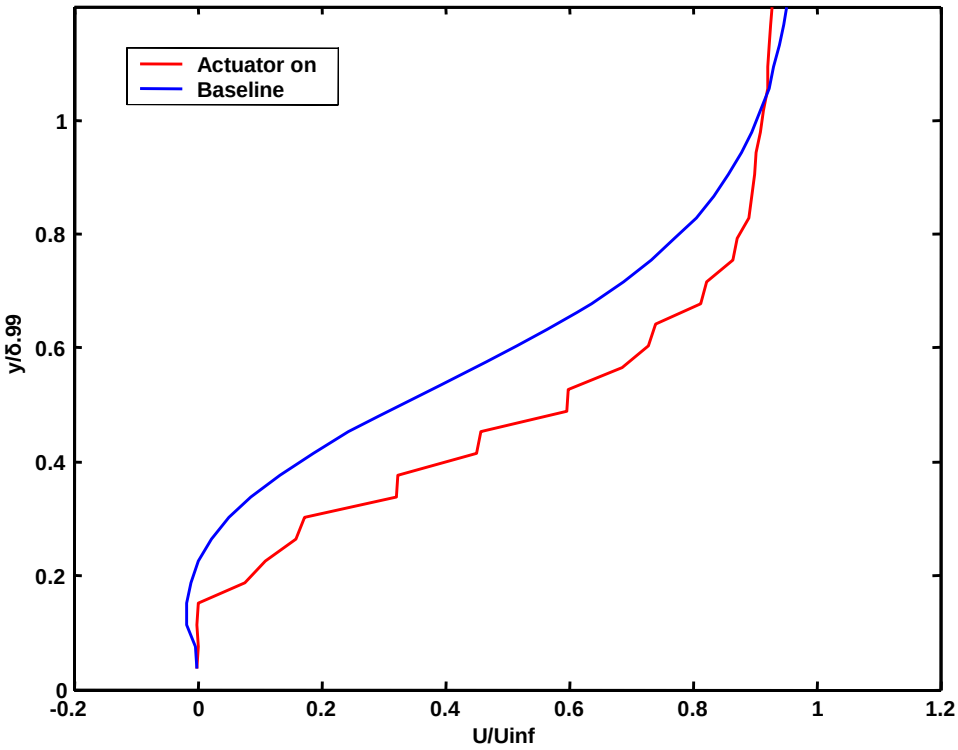

Figure 43. Boundary layer profile plot for 50 Hz

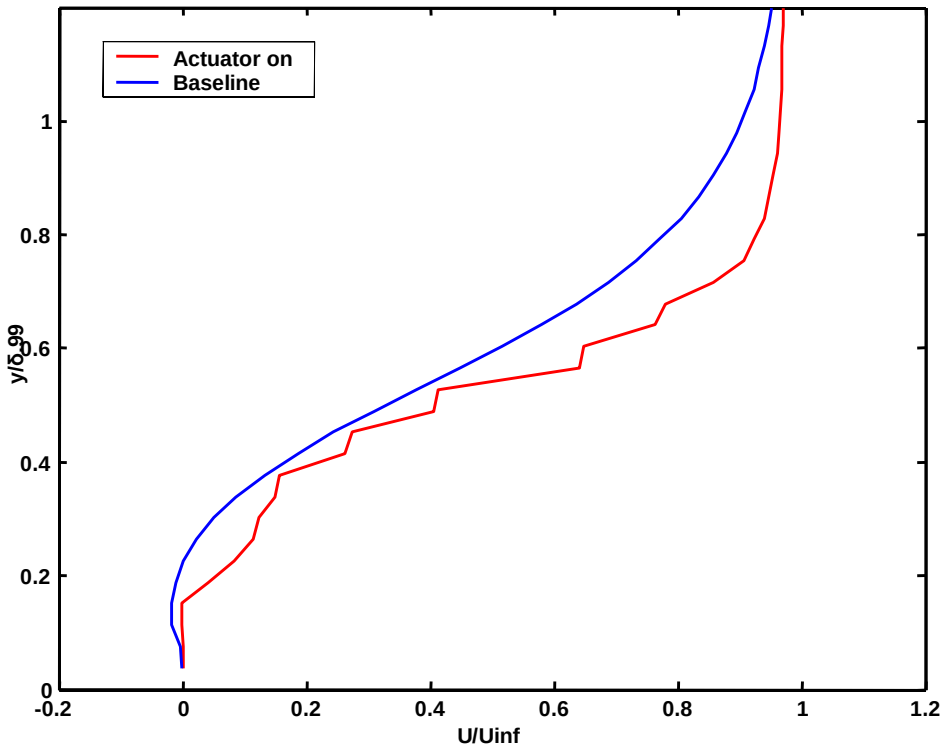

Figure 44. Boundary layer profile plot for 75 Hz

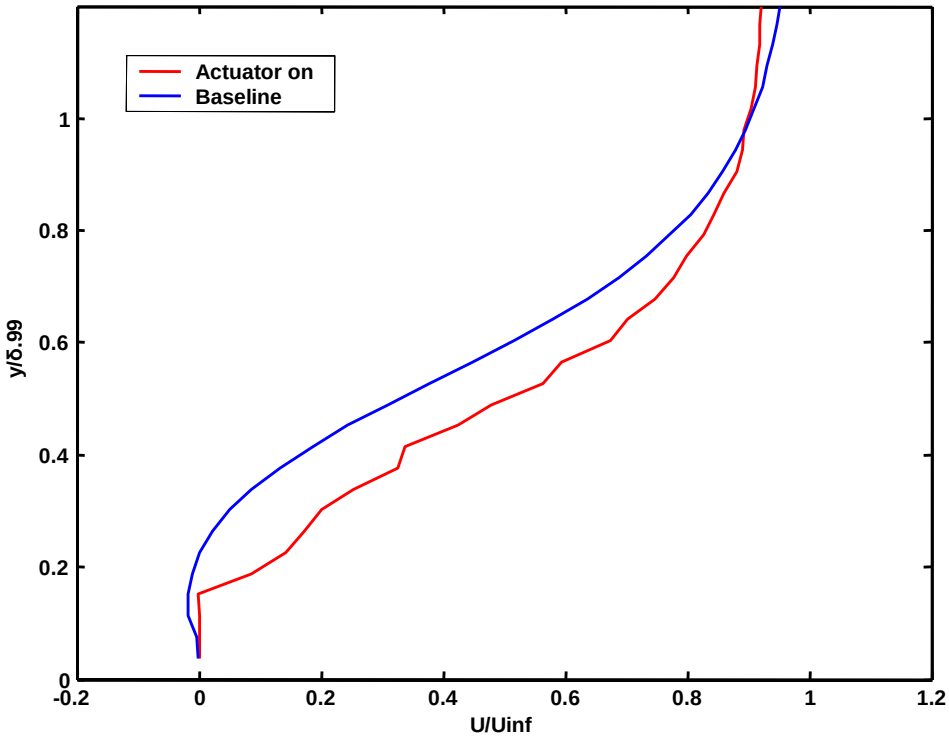

Figure 45. Boundary layer profile plot for 100 Hz

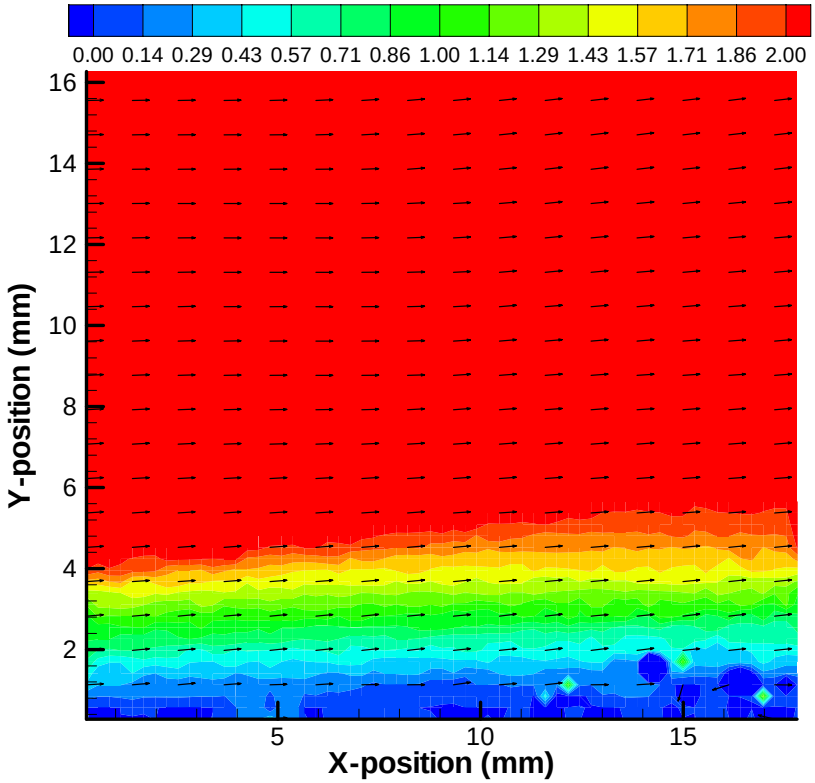

Figure 46. Velocity vector contours for 25 Hz

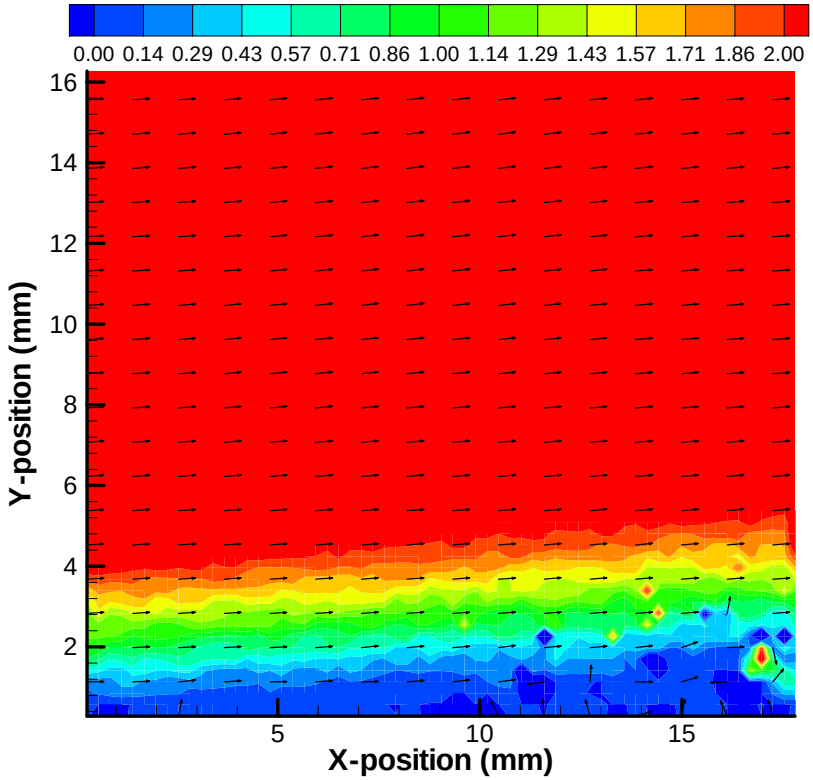

Figure 47. Velocity vector contours for 50 Hz

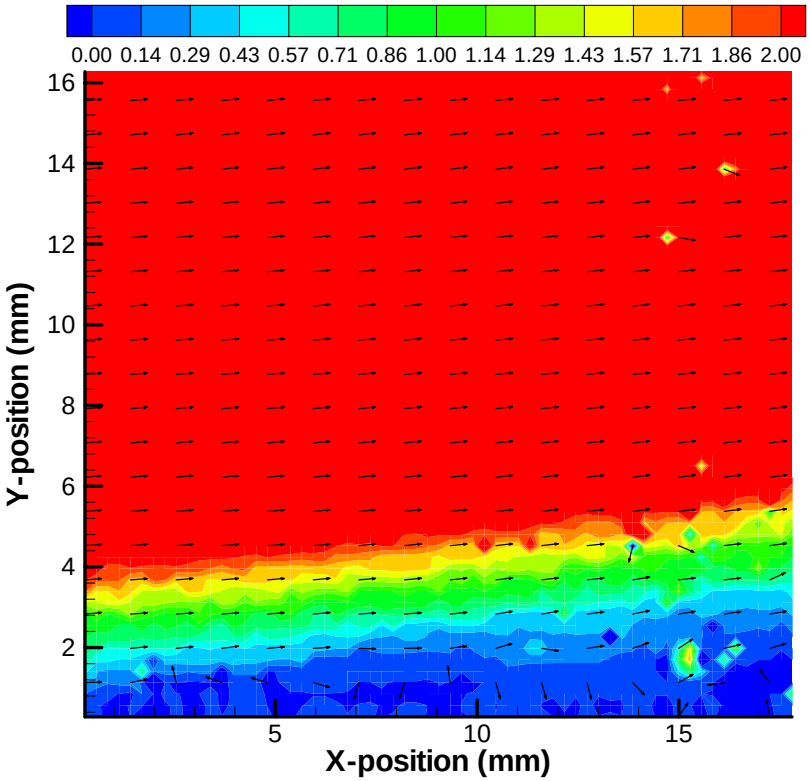

Figure 48. Velocity vector contours for 75 Hz

Appendix C: Average Velocity Contours

This appendix includes the average 70% velocity contours for the other frequencies. All of the velocity contours for the actuator on were an average of images that effectively moved the separation point behind the bottom electrode. In all cases, the plasma effectively decreases the size of the boundary layer compared to the baseline condition. Also included are representative contours at 50%, 60%, 80%, and 90% of the free stream velocity at 75 Hz.

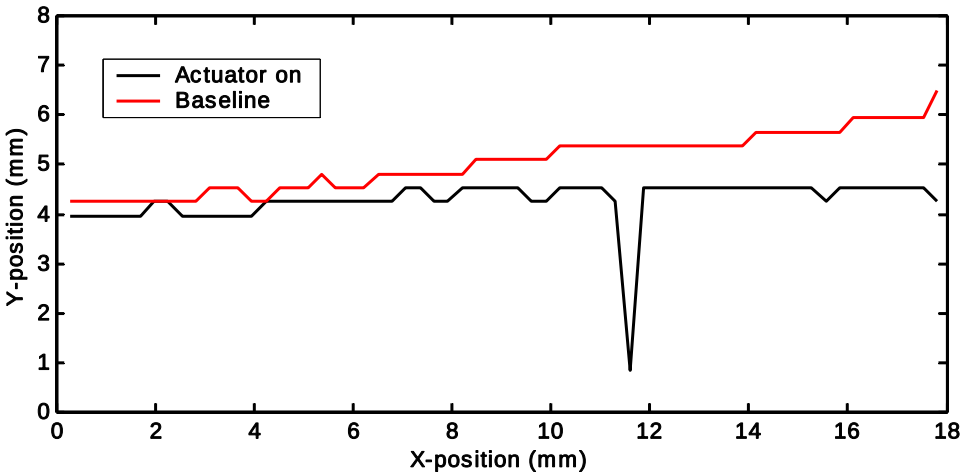

Figure 49. 70% velocity contour at 25 Hz

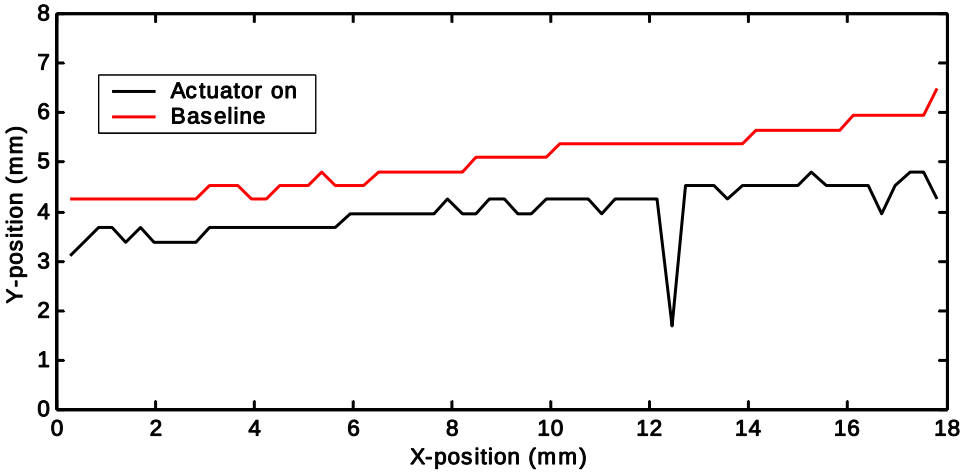

Figure 50. 70% velocity contour at 50 Hz

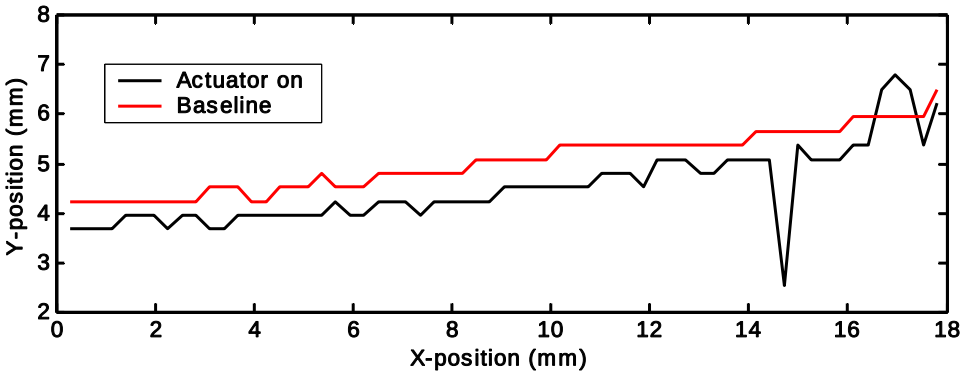

Figure 51. 70% velocity contour at 75 Hz

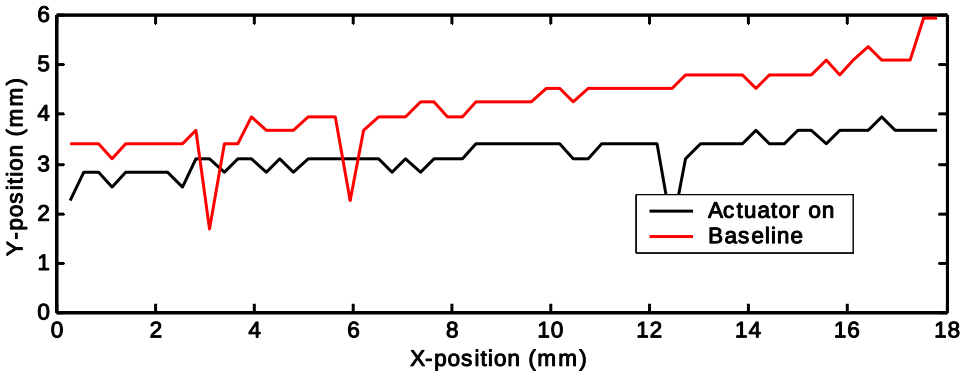

Figure 52. 50% velocity contour

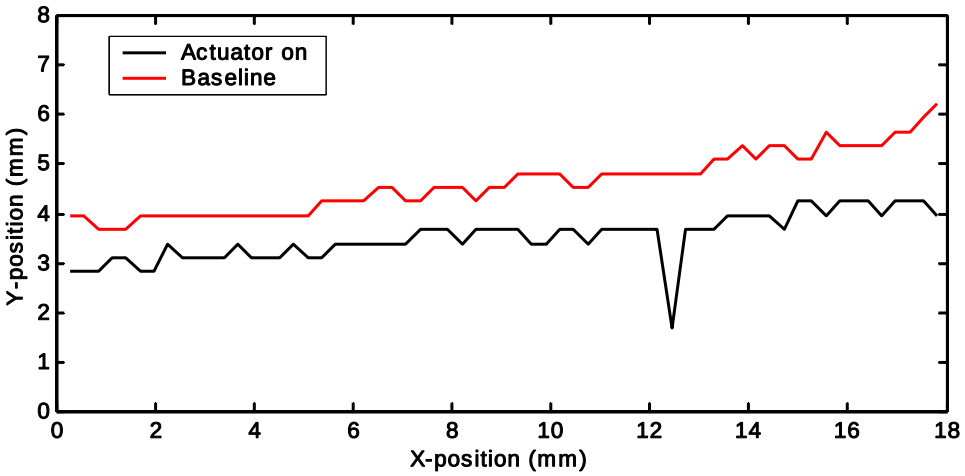

Figure 53. 60% velocity contour

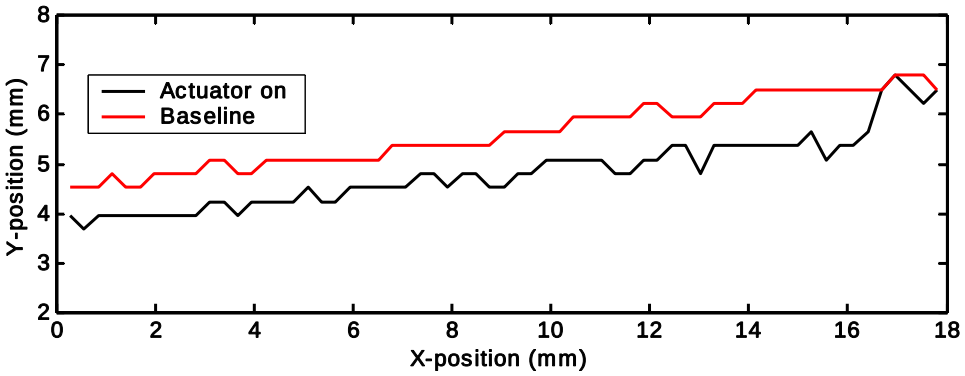

Figure 54. 80% velocity contour

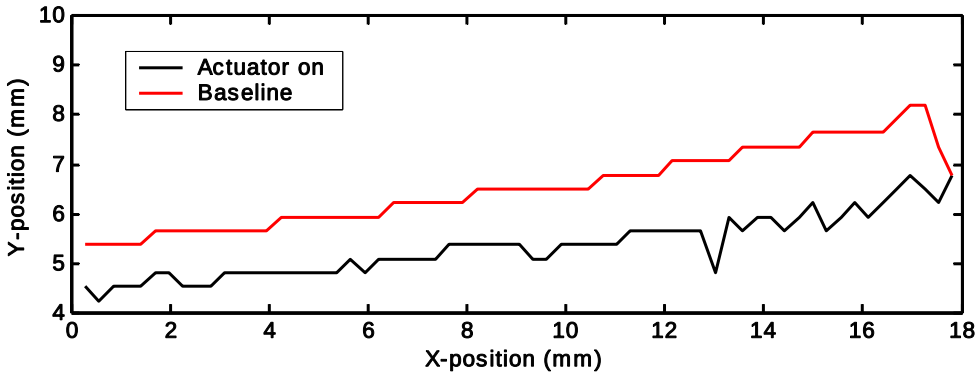

Figure 55. 90% velocity contour

Appendix D: Supplemental Power Spectrum Plots

This section is included to show the thoroughness in the objective of finding evidence of a characteristic frequency at the seventy percent free stream velocity contour. Similar graphs were analyzed at different contours but will not be presented here as results were practically identical. As discussed previously in the results section, only the magnitude of these graphs changed and the general shape remained constant. The graphs following are the average power spectrums found at three different columns provided in addition to the figures presented in the main results. Representative image sets for the baseline and the four different run conditions are included. These graphs support the conclusion that no extraneous frequency exists for the actuator on case compared to the baseline condition.

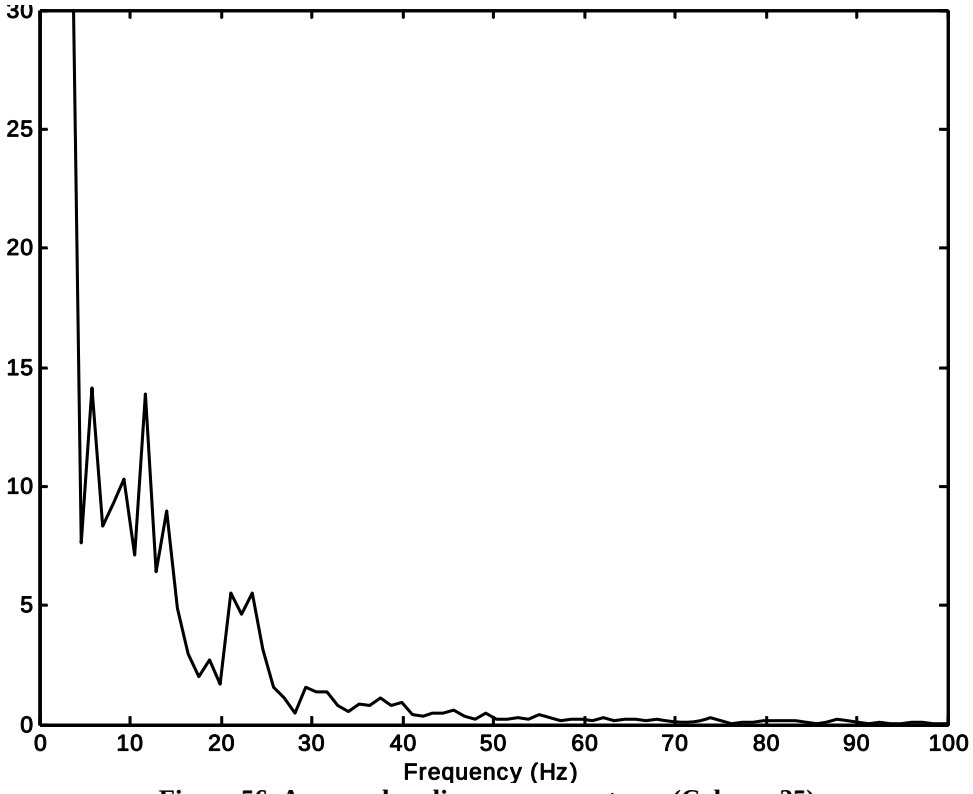

Figure 56. Average baseline power spectrum (Column 35)

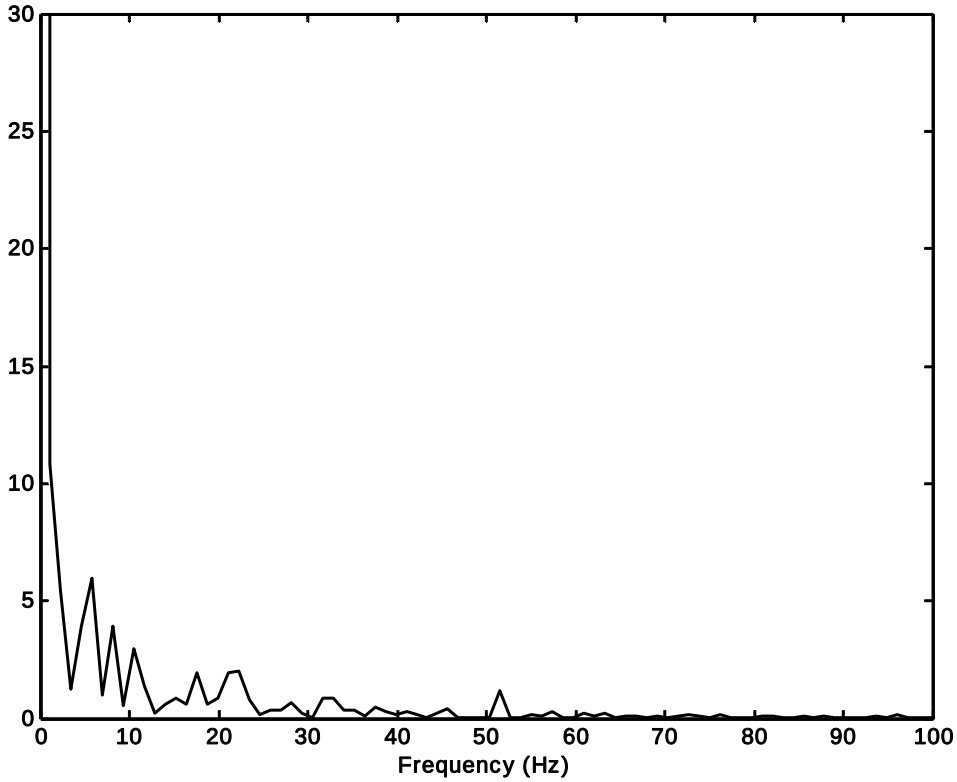

Figure 57. Average power spectrum at 25 Hz (Column 35)

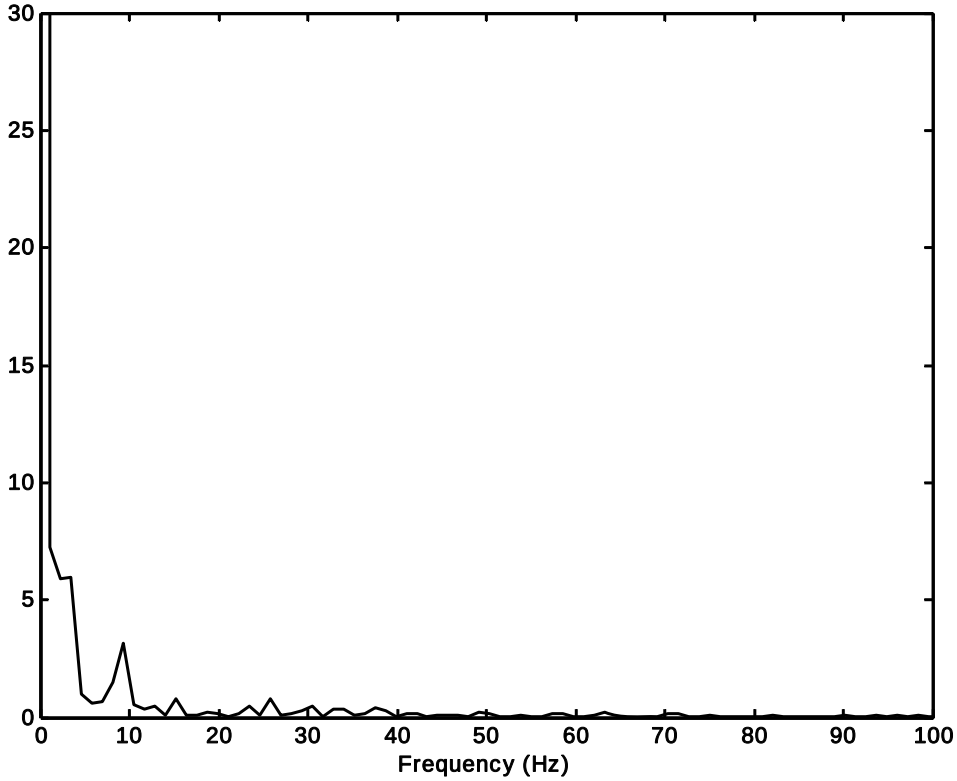

Figure 58. Average power spectrum at 50 Hz (Column 35)

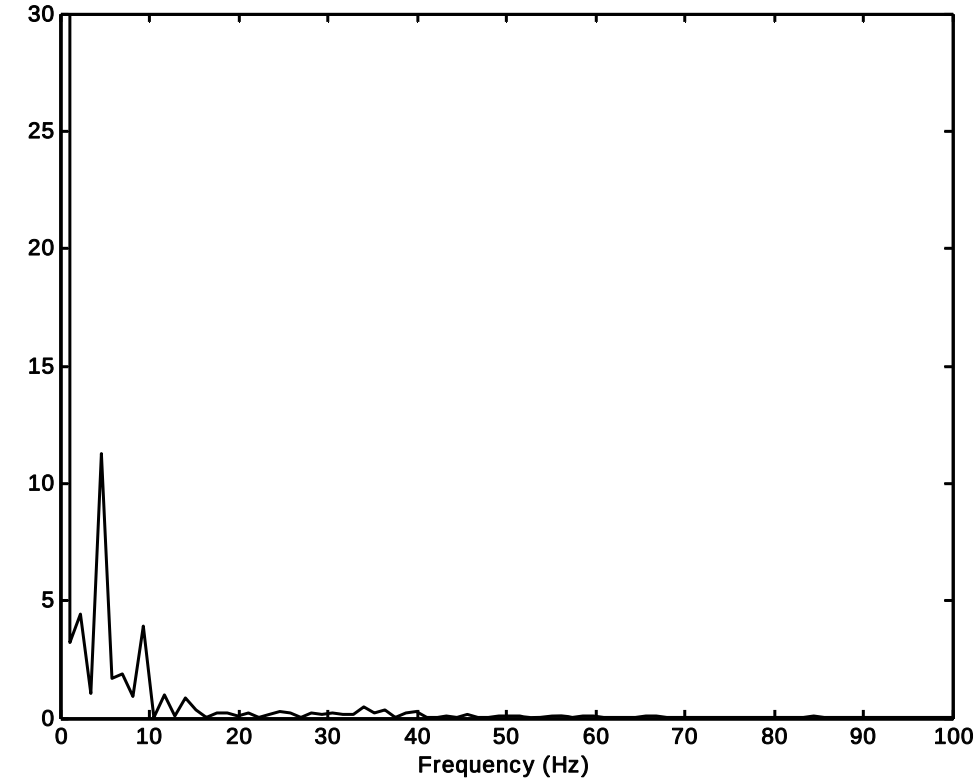

Figure 59. Average power spectrum at 75 Hz (Column 35)

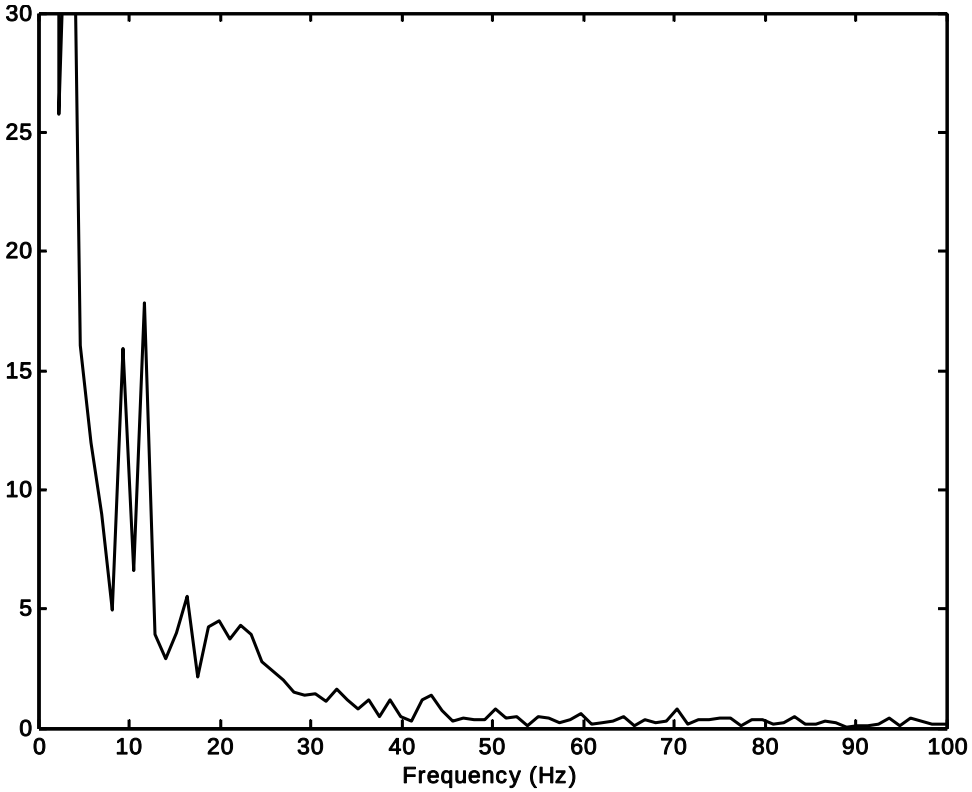

Figure 60. Average power spectrum at 100 Hz (Column 35)

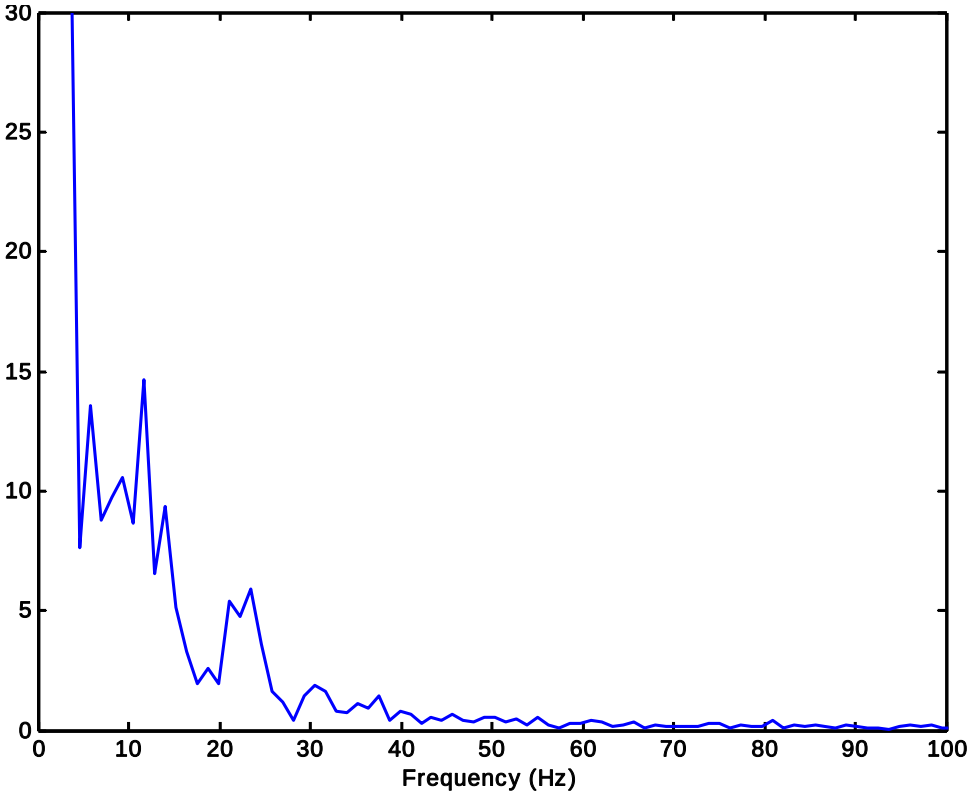

Figure 61. Average baseline power spectrum (Column 40)

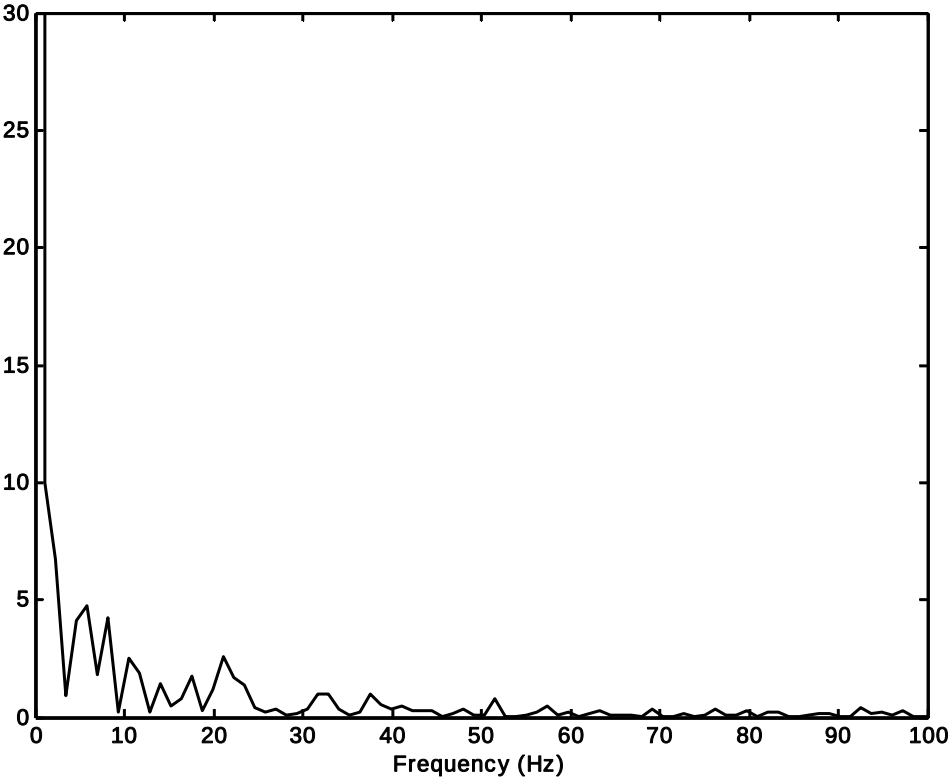

Figure 62. Average power spectrum at 25 Hz (Column 40)

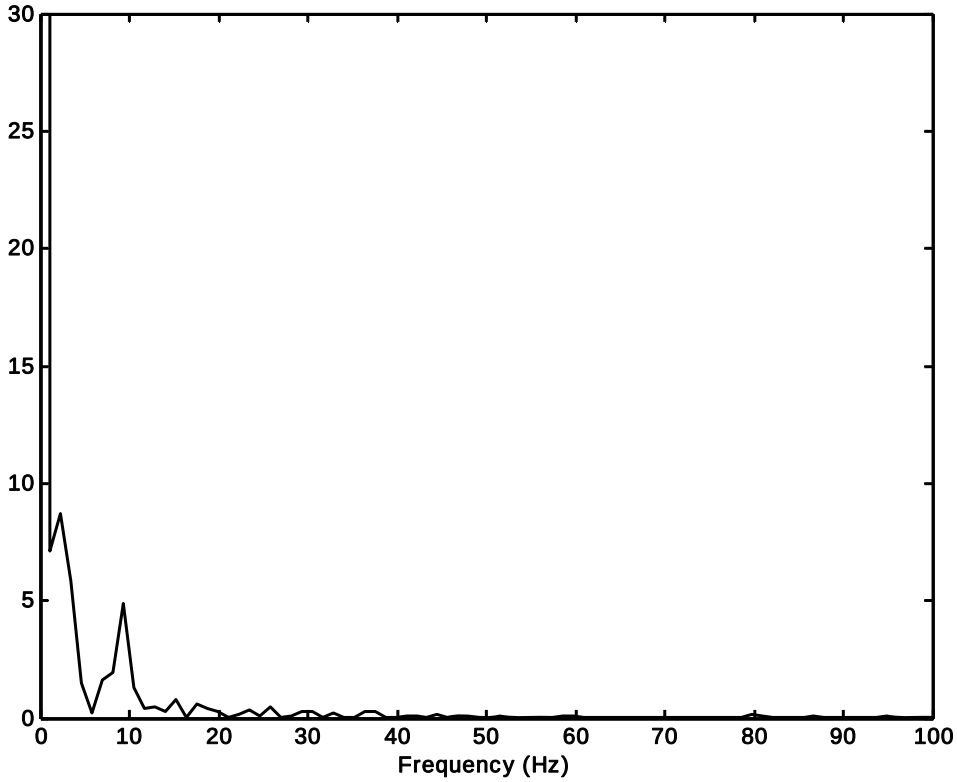

Figure 63. Average power spectrum at 50 Hz (Column 40)

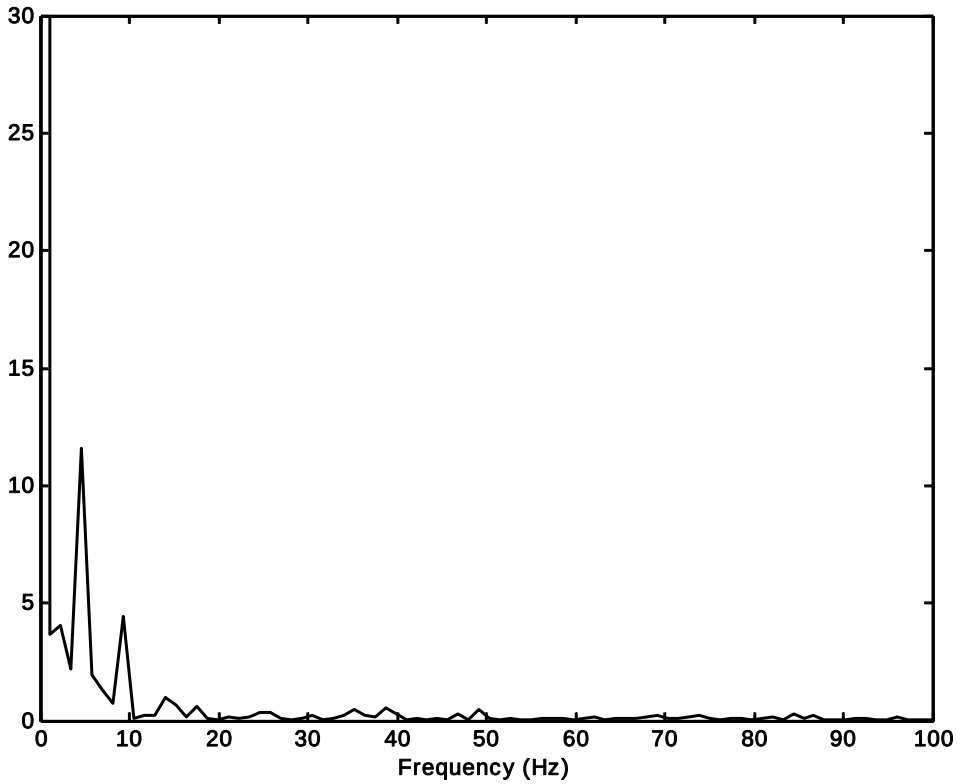

Figure 64. Average power spectrum at 75 Hz (Column 40)

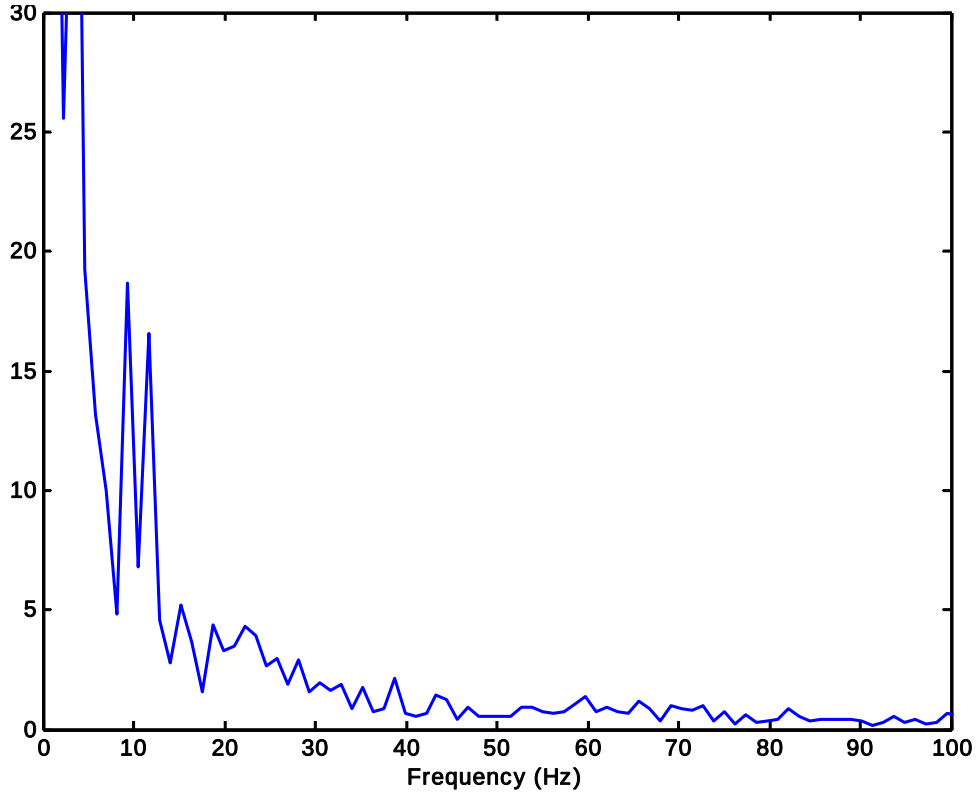

Figure 65. Average power spectrum at 100 Hz (Column 40)

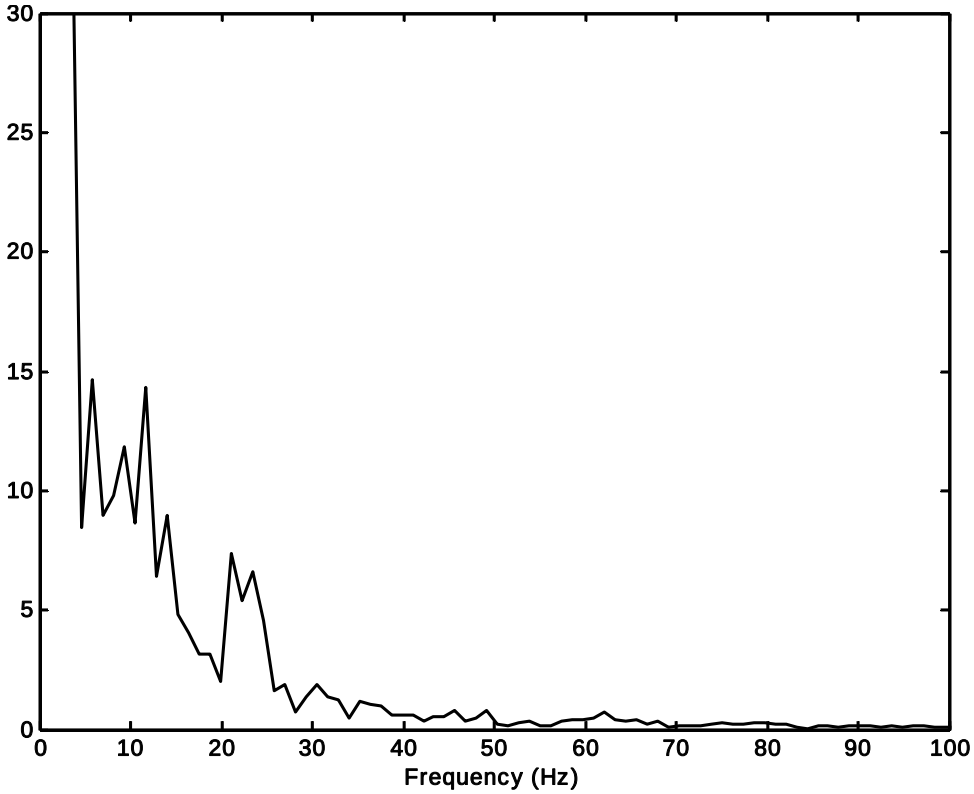

Figure 66. Average baseline power spectrum (Column 45)

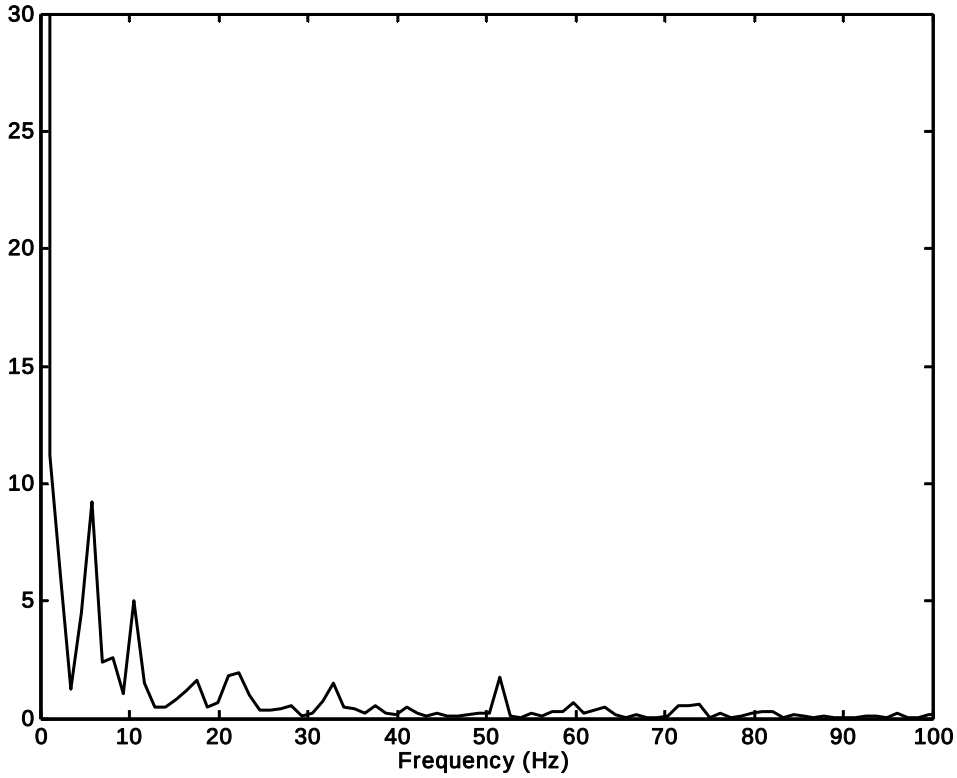

Figure 67. Average power spectrum at 25 Hz (Column 45)

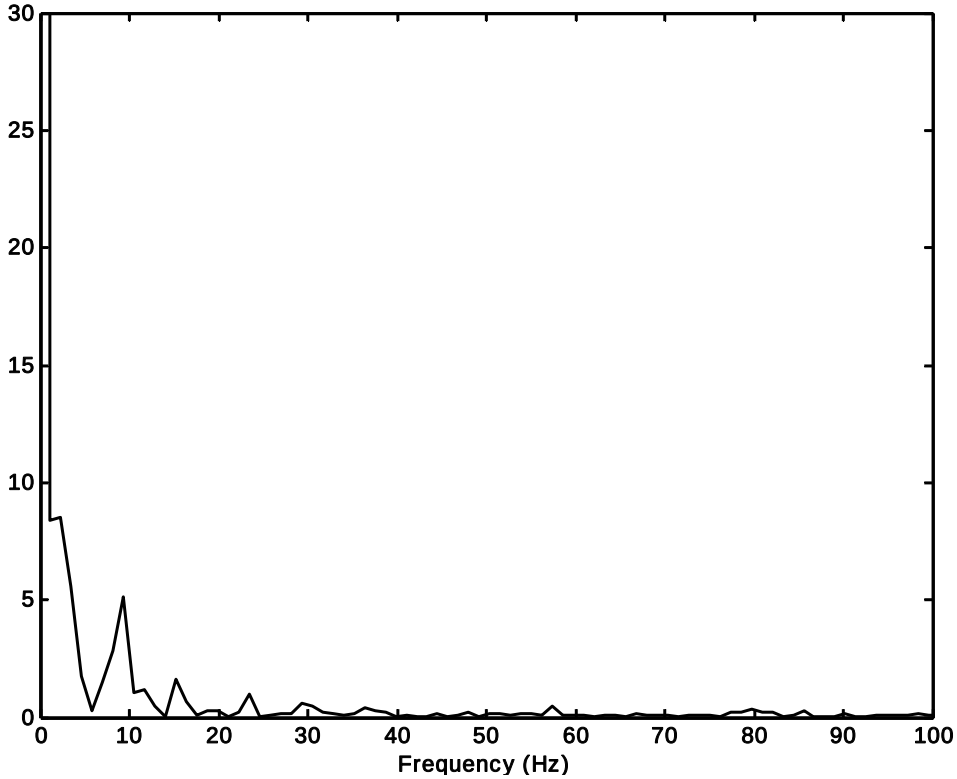

Figure 68. Average power spectrum at 50 Hz (Column 45)

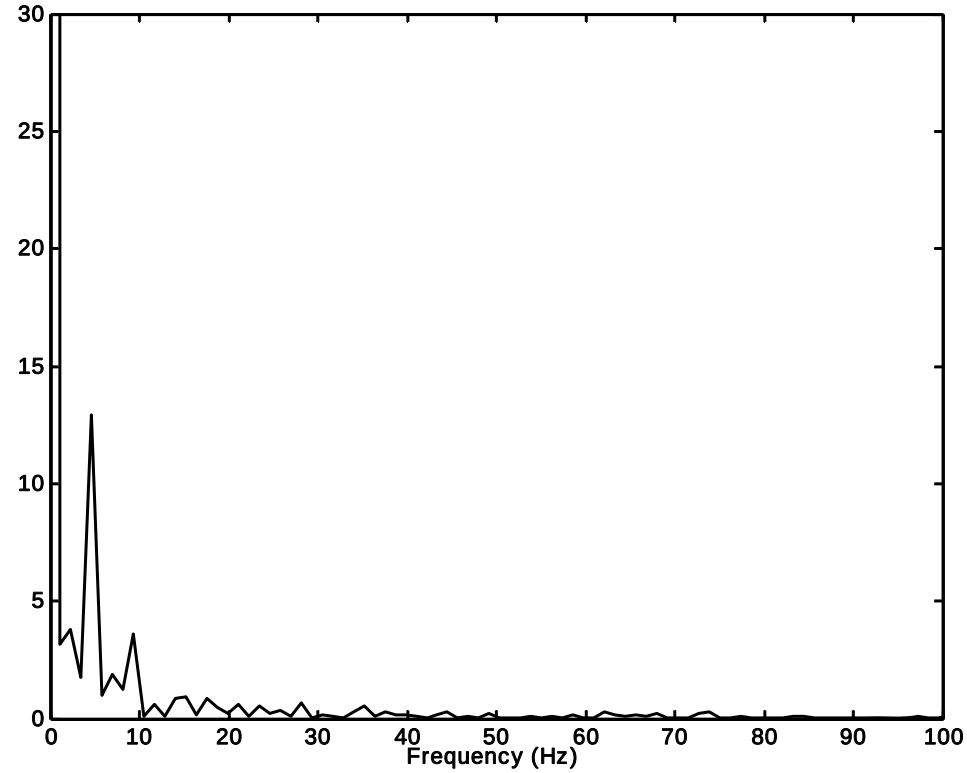

Figure 69. Average power spectrum at 75 Hz (Column 45)

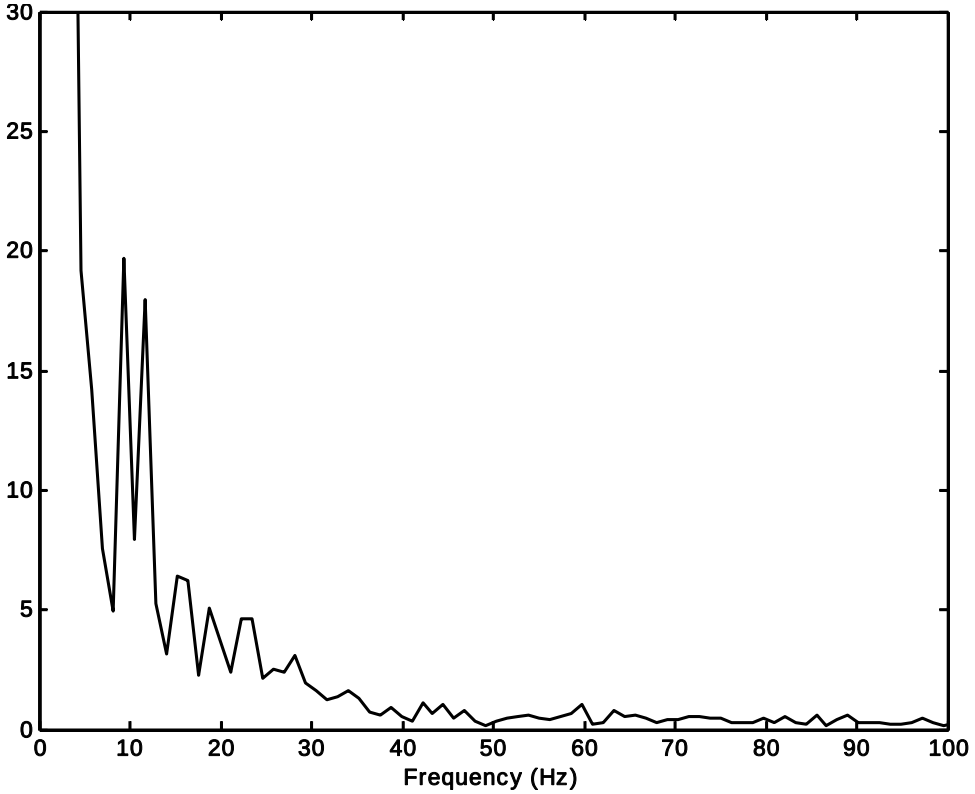

Figure 70. Average power spectrum at 100 Hz (Column 45)

References

1. Hultgren L., and Ashpis, D. “Demonstration of Separation Delay with Glow-Discharge Plasma Actuators,” American Institute of Aeronautics and Astronautics, AIAA Paper 2003-1025, (Reno, NV, Jan 2003).

2. Viets, H., Piatt, M., and Ball, M. “Forced Vortices near a Wall,” American Institute of Aeronautics and Astronautics, AIAA Paper 1981-256, (Saint Louis, MO, Jan 1981).

3. Rivir, R., Sondergaard, R., Bons, J., and Yurchenko, N. “Control of Separation in Turbine Boundary Layers,” American Institute of Aeronautics and Astronautics, AIAA Paper 2004-2201, (Portland, OR, July 2004).

4. Huang, J., Corke, T., Thomas, F. “Plasma Actuators for Separation Control of Low Pressure Turbine Blades,” American Institute of Aeronautics and Astronautics, AIAA Paper 2003-1027, (Reno, NV, Jan 2003).

5. Roth, J., Sherman, D., Wilkinson, S. “Boundary Layer Flow Control with a One Atmosphere Uniform Glow Discharge Surface Plasma,” American Institute of Aeronautics and Astronautics, AIAA Paper 98-0328, (Reno, NV, Jan 1998).

6. VanDyken, R., McLaughlin, T., and Enloe, C. “Parametric Investigations of a Single Dielectric Barrier Plasma Actuator,” American Institute of Aeronautics and Astronautics, AIAA Paper 2004-0846, (Reno, NV, Jan 2004).

7. Volino, R. and Hultgren, L. “Measurements in Separated and Transitional Boundary Layers under Low-Pressure Turbine Airfoil Conditions,” Journal of Turbomachinery, 123:189-197, 2001.

8. Corke, T. and Post, M. “Overview of Plasma Flow Control: Concepts, Optimization, and Applications,” American Institute of Aeronautics and Astronautics, AIAA Paper 2005-0563, (Reno, NV, Jan 2004).

9. Corke, T. and Cavalieri, D. “Controlled Experiments on Instabilities and Transition to Turbulence in Supersonic Boundary Layers,” American Institute of Aeronautics and Astronautics, AIAA Paper 97-1817, (Snowmass Village, CO July 1997).

10. Enloe, C., McLaughlin T., VanDyken, R., and Fischer, J. “Plasma Structure in the Aerodynamic Plasma Actuator,” American Institute of Aeronautics and Astronautics, AIAA Paper 2004-0844, (Reno, NV, Jan 2004).

11. Rivir, R., White, A., Carter, C., and Ganguly, B. “AC and Pulsed Plasma Flow Control,” American Institute of Aeronautics and Astronautics, AIAA Paper 2004-0847, (Reno, NV, Jan 2004).

12. Bertin, J. *Aerodynamics for Engineers, Fourth Edition.* Upper Saddle River, NJ: Prentice Hall, Inc., 2002.

13. Balcer, B., Franke, M., and Rivir, R. "Effects of Plasma Induced Velocity on Boundary Layer Flow," American Institute of Aeronautics and Astronautics, AIAA Paper 2006-875, (Reno, NV, Jan 2006).

14. Balcer, B., "Boundary Layer Flow Control Topics Using Plasma Induced Velocity," M.S. Thesis, AFIT/GAE/05-M03, Air Force Institute of Technology (AU), Wright-Patterson AFB OH, 2005.

15. "Low Differential Pressure Transducers," *GE Sensing manual,* April 2006. http://www.gesensing.com/products/lpm5000.htm.

16. "High Voltage DC Power Supply," *Glassman PK series manual,* April 2006. http://www.glassmanhv.com/PDFs/PK_Series.pdf.

17. "Fast High Voltage Transistor Switches," *Behlke HTS 151 manual,* April 2006. http://www.behlke.de/separations/separation_c8.htm.

18. "High Voltage Probe Specifications Sheet," *North Star Research Corporation,* April 2006. http://www.northstar-research.com/pvm.html.

19. "Current Monitor Specifications Sheet," *Pearson Electronics,* April 2006. http://www.pearsonelectronics.com/current-monitor-products/standard-current-monitor.htm.

20. Boxx, I., Newcamp, J., Woods, N., Rivir, R., and Franke, M. "A PIV Study of a Plasma Discharge Flow-Control Actuator on a Flat Plate in an Aggressive Pressure Induced Separation," Proceedings of ASME Turbo Expo 2006, Paper GT2006-91044, (Barcelona, Spain, May 2006).

21. "Pegasus-PIV Laser," *New-Wave manual,* April 2006. http://www.new-wave.com/DownLoad%20Files/PV-PEG-DSa4-0311.pdf.

22. "High Speed APX Camera," *Photron manual,* April 2006. http://www.photron.com/pdf/ultima_APX.pdf.

23. "Quantum Composer Specifications Sheet," *Quantum Composer Incorporated,* April 2006. http://www.quantumcomposers.com/cgi-bin/quantumcomposers/knowledge_base/display.html.

REPORT DOCUMENTATION PAGE

Form Approved
OMB No. 074-0188

1. REPORT DATE *(DD-MM-YYYY)*	**2. REPORT TYPE**	**3. DATES COVERED** *(From – To)*
13-06-2006	**Master's Thesis**	Sep 2005 – June 2006

4. TITLE AND SUBTITLE

An Experimental Study of a Pulsed DC Discharge Plasma Flow Control Actuator

5a. CONTRACT NUMBER

5b. GRANT NUMBER

5c. PROGRAM ELEMENT NUMBER

6. AUTHOR(S)

Wall, Jennifer D., Ensign, USN

5d. PROJECT NUMBER

5e. TASK NUMBER

5f. WORK UNIT NUMBER

7. PERFORMING ORGANIZATION NAMES(S) AND ADDRESS(S)

Air Force Institute of Technology
Graduate School of Engineering and Management (AFIT/EN)
2950 Hobson Way
WPAFB OH 45433-7765

8. PERFORMING ORGANIZATION REPORT NUMBER

AFIT/GAE/ENY/06-J16

9. SPONSORING/MONITORING AGENCY NAME(S) AND ADDRESS(ES)

Air Force Research Labs, AFRL/PRTT
Attn: Dr. Richard Rivir
1950 West 5th Street
WPAFB OH 45433-7251 DSN: 785-4539

10. SPONSOR/MONITOR'S ACRONYM(S)

11. SPONSOR/MONITOR'S REPORT NUMBER(S)

12. DISTRIBUTION/AVAILABILITY STATEMENT

APPROVED FOR PUBLIC RELEASE; DISTRIBUTION UNLIMITED.

13. SUPPLEMENTARY NOTES

14. ABSTRACT

An experiment on the effects of a pulsed DC plasma actuator on a separated flow in a low speed wind tunnel was conducted. The actuator consisted of two asymmetric copper electrodes oriented normal to the flow separated by a dielectric barrier and mounted on a flat plate in the center of the tunnel. A contoured insert was constructed and used to create an adverse pressure gradient in the test section comparable to a Pak-B low pressure turbine blade distribution. Suction was applied from the upper wall to induce separation along the flat plate over the electrodes. The DC power supply was kept constant at 8.5 kV and power was regulated through a high voltage fast transistor switch. The pulse width of the switch remained at 250 ns with the frequency ranging from 25 to 100 Hz. All studies were conducted at a Reynolds number of 30,000 to simulate takeoff and other low speed conditions. It was found that the DC pulsed plasma actuator could reattach the flow but not consistently at these conditions. Furthermore no evidence was found to indicate that coherent vortical structures are responsible for reenergizing the boundary layer and controlling separation

15. SUBJECT TERMS

Plasma discharge, turbine blades, pressure distributions, coherence, particle image velocimetry

16. SECURITY CLASSIFICATION OF:			**17. LIMITATION OF ABSTRACT**	**18. NUMBER OF PAGES**	**19a. NAME OF RESPONSIBLE PERSON**
REPORT	**ABSTRACT**	**c. THIS PAGE**			Dr. Milton Franke, AFIT/ENY
U	**U**	**U**	**UU**	95	**19b. TELEPHONE NUMBER** *(Include area code)* (937) 255-6565, ext 4720; e-mail: m.franke@afit.edu

Standard Form 298 (Rev: 8-98)
Prescribed by ANSI Std. Z39-18